Mechanical structures and thermal management scheme for HiClBaS's stratospheric balloon mission

Mémoire

Deven Patel

Maîtrise en physique - avec mémoire
Maître ès sciences (M. Sc.)

Québec, Canada

Résumé

Le projet HiCIBaS (High-Contrast Imaging Balloon System) est une mission de télescope à ballon dirigé dans le but de l'imagerie exoplanète en utilisant des techniques à contraste élevé. Pour la première mission en 2018, les principaux objectifs étaient de développer les systèmes nécessaires et de valider leurs performances, d'acquérir des données de vol et de prouver la capacité de survie de tous les systèmes et composants majeurs dans des conditions proches de l'espace.

Ce projet de maîtrise porte sur deux aspects de la charge utile: la conception de la monture de télescope alt-az dynamique pour le système de pointage et le développement des sangles thermiques personnalisées pour le système optique. La monture du télescope est la structure qui supporte le télescope et permet aux moteurs du système de pointage de le diriger vers la position souhaitée. Les sangles thermiques personnalisées sont une solution développée pour dissiper la chaleur générée par les principaux composants du système optique (caméras, contrôleurs, etc.). Les deux solutions ont été testées lors d'un vol de nuit en août 2018 dans le cadre de la campagne STRATOS de l'agence spatiale canadienne à Timmins, en Ontario. Ce mémoire définira les exigences des deux systèmes, présentera le développement des conceptions, détaillera les analyses et les tests effectués, démontrera la conformité aux exigences, commentera sur les performances de la mission et donner des conseils des moyens d'améliorer les deux conceptions pour les futures itérations du projet.

Abstract

The HiCIBaS (High-Contrast Imaging Balloon System) project is a balloon-borne telescope mission with the big-picture goal of exoplanet-imaging using high-contrast techniques. For the scope of the pilot mission in 2018, the main goals were to develop the necessary systems and validate their performance, acquire flight data, and prove the survivability of all systems and major components in near-space conditions.

This Master's project deals with two aspects of the overall payload: the design of the dynamic alt-az telescope mount for the pointing system and the development of the custom thermal straps for the optics system. The telescope mount is the structure that supports the telescope and allows the pointing system's motors to direct it to the desired position. The custom thermal straps are a solution that was developed to dissipate the heat generated by the optics system's main components (cameras, controllers, etc.). Both solutions were tested during an overnight flight in August of 2018 under the Canadian Space Agency's STRATOS campaign in Timmins, Ontario. This *mémoire* will define the requirements for both systems, present the development of the designs, detail the analyses and tests performed, demonstrate conformance to the requirements, comment on mission performances, and provide insight on ways to improve both designs for future iterations.

Table of Contents

List of Figures

List of Tables

List of Abbreviations and Acronyms

CAD	Computer-aided design
CCD	Charge-coupled device
CNES	Centre National d'Études Spatiale
CSA	Canadian Space Agency
DM	Deformable mirror
EMCCD	Electron-multiplying charge-coupled device
HiCIBaS	High-Contrast Imaging Balloon System
LOWFS	Low-order wavefront sensor
OAP	Off-axis parabolic
SOW	Scope of work
V&V	Verification & Validation

Introduction

Scientific Context

In the realm of astronomy, high-contrast imaging is a technique used to detect faint objects, such as exoplanets, that are in proximity to bright sources, such as stars. Typically, this is accomplished using a coronagraph, an instrument that physically blocks a star from the view of a detector, suppressing its starlight (Kaufman, 2017). With less light present in the field of view, the detector will be less saturated, and the faint objects can more effectively be detected. This is demonstrated in Figure 1 with the HR 8799 star suppressed in the center and the 4 exoplanets exposed (denoted as b, c, d, and e).

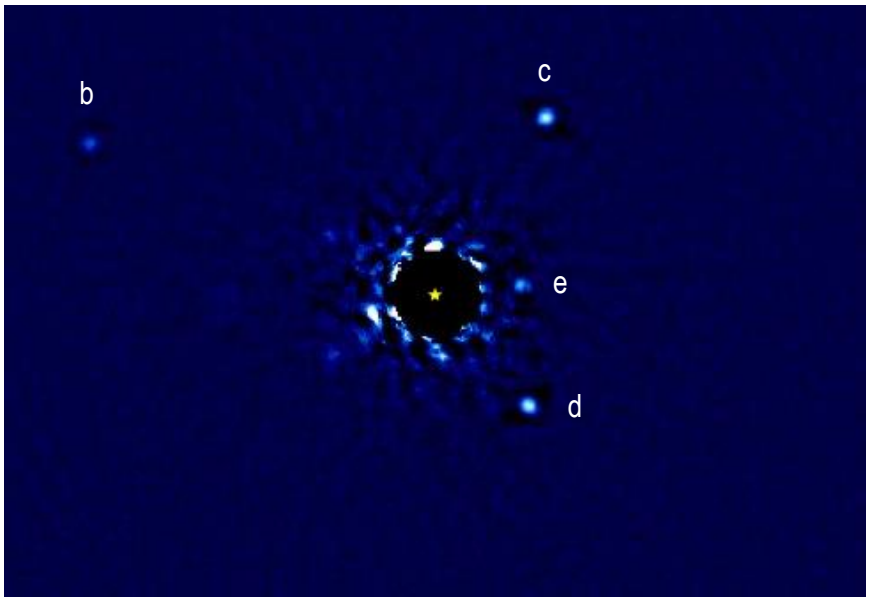

Figure 1: Example of high-contrast techniques used for exoplanet-imaging (Kaufman, 2017)

Even with this technique, ground-based telescopes encounter difficulties with exoplanet imaging due to "astronomical seeing," a phenomenon caused by atmospheric turbulence (MacRobert, 2006). Earth's atmosphere is composed of several different layers that each have drastically different air properties and environmental conditions. This results in differing optical refractive indices throughout the atmosphere and that effects the way light is refracted, causing the image taken on-ground to be blurry. Since atmospheric turbulence is dynamic, the light's wavefront is constantly being aberrated, as demonstrated by Figure 2, causing it to appear as if it is "twinkling" because of the variation of light intensity from one moment to the next; this phenomenon is also known as scintillation. Atmospheric turbulence in the troposphere (closest to the ground) is the hardest to predict and, therefore, plays the biggest role in atmospheric seeing.

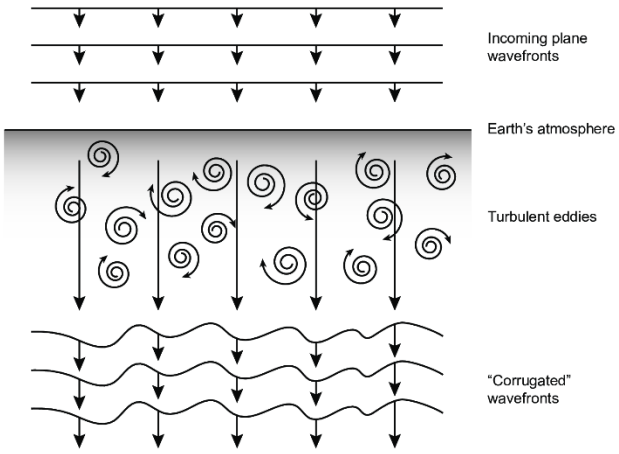

Figure 2: The effect of atmospheric turbulence on incoming starlight wavefronts (Buscher, 2015)

Astronomical seeing can be overcome, though, using advanced optical instrumentation and by using techniques to countermeasure the aberrations caused, as seen with the advent of adaptive optics in astronomy. However, another strategy can be used to circumvent the problem altogether: performing the imaging *outside* of Earth's atmosphere.

Purpose of HiCIBaS

The big-picture goal of Université Laval's High-Contrast Imaging Balloon (HiCIBaS) project is to perform exoplanet imaging from the stratosphere, effectively eliminating the worst contributor to astronomical seeing (the troposphere) by being above 99.996% of the air in Earth's atmosphere. A successful mission would have multiple benefits, not limited to just the performance of high-contrast imaging and airborne telescopes. Space-based telescopes are extremely costly and, for those that don't venture into deep space, a cheap alternative can be high-altitude observations. Sub-orbital flights are also much more practical as they can be recovered, maintained or modified, and relaunched. With the introduction of newer technologies for space-based telescopes, high-altitude balloon flights offer a unique platform for near-space conditions for testing and system design validation purposes, even if the flight duration will be significantly shorter than an orbital mission.

However, to realize this long-term goal, there are many functional issues linked to high-altitude observations, that need to be addressed. One of the biggest issues is pointing stability. For ground-based telescopes, the use of a coronagraph is highly effective because the telescope itself is relatively stable and typically only moving in very small increments in altitude and azimuth directions. A high-altitude balloon, though, is constantly moving in 3D space in the stratosphere, as well as moving in altitude and azimuth directions to track a star. This causes the performance of the optical system to be dependent on the performance of the pointing system. Pointing errors can result in contrast degradation in two ways: jitter and stability error, and imperfect centering of the coronagraph on the target star. Jitter and stability error would cause wavefront errors generated by beam-walk and imperfect centering of the coronagraph would cause starlight leaking onto the detector; both contributing to contrast degradation (Université Laval, 2016).

Another major challenge is designing systems while lacking reliable data surrounding the high-altitude environment. Air properties and ambient temperatures vary significantly based on geographical location, altitude and day-to-day meteorology. As a result, atmospheric turbulence, and the aberrations caused by it, are impossible to define and to design for. A prior mission, a pilot mission, is required to characterize these conditions and their effects on: temporal variability, scintillation, coherence cell diameter, transmission, and stray or scatted light (Université Laval, 2016).

In the case of both challenges, a Low-Order Wavefront Sensor (LOWFS) is something that can be used. Very simply, a LOWFS is an optical system that measures wavefront errors caused by low-order optical aberrations (defocus, etc.) and aids in their correction by sending data to another optical component, or system, that can correct for them. For HiCIBaS, the LOWFS can serve as fine-pointing correction to mitigate stability problems and keep the coronagraph centered on the target star.

Objectives of the HiCIBaS Mission

In order to achieve the short-term goals, necessary for the long-term vision, outlined in section 1.2, HiCIBaS has 5 specific objectives for the pilot mission (Université Laval, 2016):

1. Develop and test a promising new type of Low-Order Wavefront Sensor (LOWFS).
2. Develop and test a generic precision pointing telescope system that can be used in future missions requiring sub-milli-arcsecond level pointing (e.g. high-contrast imaging missions).
3. Measure and gather data on the wavefront instabilities and errors encountered at 40 km of altitude in the visible region of the spectrum (scientific interest).
4. Test optical components (DM, coronagraph) for future high-contrast imaging missions.
5. Fly in space-like conditions the LOWFS including a Nuvu EMCCD camera.

Objectives of the Project

This project involves the mechanical aspects of the payload. More specifically, the mandate for the mechanical specialist of this project was to:

1. Design a dynamic alt-az mount that is capable of supporting a 14” telescope.
2. Design a thermal system capable of dissipating the heat generated by the detectors, controllers and voltage regulator (of the Nüvü Cameras’ components).

The first mandate pertains directly to the 2nd objective of the HiCIBaS mission because it involves the development of the mechanical structure that is required for the pointing system. The second mandate supports the 4th and 5th objectives of the mission by ensuring the proper operation and performance of the associated systems.

Both solutions will be discussed in-depth in Chapters 1 and 2, respectively, of this memoir. In them, the low-level requirements will be defined, the final designs and motivating factors will be reviewed, the analyses

and simulations performed will be detailed and discussed, the mission performance will be evaluated, and, finally, ways to improve both designs will be advised.

Chapter 1: Dynamic Telescope Mount Structure

1.1 Scope of Work (SOW)

The dynamic telescope mount structure is one of the two main structures of the HiCIBaS project (the optics bench being the second). The mount structure serves two main purposes: to accommodate the front-end optics (telescope, Nasmyth mirror, etc.) and to provide a dynamic platform for the pointing system to guide the telescope. In other words, this structure is directly contributing towards the success of Objective 2.

More specifically, the telescope mount structure must:

1. Demonstrate structural integrity, as defined by the Canadian Space Agency (CSA) and Centre National d'Études Spatiale (CNES).
2. Respect the maximum weight limit, as defined by CNES.
3. Provide the necessary degrees of freedom in altitude and azimuth direction, as required by the pointing system.
4. Respect the dimensional and positional restrictions of the front-end optics, as required by the optics system.
5. Accommodate the components of, both, the pointing system and the optics system, as required by the respective specialists.

This chapter will detail the work done for the telescope mount structure and aim to demonstrate conformance to the scope of work defined above. Specifically, the requirements will be defined, followed by a discussion and description of the final design, an evaluation of the design with the approaches taken and the validation criteria, the mission performance of the structure, and, finally, recommendations for further improvement.

1.2 System Requirements

Table 1: Mount structure requirements

Requirement #	Requirement	Origin
1	The telescope and Nasmyth mirror central axes must intersect on the center of the tertiary mirror to a precision of 0.5 mm	Optics System
2	The Nasmyth mirror and OAP mirror central axes must intersect on the center of the tertiary mirror to a precision of 0.5 mm	Optics System
3	The rotational axis of the RM5 motor must be coaxial to the Nasmyth mirror's cylindrical mount to a precision of 0.5 mm	Optics System
4	The threaded flange (to mount optics) at the back of the telescope must be 121.141 mm from the tertiary mirror (center-to-center distance)	Optics System
5	The structure must never intersect with the optical axis at any point of the optics system	Optics System
6	The telescope must have ±20° of freedom in the azimuth direction with at least 20 mm of clearance at the extremities	Pointing System
7	The telescope must have +60° of freedom in the altitude direction with at least 20 mm of clearance at the extremity	Pointing System
8	The telescope must have at least -20° of freedom in the altitude direction and zero clearance from the descent support at the extremity	Pointing System
9	The maximum weight placed on the gondola's floor must be less than or equal to 100 kg	CNES
10	The operational load limits of the RM-3, RM-5, and RM-8 motors (as defined on their respective datasheets) must be met with a safety factor of 1.2 or more	Pointing System
11	The maximum normal load expected (P) on every insert of the gondola's floor must be less than or equal to 1960 N $(P_{crit})^2$	CNES
12	The maximum transverse load expected (Q) on every insert of the gondola's floor must be less than or equal to 4080 N $(Q_{crit})^2$	CNES
13	The following equation must be satisfied for every insert of the gondola's floor: $(P/P_{crit})^2 + (Q/Q_{crit})^2 \leq 1^2$	CNES
14	The design yield load (DYL) must be less than or equal to the material's tensile yield strength (YL): DYL ≤ YL[3]	CSA
15	The design ultimate load (DUL) must be less than or equal to the material's tensile yield strength (YL): DUL ≤ YL[3]	CSA
16	The load limit (LL) multiplied by 1.5 must be less than or equal to the material's tensile yield strength (YL): LL × 1.5 ≤ YL[3]	CSA

[1] As defined in the material datasheets for each of the respective motors (Appendix 1)
[2] As defined in the CARMEN_Insert_loads document (Appendix 2) provided by CNES and CSA.
[3] As defined in the CSA-STRATOS-RPT-0004-A-EN document (Appendix 3) provided by CSA.

Just as important as defining the requirements themselves is their origin. Therefore, here is a brief breakdown of the motivation behind the requirements:

- **Requirements 1-5:** To provide the necessary positioning and tolerancing for the optical design concept and to ensure optimal performance of the optical system.
- **Requirements 6-8:** To provide the necessary degrees of freedom for the pointing system to track and follow the movement of the targeted star over the duration of the mission.
- **Requirement 9:** To demonstrate adherence to the maximum allowable weight supported by the CARMEN gondola's floor.
- **Requirement 10:** To demonstrate the capability of the motors to perform their respective tasks for their respective applications.
- **Requirement 11-13:** To demonstrate adherence to the load limits of the M6 inserts on the CARMEN gondola's floors imposed by CNES.
- **Requirement 14-16:** To demonstrate structural integrity of the mount structure to the CSA for safety reasons.

1.3 System Design

1.3.1 Design Breakdown and Driving Factors

This section will highlight the key factors considered during the design phase of the mount structure and how they played in role in design and component choices made during its development.

In terms of the *overall,* large-scale design, the mount structure was made to respect the dimensional constraints of the CARMEN gondola while also respecting the degrees of freedom required to track the desired stars for the science aspect of the HiCIBaS project (the latter is discussed in Section 2.3.3). However, five major factors influenced the physical dimensions and geometry of the design:

1. Implementing the "three-axes" design concept that was imposed by the optical system and pointing system (discussed in Section 2.3.2).
2. Positioning of the optical components (discussed in Section 2.3.2).
3. Respecting the weight limit imposed by CNES (discussed in Section 2.3.4).
4. Achieving the rigidity required to withstand the increased loads experienced at balloon separation and landing (discussed in Section 2.4).
5. Accommodating the pointing system's motors and the front-end optical components.

Figure 3 provides a look at the final design of the mount structure and its major components.

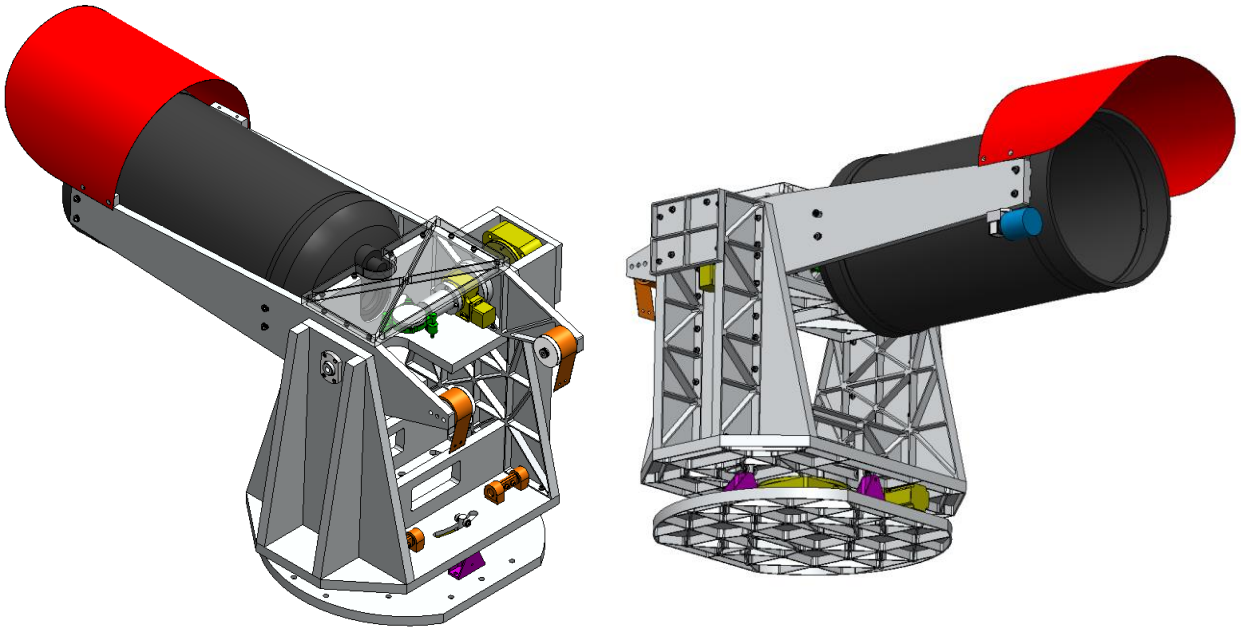

Figure 3: Final design of the HiCIBaS mount structure

To comment on some of the components of the design, the components of the mount structure in Figure 1 have been color-coded:

- Red: Shield (made of 6061-T6 aluminum alloy) for jettisoned stainless-steel balls during descent.
- Black: 14" Schmidt-Cassegrain telescope (Celestron: C14-AF-XLT) used to collect the light required to perform science and tracking tasks.
- Green: Mirror mount (ThorLabs: POLARIS-K3S5) housing the 2" Nasmyth mirror; aptly named for its purpose of guiding the incoming light (from the telescope) straight downwards and towards the rest of the optical system.
- Yellow: Rotary stage motors (Newmark: RM-3, RM-5, RM-8) used to deliver the arcsecond precision desired in azimuth and altitude.
- Blue: CCD camera (IDS: UI-3060CP Rev.2) and scope for the pointing system used to provide a wider view of the sky, and to locate and track the desired star(s).
- Light Grey: Alt-Az mount structure (made of 6061-T6 aluminum alloy) using a bracketed design that is made to be rigid and lightweight.
- Orange: Constant-force springs (McMaster: 9293K14) used to balance the telescope on the altitude axis to relieve stress on the altitude axis' rotary stage motor (RM-5).
- Purple: Support posts (made of 6061-T6 aluminum) to reduce impact loads on RM-8 motor during separation and landing events.

Not shown in Figure 3 are the deep groove ball bearings that are used to support the top portion of the structure and the telescope and allow free rotation on the altitude axis; the grease in these bearings are replaced with vacuum-compatible grease to survive the environmental conditions of the stratosphere.

1.3.2 Optical Design Considerations

This section aims to show a more in-depth look at the considerations made for the optical system in the design phase; in the process, it will also show conformance to Requirements 1-5 that were defined to ensure those considerations are met.

The mount structure is simply a means for the pointing system to accomplish its task of tracking the target star so that the optical system can perform the science of the mission. In that regard, the optical system has the most influence (top-level) on the mechanical design of the mount structure, as mentioned in section 2.3.1, making it a driving factor.

The first major consideration for the optical system is the “three-axes” concept. This concept involves intersecting the optical axis of the telescope and the rotational axes of the altitude and azimuth motors onto a single mirror (the aforementioned “Nasmyth” mirror), as shown in Figure 4. Attached to this design concept is the precision to which the axes must intersect, as defined in Requirements 1-3.

This concept serves one major purpose: to render the mount and “front-end” optical design fixed for future missions, allowing the “back-end” optical system to be modifiable or even replaced by entirely different optical systems (turnkey operation). In other words, different optical missions could be developed in parallel and flown during the same or subsequent flight campaigns. This would also facilitate the design process since half of the mechanical design would be complete, lessening the time needed to develop a payload.

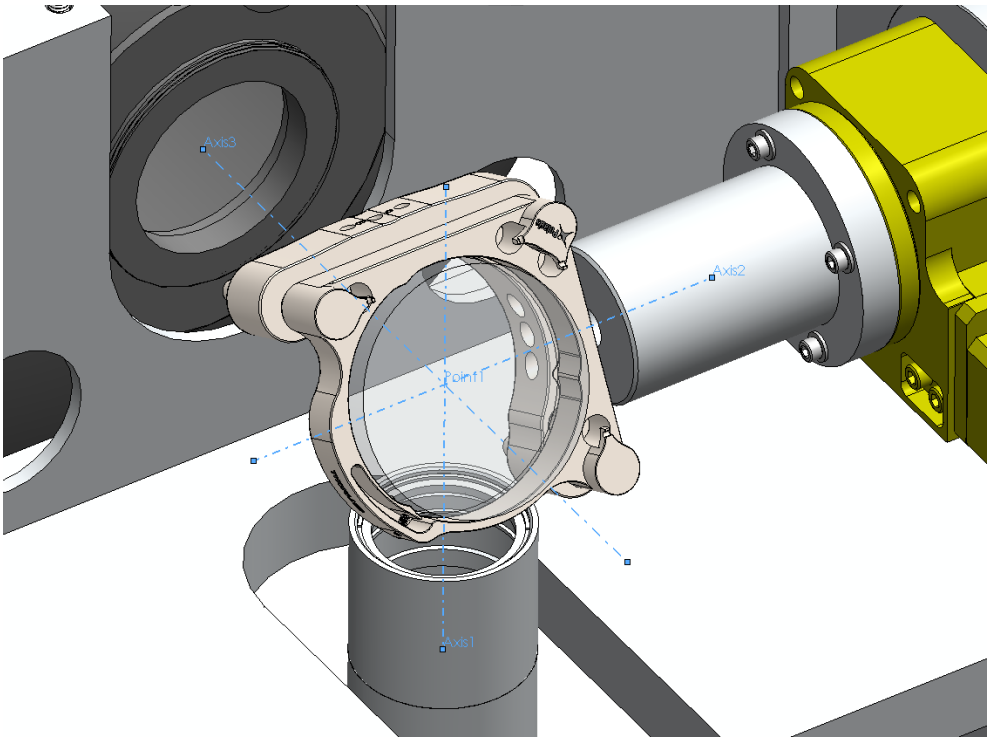

Figure 4: Intersection of the three main axes on the Nasmyth mirror

The optics team was able to confirm during the testing phase that the three axes intersected as desired, which gives validation for the conformance to Requirements 1-3.

The second major consideration for the optical system is the positioning of various optical and mechanical elements. Most notably, for the placement of the Nasmyth mirror, as defined by Requirement 4 and as seen in Figure 5, and the movement of the mount's back side during operation. Although these seem relatively minor, these two constraints (coupled with the three-axes concept) made the design of the structure difficult. On one hand, the placement of the Nasmyth mirror causes the center of gravity to be further from the center of rotation of the structure and elongating the overall length of the structure. On the other hand, to ensure that the structure does not intersect the optical path, the opposite side of the structure is restricted in length. The result is an asymmetric structure that would require more counterweights to be added to counteract the weight of the telescope that is further away. This was eventually mitigated using the constant-force springs solution mentioned in Section 2.3.1, it is discussed at length in Section 2.4.4.

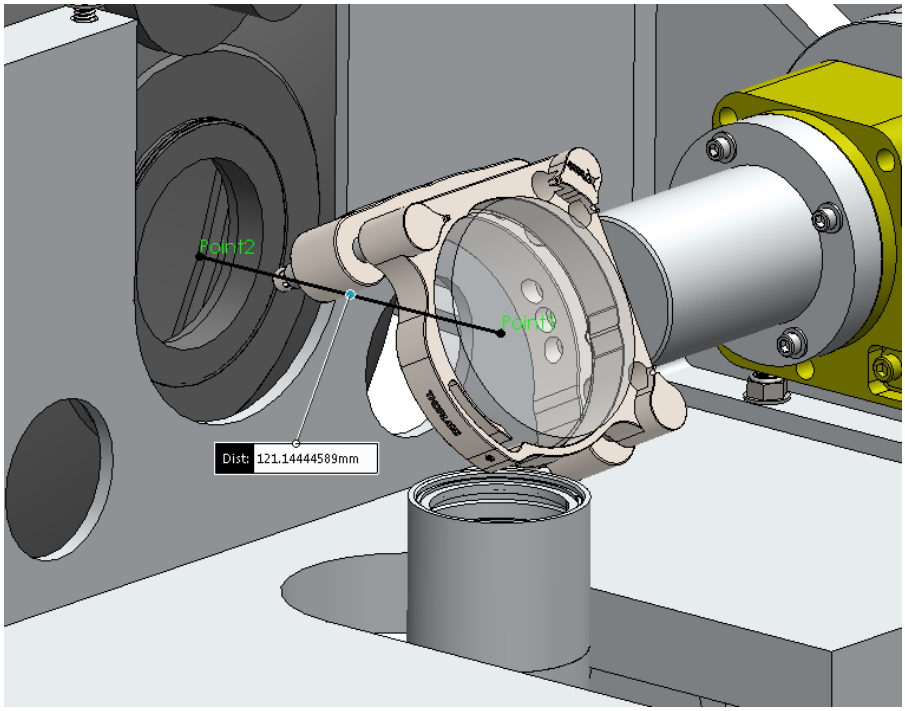

Figure 5: Positioning of the Nasmyth mirror in relation to the telescope's flange

1.3.3 Pointing System Considerations

This section will show the range capabilities of the telescope mount structure and the clearance from the gondola structure at all extremities.

The pointing system directly impacts optical performance and, therefore, the science of the mission. The mount structure must be designed, therefore, to accommodate the pointing system's needs so that the optical system can perform the science without restrictions from internal systems. In order to track the targeted stars, the pointing system requires specific degrees of freedom: ±20° in the azimuth direction and -20° to +60° in the

altitude direction. For safety concerns, a clearance of 20 mm at all extremities of these ranges must be met, as well.

Figures 6, 7, and 8 show the required range capabilities of the mount structure and the clearance from the gondola structure for ±20° azimuth, 60° altitude, and -20° altitude, respectively.

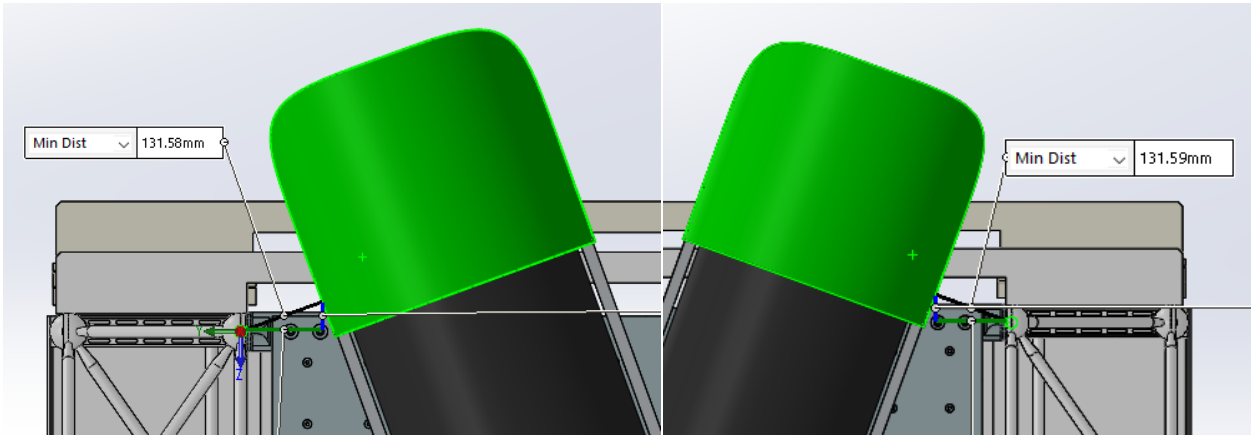

Figure 6: Clearance between mount structure (at ±20◦ azimuth positions) and gondola structure

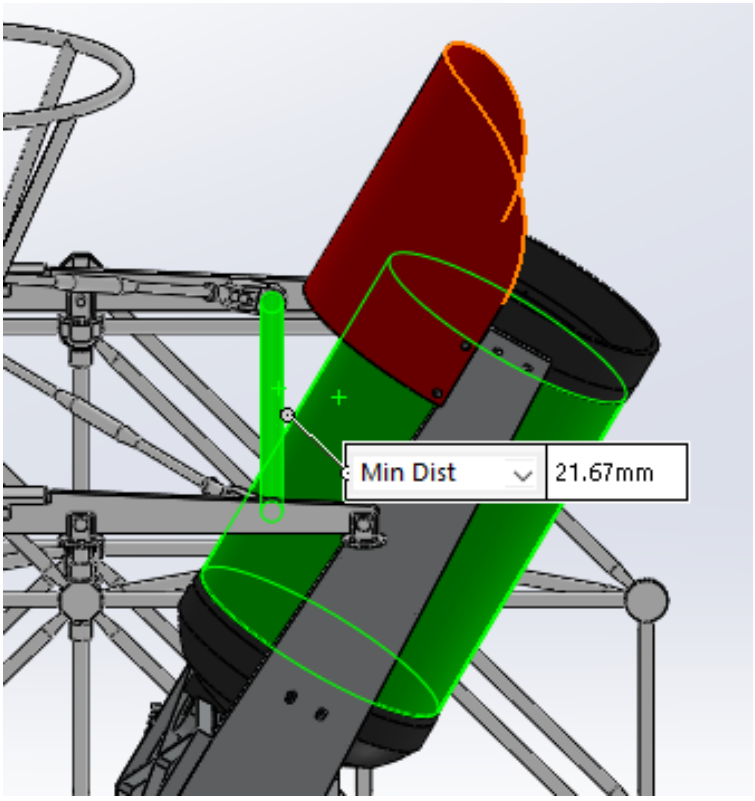

Figure 7: Clearance between mount structure (at 60° altitude position) and gondola structure

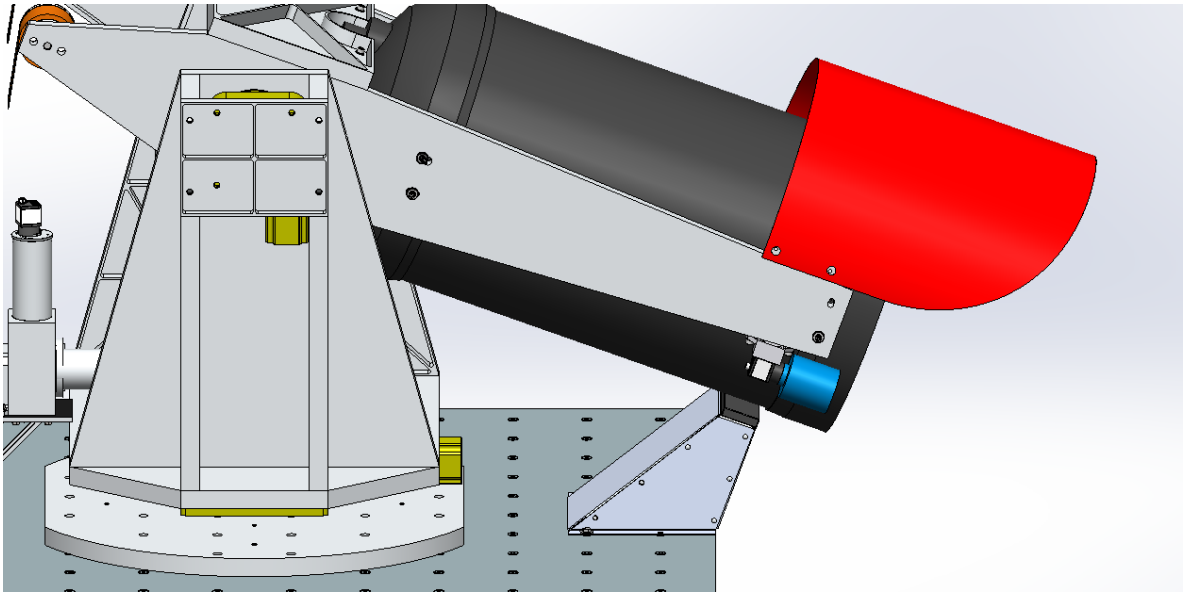

Figure 8: Mount structure descent position (-20° altitude, 0° azimuth)

The actual degrees of freedom of the mount structure and clearances from the gondola structure were confirmed to be accurate to those shown in Figure 6-8 during integration and testing to a magnitude of ±2 mm. This discrepancy was expected and comes from the positional tolerance of the gondola's floor and the positional adjustment of the gondola's floor needed for optical alignment. In all cases, however, the clearance was confirmed to be greater than or equal to 20 mm, the minimum desired clearance. Requirements 6-8 were, therefore, satisfied during the design phase and validated during integration and testing.

1.3.4 Overall Geometry and Positioning

This section will show the overall geometry and dimensions of the telescope mount structure and its placement in the CARMEN gondola.

Figures 9 and 10 demonstrate the overall dimensions of the entire mount structure at 0° altitude and azimuth. Figure 11 shows the positioning of the interface plate and the M6 inserts that are engaged on the CARMEN gondola's floor; this is important information for CNES to assess the mount structure's impact on the weight balance for the gondola. Figure 12 shows how far the telescope clears the edge of the gondola; there was no constraints imposed for this, but it is information that was requested by the CSA for safety reasons.

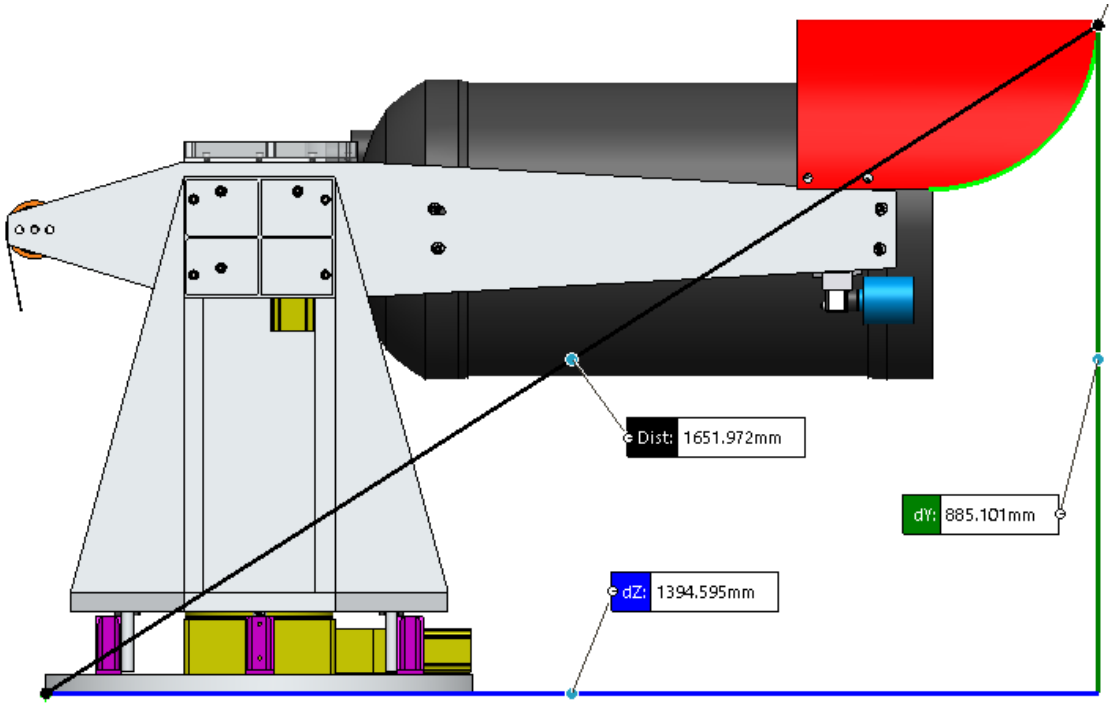

Figure 9: Length and height of mount structure at 0° altitude and azimuth position

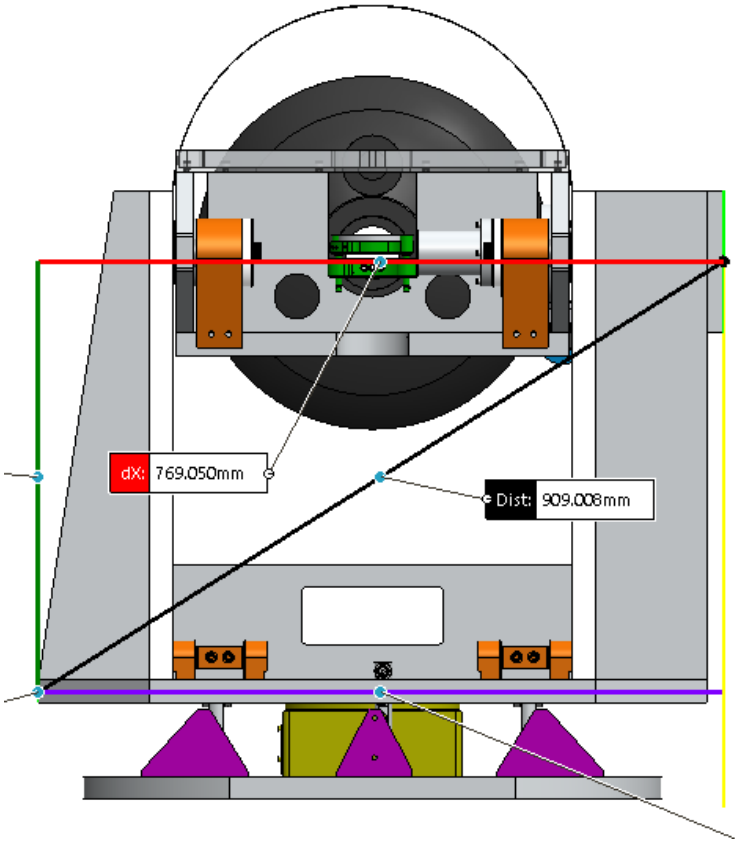

Figure 10: Width of mount structure at 0° altitude and azimuth position

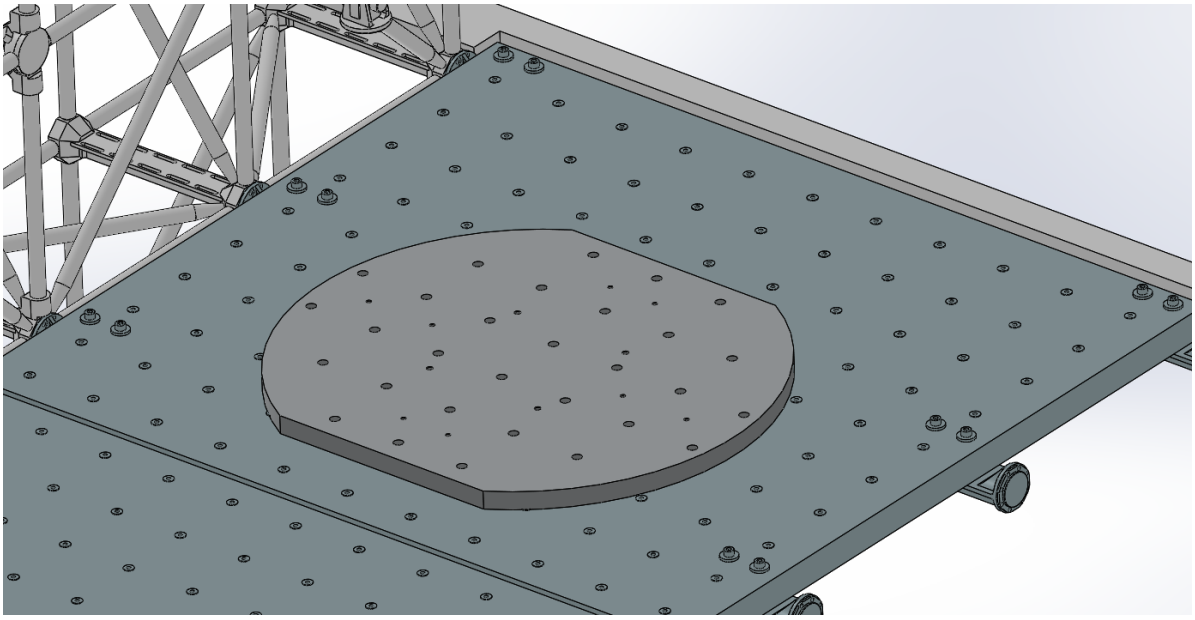

Figure 11: Position of mount structure's interface plate on gondola's front floor

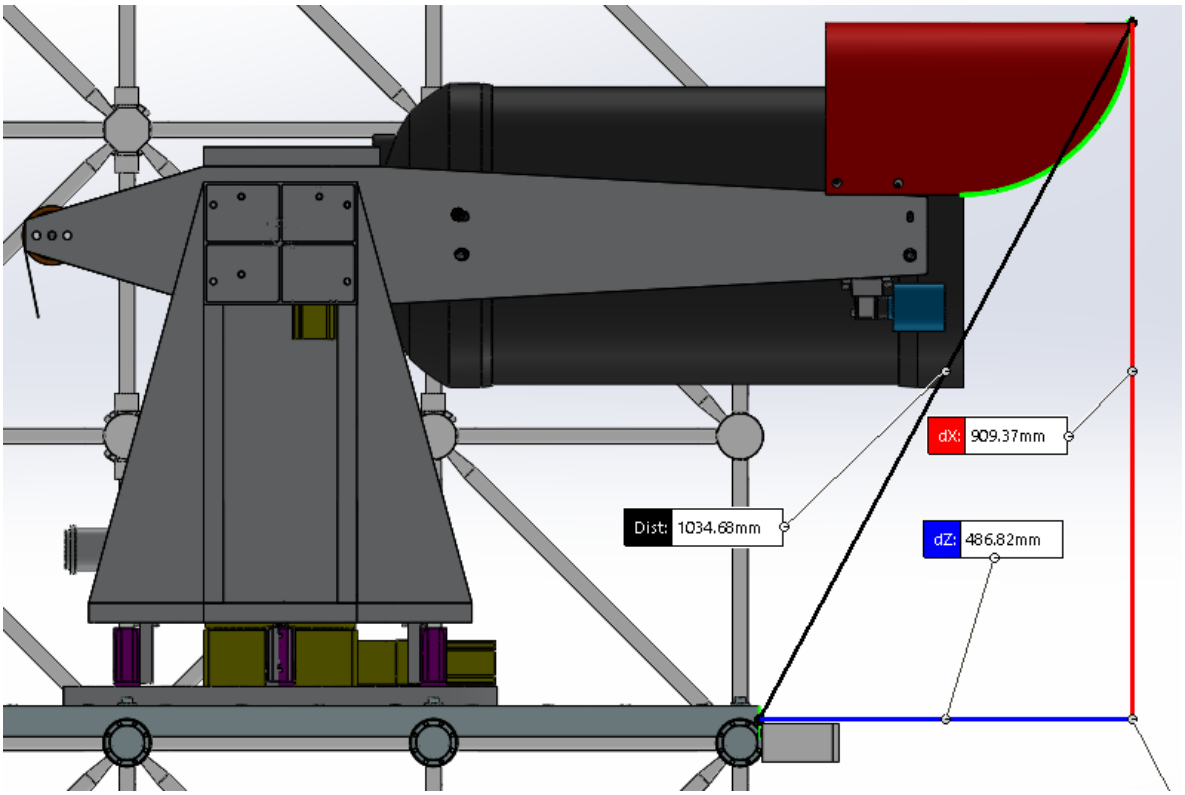

Figure 12: Horizontal clearance of mount structure from the edge of CARMEN's front floor

1.3.5 Weight and Center of Gravity (CG) Position

This section will provide a breakdown of the weight supported by the front floor of the CARMEN gondola; it will serve to demonstrate conformance to Requirement 9. The front floor will be occupied by the mount structure assembly and the telescope descent support; the breakdown provided in this section will show the weight contribution of the various main parts of the mount structure.

The weight distribution and CAD model versus actual structure weight difference is demonstrated by Table 2. Note that there is a ~6 kg difference between the actual weight (measured) and the CAD weight (expected). Since the entire telescope structure was measured while fully assembled, the origin of this discrepancy is unclear. However, it is most likely a result of the lower material density of the actual mount structure (i.e. the bulk of the mass) than was inputted, and estimated, in the CAD model.

Figures 9 and 10 provide information regarding the position of the CG of the mount structure with respect to its own physical center and with respect to the gondola's floor, respectively. As with the positioning of the mount structure, this is relevant information for CNES regarding weight balance of the gondola.

Table 2: Weight distribution of the mount structure components

Parts	CAD Weight (kg)	Actual Weight (kg)
Telescope	26.040	87.364
Telescope Brace Structure	10.233	
Standing Structure	22.478	
Rotary Motors (RM8, RM5, RM3)	18.600	
Rotating Baseplate	6.986	
Interface Plate	7.553	
Auxiliary Components (fasteners, supports, etc.)	1.182	
Total weight	**93.072**	**87.364**

CG position relative to the intersection point of mount's azimuth axis and the top surface of the CARMEN:

X: -22.68 mm
Y: 404.87 mm
Z: 172.03 mm

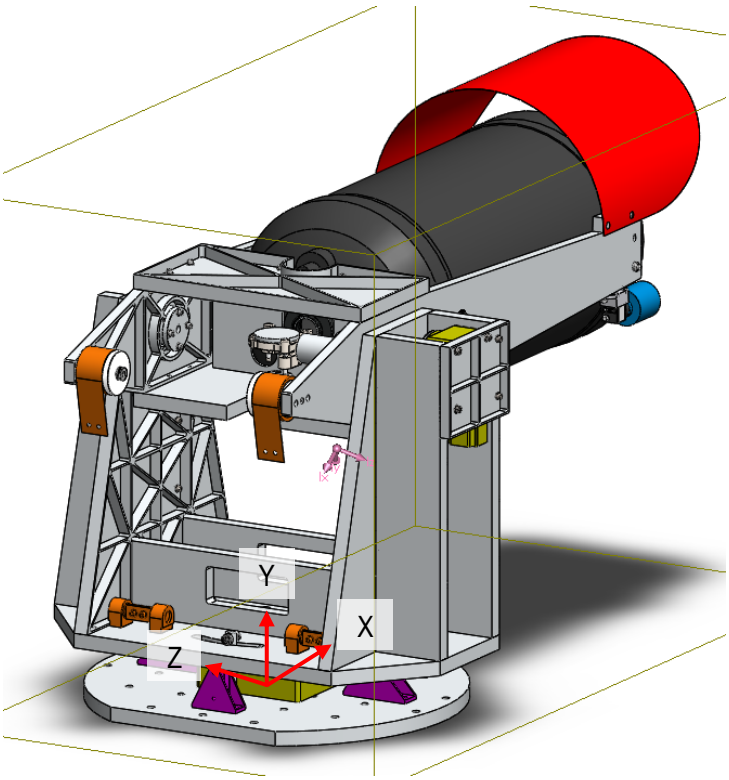

Figure 13: Center of gravity position of the standalone mount structure

CG position relative to indicated corner of CARMEN floor:

X: 534.30 mm
Y: 404.87 mm
Z: 567.03 mm

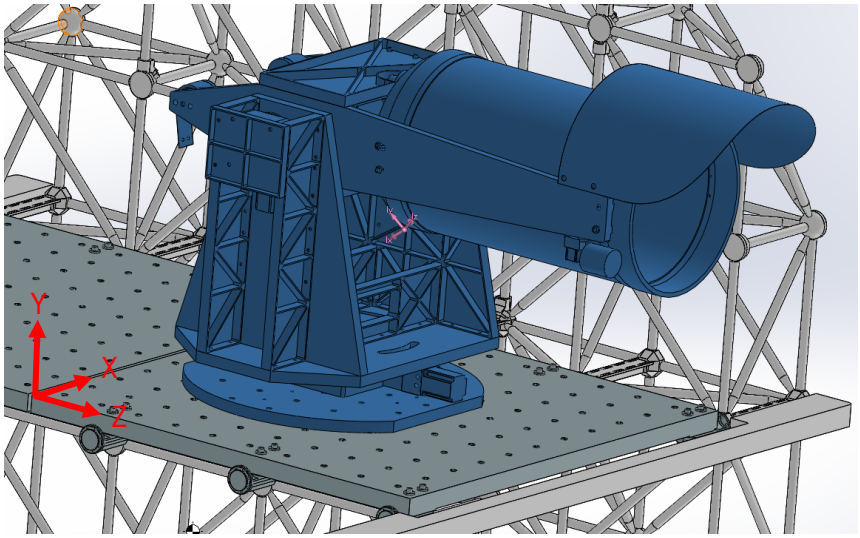

Figure 14: Center of gravity position of the mount structure in the CARMEN gondola

It is clear by looking at Table 2 that Requirement 9 was met during the design phase and validated to be conform in the testing phase, regardless of the discrepancy. Also, although it was not a requirement, Figures 9 and 10 demonstrate that the CG of the mount structure is very close to the center of the gondola's floor (only 34.3 mm away) between the walls of the gondola. This means that it's well-positioned in the gondola and the

structure itself has good symmetry, which is an important design feature when dealing with dynamic structures and increased load scenarios.

1.4 Evaluation of the Design

This section will demonstrate conformance to Requirements 10-16 pertaining to the general structural requirements of the mount structure and the load limit of the CARMEN M6 inserts, and increased loads experienced at landing. All designs in this section were made in SolidWorks 2017 and imported into ANSYS 18.0 for structural simulation. All calculations were done in accordance to section 5.4.2 of CSA's Safety Regulations for Aerostat Design and Operations document (CSA-STRATOS-RPT-0004-A-EN).

1.4.1 Numerical Analyses

The numerical analyses performed in this section all utilize the same strategy: removing parts of the structure surrounding the area of interest, making a free-body diagram, performing the necessary calculations to determine the resultant forces, torques, and moments, and, finally, evaluating the design.

1.4.1.1 RM-3 Motor – Moment Load Analysis

As mentioned in section 2.3.1, the RM-3 motor is responsible for controlling the orientation of the Nasmyth mirror in the altitude direction. The motor is mounted with its rotational axis being coaxial with the rotational axis of the mount structure's entire top portion (i.e. the rotational axis of the RM-5 motor). This section will demonstrate how the operational load limits of the RM-3 motor was respected. The complete datasheet for the motor is shown in Appendix 1, but, for convenience, the operational load limits are shown in Figure 15.

Load Characteristics

Normal Load (Fz)	20.4 kg (45 lbs)
Moment Load (Ma)	13.5 Nm (10 lb-ft)
Max. Torque (Tz)	4.5 Nm (3.3 lb-ft)

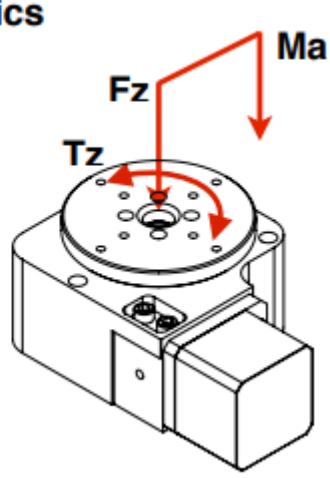

Figure 15: Operational load limits of the RM-3 motor

The main concern for the RM-3 motor is the moment load since it is holding 3 components in a cantilever configuration, as shown in Figure 16. Since the CG of these components is centered very close to the rotational axis and are of relatively low mass, the normal and torque loads are negligible in terms of criticality.

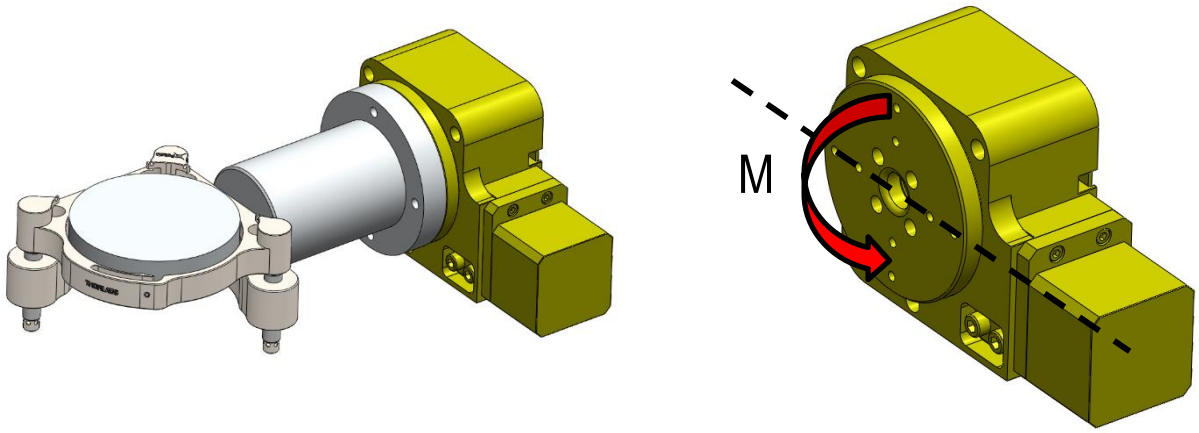

Figure 16: RM-3 assembly configuration (*left*) and resulting free-body diagram (*right*)

$$Total\ weight\ of\ supported\ components\ (F_{components}): 0.71\ kg = 6.9651\ N$$

$$Distance\ of\ total\ weight\ CG\ to\ RM-3\ (D_{CG\_components}) = 60.128\ mm = \ 0.060128\ m$$

$$Moment\ (M_{resultant}) = Force\ (F_{components}) \times Distance\ (D_{CG\_components}) = 0.4188\ Nm$$

$$\textbf{\textit{Moment Load}}: Factor\ of\ Safety\ (FoS) = \frac{13.5\ Nm}{0.4188\ Nm} = 32.23 \geq 1.2\ (minimum\ FoS\ desired)$$

With an FoS of 32.23, we have more than enough confidence to state that the operational load limits of the motor are respected.

1.4.1.2 RM-8 Motor – Normal and Moment Load Analysis

As mentioned in section 2.3.1, the RM-8 motor is responsible for controlling the orientation of the entire mount structure in the azimuth direction. This section will demonstrate how the operational load limits of the RM-8 motor was respected. The complete datasheet for the motor is shown in Appendix 1, but, for convenience, the operational load limits are shown in Figure 17.

Load Characteristics

Normal Load (Fz)	317 kg (700 lbs)
Moment Load (Ma)	135.5 Nm (100 lb-ft)
Max. Torque (Tz)	23 Nm (17 lb-ft)

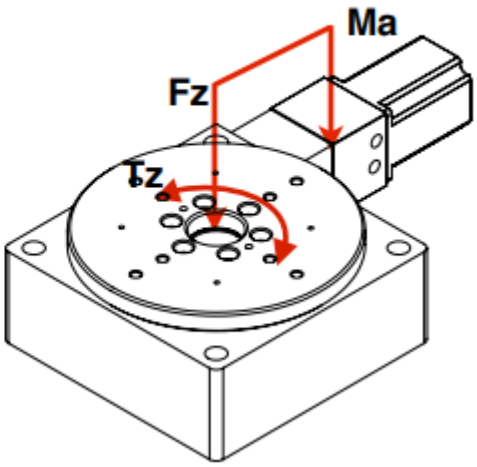

Figure 17: Operational load limits of the RM-8 motor

The main concerns for the RM-8 motor are the normal and moment loads since it is holding most of the components that make up the mount structure, as shown in Figure 18. Since there are no forces or moments causing a torque, the torque loads can be neglected in terms of criticality.

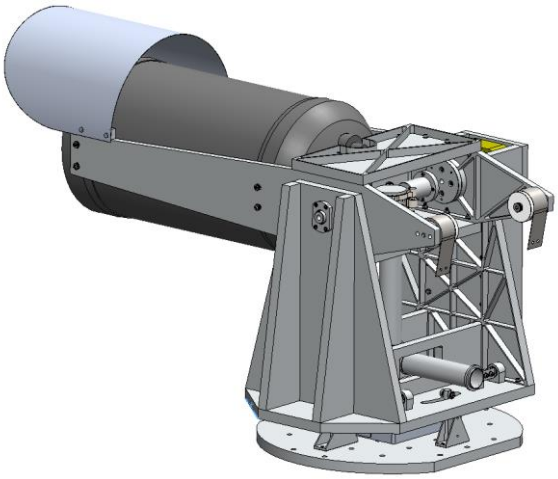

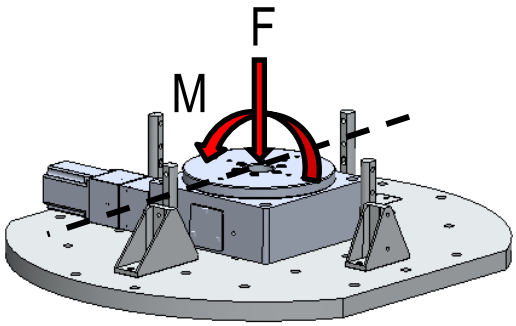

Figure 18: RM-8 assembly configuration (*left*) and resulting free-body diagram (*right*)

$$Total\ weight\ of\ supported\ components\ (F_{components}): 71.213\ kg = 698.6\ N$$

$$\boldsymbol{Normal\ Load}: Factor\ of\ Safety\ (FoS) = \frac{317\ kg}{71.213\ kg} = 4.451 \geq 1.2\ (minimum\ FoS\ desired)$$

$$Distance\ of\ total\ weight\ CG\ to\ RM3\ (D_{CG\_components}) = 150.712\ mm = \ 0.150712\ m$$

$$Moment\ (M_{resultant}) = Force\ (F_{components}) \times Distance\ (D_{CG\_components}) = 105.29\ Nm$$

$$\boldsymbol{Moment\ Load}: Factor\ of\ Safety\ (FoS) = \frac{135.5\ Nm}{105.29\ Nm} = 1.287 \geq 1.2\ (minimum\ FoS\ desired)$$

With FoS's of 4.451 and 1.287 for the normal and moment loads, respectively, we have enough confidence to state that the operational load limits of the motor are respected *for normal operation*. For impact during landing, the increased load felt (up to 15 g) would drop our FoS below 1.2 for both limits. In order to avoid this, support posts were integrated in the design to transfer the impact to the interface plate and gondola floor below and, consequently, relieve the RM-8 motor of this increased load.

1.4.1.3 Altitude-Direction Coupling – Torque Load Analysis

As mentioned in section 2.3.1, the altitude-direction coupling is responsible for transferring the torque from the RM-5 motor to the top portion of the mount structure (i.e. the structure that supports the telescope), as seen in Figure 19. In other words, the RM-5 motor controls the movement of the top portion of the mount structure in the altitude direction. Since the top portion of the mount structure is supported by bearings on both sides, the normal loads experienced by the RM-5 motor itself are negligible in terms of criticality; however, the coupling still encounters a significant torque load that must be considered. Therefore, this section will show the analysis that determined the maximum torque that would be experienced by the coupling, to compare it to how much it is designed to handle. The complete datasheet for the coupling and RM-5 motor are shown in Appendix 1, but, for convenience, the allowable torque limit for the coupling is 10 Nm and the maximum torque output for the RM-5 motor is 12.5 Nm; therefore, the coupling is the bottleneck of the design.

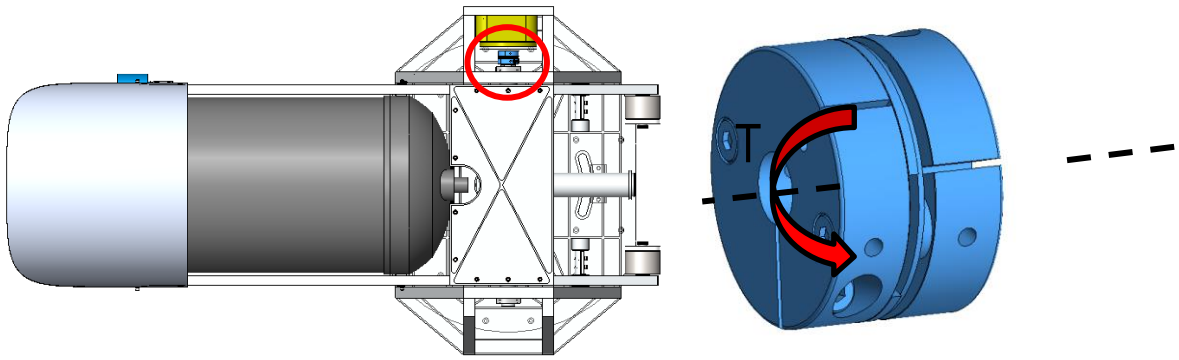

Figure 19: RM-5 coupling assembly configuration (*left*) and resulting free-body diagram (*right*)

We start with a balance of forces of the top portion of the structure to determine the resultant torque to apply to the coupling:

$$Load\ applied\ due\ to\ spring\ tension\ (F_{spring}) = 18.55\ kg = 182\ N$$

$$CG\ distance\ from\ rotational\ axis\ (D_{CG\_spring}) = 0.298\ m$$

$$Resultant\ torque\ (T_{spring}) = Force\ (F_{spring}) \times Distance\ (D_{CG\_spring}) = \ 54.236\ Nm$$

$$Load\ applied\ due\ to\ weight\ of\ telescope\ (F_{telescope}) = 26.04\ kg = 255.45\ \ N$$

$$CG\ distance\ from\ rotational\ axis\ (D_{CG\_telescope}) = 0.244\ m$$

$$Resultant\ torque\ (T_{telescope}) = Force\ (F_{telescope}) \times Distance\ (D_{CG\_telescope}) = \ 62.33\ Nm$$

$$Resultant\ torque\ on\ the\ coupling\ (T_{resultant}) = \ 62.33 - 54.236 = 8.094\ Nm$$

$$\textbf{\textit{Torque Load}}: Factor\ of\ Safety\ (FoS) = \frac{10\ Nm}{8.094\ Nm} = 1.235 \geq 1.2\ (minimum\ FoS\ desired)$$

With an FoS of 1.235, we have enough confidence to state that the operational load limit of the coupling is respected.

1.4.2 Simulation Analyses

This section will highlight the simulations performed for various critical parts of the mount structure, followed by brief discussions on the results.

The simulations performed in this section utilize a similar strategy as seen for the numerical analyses in Section 2.4.1: simplifying the structure surrounding the area of interest in the CAD model (discussed in Section 2.4.2.1), applying the appropriate parameters, constraints, and loads (discussed in Section 2.4.2.1), running the simulation, and, finally, analyzing the accuracy of the results (discussed in Section 2.4.2.6).

1.4.2.1 General Simulation Setup and Analysis

1.4.2.1.1 Simulation Setup

The primary goal of this section is to build confidence in the setup of the simulations performed. More specifically, to build confidence in the simulation model's preparation and the parameters used. This section will outline the setup of the simulation by describing the general setup strategy, the input parameters, the parameter values, and the results expected.

To begin, the type of simulation chosen was the explicit dynamics simulation. This decision is the most appropriate since the loads experienced by the structure are *impact* loads. The general strategy for the simulations was to simplify the model as much as possible by removing parts to save simulation time, while retaining all the parts that may have a significant impact on the results. For some simulations, removing the parts also improved the accuracy of the simulation model. For example, the telescope arms and standing structure (Sections 2.4.2.1.4 and 2.4.2.1.5) were separated because the interaction between the two proved difficult to model correctly. To compensate, they were separated and constrained accordingly in each of their simulation conditions. All the parts that were removed were replaced with a single point mass located at the CG of all those parts combined and applied to the areas that they were connected to.

The next step was to ensure that the *meshing* of the components was well-generated. Meshing is the practice of breaking up a component into small pieces, called *elements*, to be solved by a finite element analysis through the software's numerical solver. The meshing of components will directly impact the accuracy of the results. The overall goal is to generate a mesh that is fine enough to deliver accurate results, but coarse enough to minimize simulation time. For the general components that were typically larger, the mesh sizes were left to

the default sizes (up to 20 mm) determined by the software. If a load-bearing component or area was close to the critical path, or expected critical path, of the stress, mesh sizes were refined down to 0.1 to 5 mm. Mesh sizes were also refined for areas that presented higher level of structural error or lower levels of mesh quality, as discussed in Section 2.4.2.2. This was also the case for geometries that were more complex. Again, mesh sizes can be seen in Figures 20-24 for each simulation performed.

With the simulation model established, the loads of the simulation can be applied. In order to satisfy Requirements 11-16, the landing scenario is the determining factor for the loads applied since it is the worst-case scenario. Therefore, an acceleration load was applied to the simulation model, with 15 g in the vertical direction and 6.8 g in the lateral direction.

With the loads applied, the constraints must also be applied; this varied from simulation to simulation. For example, for the standing structure, the bottom of the base plate was fixed at the location of the bolts that held it in place and the area that it was resting on. For the interface plate, the bolts were fixed in place themselves. For the telescope mounting bolts simulation, the telescope arm was fixed. The constraints were made to simulate the physical model as accurately as possible.

Finally, the results desired must be defined. Again, this varies simulation to simulation. For most of them, the Von-Mises stress is the most important data because it can be used to show conformance to Requirements 14-16 and is, widely considered to be the most accurate means of determining the structural integrity of a ductile-material structure, since it is used to predict yield behavior. For the interface plate, where the force on the bolts was of prime concern, the force reactions was the desired data. In both cases, structural error is another result that was desired in order to perform one of the V&V activities outlined in Section 2.4.2.2.

1.4.2.2 Analysis Setup

In order to prepare the following sections for the results of the simulations performed, some context must be provided about the CSA's Safety Data Pack (CSA-STRATOS-RPT-0004-A-EN), which can be found, in partial format, in Appendix 3, and how it outlines the approach to be taken to satisfy Requirements 14-16.

Section 5.3.2 of the CSA's Safety Data Pack outlines the steps taken to prove structural integrity of a part using the maximum stress simulated (LL). This stress will be the Von-Mises stress since it better predicts the behavior of ductile metals. Safety factors defined by the CSA are then applied to this value to determine three design loads; the same three design loads required to satisfy Requirements 14-16 that can be found for each simulation. The following are the list of safety factors and the equations required to determine the design loads.

Safety factors as defined by the CSA:

- Model factor (KM) = 1.4
- Project factor (KP) = 1.15
- Design factor (FOSD) = 1.2
- Yield factor (FOSY) = 1.25
- Ultimate factor (FOSU) = 1.5

Design load equations:

- DLL (Design Limit Load) = LL × KP × KM
- DYL (Design Yield Load) = DLL × FOSY
- DUL (Design Ultimate Load) = DLL × FOSU

1.4.2.2.1 Telescope Arm Structure and Screws (Top Section) – Stress Analysis

The telescope arm structure is the top section of the mount structure. It holds the telescope on one end and uses constant-force springs on the other end to balance the structure on the elevation axis. This structure was deemed important to analyze since it is holding the telescope (which is about a quarter of the total weight of the structure) and presents a big risk in the event of failure. There are two areas of interest for this simulation: the maximum stress on the structure itself and the stresses experienced by the eight screws supporting the telescope.

Using the strategy and parameters mentioned in Section 2.4.2.1, the simulation was performed, and the results are shown in Figure 20 and Table 3.

Figure 20 shows the maximum stress experienced by the structure of the telescope arms and the analysis that follows is done using the CSA's criteria mentioned in Section 2.4.2.2.

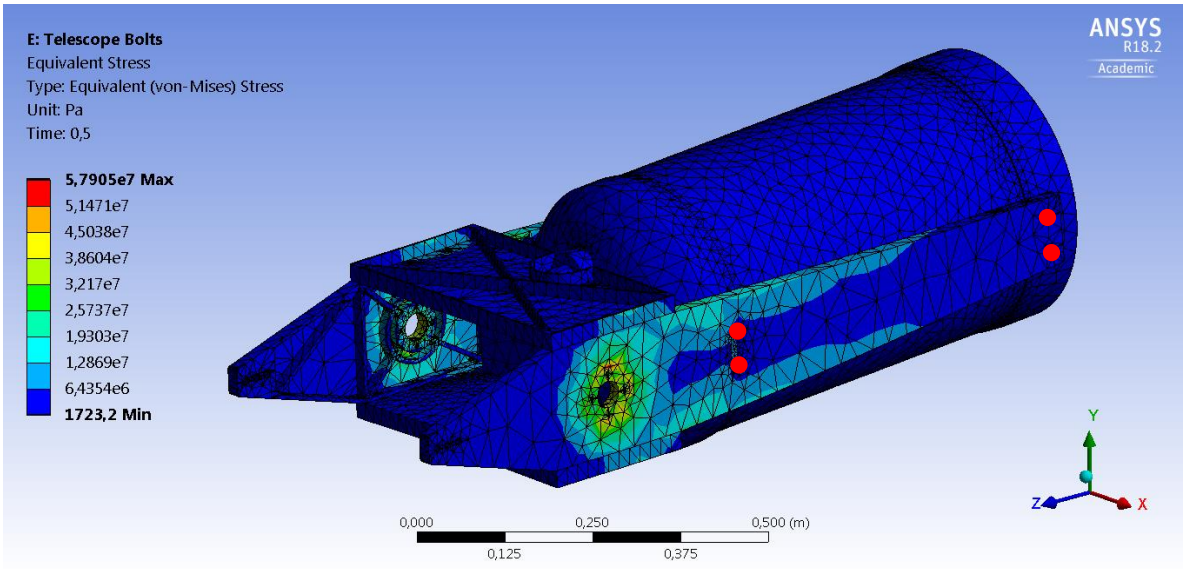

Figure 20: Maximum Von-Mises stress due to impact simulation of telescope arm structure

$$Design\ Limit\ Load\ (DLL) = LL \times \mathrm{KM} \times \mathrm{KP} \times \mathrm{FOSD} = 55.2 \times 1.4 \times 1.15 \times 1.2 = 106.65\ \mathrm{MPa}$$

$$\boldsymbol{Design\ Yield\ Load\ (DYL)} = DLL \times \mathrm{FOSY} = 106.65 \times 1.25 = \mathbf{133.31\ MPa} \leq \mathbf{276\ MPa\ (YL)}$$
$$\boldsymbol{Design\ Ult.\ Load\ (DUL)} = DLL \times \mathrm{FOSU} = 106.65 \times 1.5 = \mathbf{159.98\ MPa} \leq \mathbf{310\ MPa\ (UL)}$$

$$\boldsymbol{General\ Safety\ Factor\ Check}: LL \times 1.5 = \times 1.5 = \mathbf{82.8\ MPa} \leq \mathbf{276\ MPa\ (YL)}$$

In order to satisfy Requirements 14-16, we can compare these results to the material's tensile yield strength (YL). We see that the values are less than the material's tensile yield strength (276 MPa) on all counts (DYL, DUL, and the general safety factor check) so the design is sufficiently strong; the results are summarized in table format in Section 2.4.3.2.

Table 3 summarizes the maximum stress experienced by each of the screws supporting the telescope with a comparison to their shear strength. The location of the screws is indicated by red dots in Figure 20.

Table 3: Maximum stresses experienced by the screws supporting the telescope

Location	Maximum Shear Stress Experienced (MPa)	Shear Strength of Screws (MPa)	Factor of Safety
Front	7.215	1172.11	162.45
	7.218		162.39
	6.940		168.89
	7.622		153.78
Back	11.228		104.39
	11.712		100.08
	10.72		109.34
	11.515		101.79

With the maximum shear stress experienced by the screws significantly lower than their shear strength, it can be concluded that the 8 screws are sufficiently strong and distribute the load effectively enough to be safe. It is worth noting that the screws closer to the elevation axis are experiencing loads that are about 58% larger than those in the front. This is expected knowing that the center of gravity is closer to those screws but still interesting for future designs.

Standing Structure and Base (Mid Section) – Stress Analysis

The standing structure is the mid-level portion of the mount structure. This part of the design is an essential to the overall structural integrity of the mount. It was deemed important to analyze since it is supporting the entire top-portion of the structure (which is close to half of the weight of the entire mount), making it critical from a safety standpoint.

Using the strategy and parameters mentioned in Section 2.4.2.1, the simulation was performed, and the result is shown in Figure 21. The analysis that follows the simulation is done using the criteria mentioned in Section 2.4.2.2.

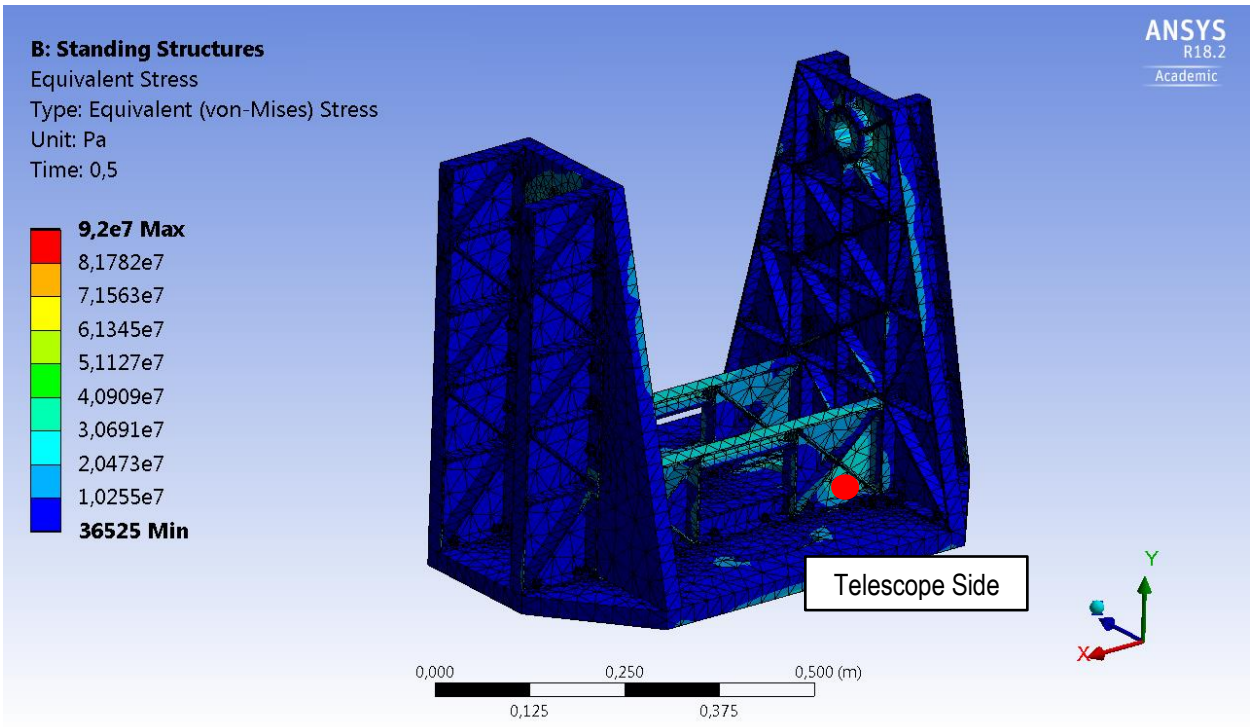

Figure 21: Maximum Von-Mises stress from the impact simulation of the standing structure

$$Design\ Limit\ Load\ (DLL) = LL \times \mathrm{KM} \times \mathrm{KP} \times \mathrm{FOSD} = 92.7 \times 1.4 \times 1.15 \times 1.2 = 179.10\ \mathrm{MPa}$$

$$\boldsymbol{Design\ Yield\ Load\ (DYL)} = DLL \times \mathrm{FOSY} = 179.10 \times 1.25 = \mathbf{223.88\ MPa} \leq \mathbf{276\ MPa\ (YL)}$$
$$\boldsymbol{Design\ Ult.\ Load\ (DUL)} = DLL \times \mathrm{FOSU} = 179.10 \times 1.5 = \mathbf{268.65\ MPa} \leq \mathbf{310\ MPa\ (UL)}$$

$$\boldsymbol{General\ Safety\ Factor\ Check}: LL \times 1.5 = 92.7 \times 1.5 = \mathbf{139.05\ MPa} \leq \mathbf{276\ MPa\ (YL)}$$

In order to satisfy Requirements 14-16, we can compare these results to the material's tensile yield strength (YL). We see that the values are less than the material's tensile yield strength (276 MPa) on all counts (DYL, DUL, and the general safety factor check) so we can conclude that the design is sufficiently strong and safe; the results are summarized in table format in Section 2.4.3.2.

1.4.2.2.2 Interface Plate Screws – Force Analysis

The interface plate screws are the screws that fix the payload (using the interface place) to the gondola's floor; there is a total of thirty M6 screws that are used for this as displayed in Figure 22. This section is relevant to improve the confidence in the load distribution across the gondola floor's inserts and to prove conformance to Requirements 11-13. It was deemed important to analyze since the screws are experiencing increased loads from the acceleration of the entire mount structure and because the gondola floor's inserts have never been subject to a payload of this size before.

Using the strategy and parameters mentioned in Section 2.4.2.1, the simulation was performed, and the results are shown in Table 4 with the maximum forces for each direction highlighted; for convenience, Figure 22 displays the interface plate simulation model with the assigned screws' numbers.

Table 4: Force reactions for the screws interfacing the mount structure to the gondola's floor

Assigned Screw #	X-direction Magnitude	Y-direction Magnitude	Z-direction Magnitude
	All values in Newtons (N)		
1	-109.63	3.3946	108.99
2	-31.658	166.95	714.9
3	98.384	5.1255	115.51
4	-19.278	2.4143	70.17
5	-33.866	5.1183	44.292
6	-18.7	158.71	-122.62
7	18.712	6.0592	57.288
8	16.556	2.431	85.737
9	-22.939	1.1726	81.6
10	-3.5519	-74.531	142.94
11	27.05	-0.58688	78.353
12	1.3641	2.6751	42.377
13	-28.384	-1.1575	90.254
14	4.8342	-93.871	136.02
15	20.057	-2.4342	96.993
16	92.492	-2.4627	124.62
17	23.62	-47.084	493.68
18	-75.732	-2.7468	118.79
19	3.35	2.7598	52.583
20	100.29	-3.8101	144.46
21	-18.636	-91.744	651.04
22	-120.07	-4.2205	162.92
23	35.77	2.1817	77.863
24	73.346	-0.24735	34.034
25	41.433	-266.43	-416.84
26	-65.093	-2.8386	46.076
27	-33.975	2.3176	96.376
28	159.65	1.3294	139.88
29	40.408	-260.5	1023.2
30	-160.03	-2.7682	158.78

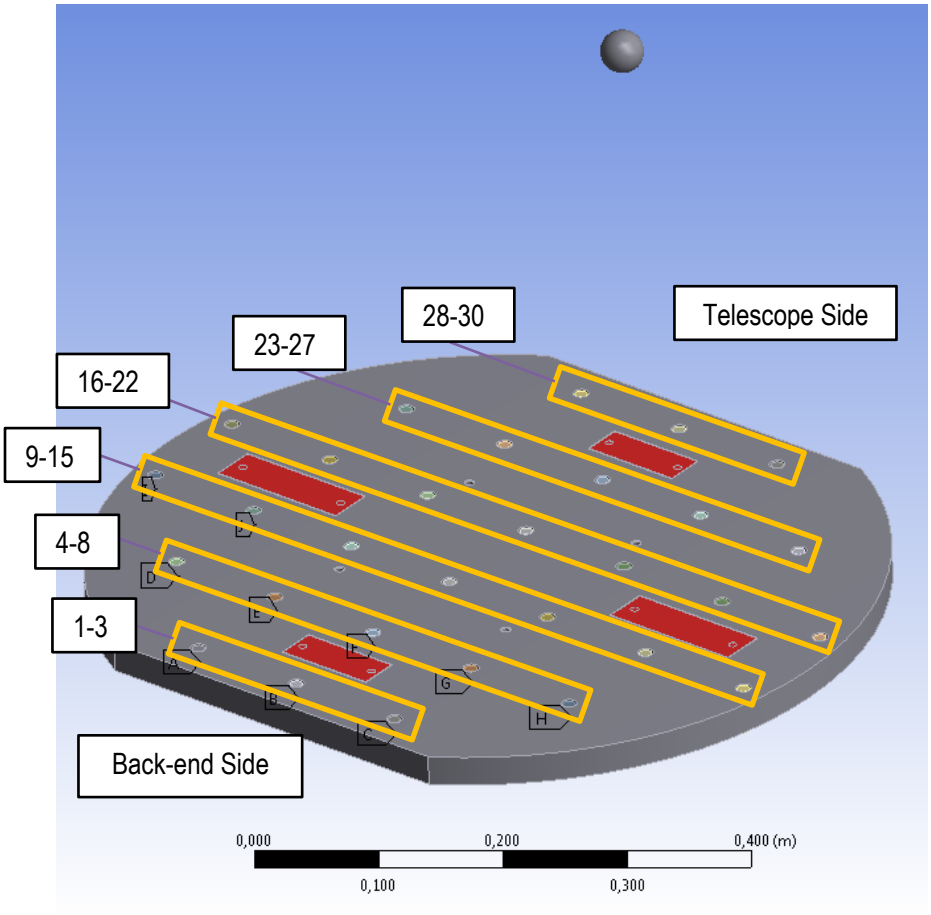

Figure 22: Interface plate with assigned numbering scheme for the insert screws

Application of standard safety factor to the maximum forces experienced in each direction:

$$\boldsymbol{X-direction}: 160.03 \times 1.2 = \boldsymbol{192.04\ N}$$
$$\boldsymbol{Y-direction}: 266.43 \times 1.2 = \boldsymbol{319.72\ N}$$
$$\boldsymbol{Z-direction}: 1023.2 \times 1.2 = \boldsymbol{1227.84\ N}$$

In order to satisfy Requirements 11 and 12, we can compare these maximum forces experienced to the limits defined in the requirements themselves. The values, after applying a standard safety factor of 1.2, are less than the values provided by CNES for the requirements. Since the maximum forces in each direction across all the screws are all below the limits, it is implied that the forces on all the screws, in all directions, are also below the limits. Therefore, we can conclude that Requirements 11 and 12 are satisfied.

In order to satisfy Requirement 13, however, further calculations must be made. Table 5 outlines the results of calculations performed in Excel that uses the equation defined in Requirement 13 to see if the forces experienced by each screw satisfy the criterion. The maximum normal load (P) is taken as the Y-direction force reaction and the maximum transverse load (Q) is taken as the vector sum of the X- and Z-direction forces.

Table 5: Verification of conformance of loads on each screw for the force equation criterion

Assigned Screw #	Load-derived Criterion Equation Result
1	0.000725
2	0.037958
3	0.000808
4	0.000297
5	0.000125
6	0.00746
7	0.000207
8	0.000443
9	0.0004
10	0.002673
11	0.000369
12	0.00011
13	0.00049
14	0.003405
15	0.000567
16	0.000935
17	0.015218
18	0.00085
19	0.000168
20	0.001257
21	0.027653
22	0.001599
23	0.000365
24	0.000323
25	0.028916
26	0.000257
27	0.000559
28	0.001532
29	0.080557
30	0.00154

With the largest result being 0.080557, it's clear that the criterion is met for all the screws. With this, we can conclude that the design satisfies Requirement 13 as well.

1.4.2.2.3 Full Structure (1G Static) – Stress Analysis

The top section and mid section of the mount design was analyzed separately for the worst-case impact load simulations because the interaction between the two can be difficult to model correctly. Separating them yields two simulations that are more accurate instead of a single inaccurate simulation resulting from a poorly constructed model. However, the full structure still requires a 1G static analysis. This analysis is important to assess how the mount structure behaves under its own weight while it is not moving. It is simulation that does not have a validation criterion, the main purpose is to find the critical areas in the design (the most stressed) and assess if the maximum stresses on those areas are reasonable.

Using the strategy and parameters mentioned in Section 2.4.2.1, the simulation was performed, and the results are shown in Figures 23 and 24.

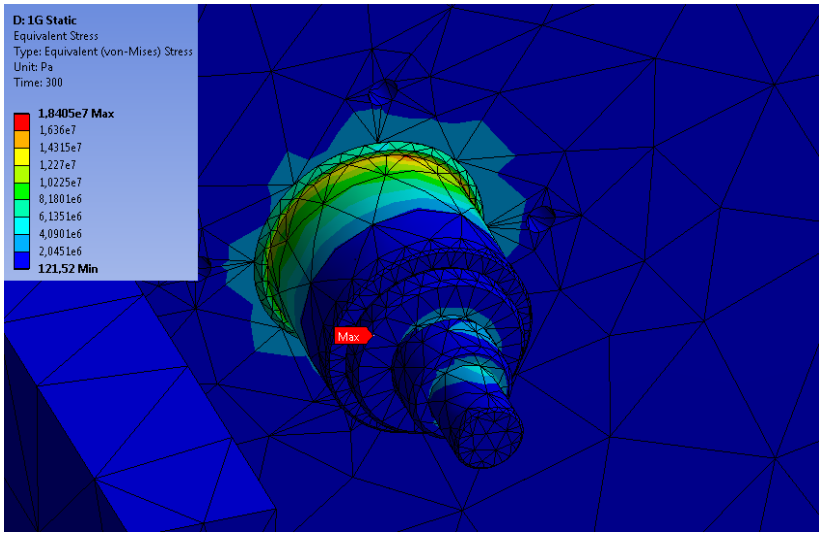

Figure 23: Maximum Von-Mises stress from the 1G static simulation of the structure

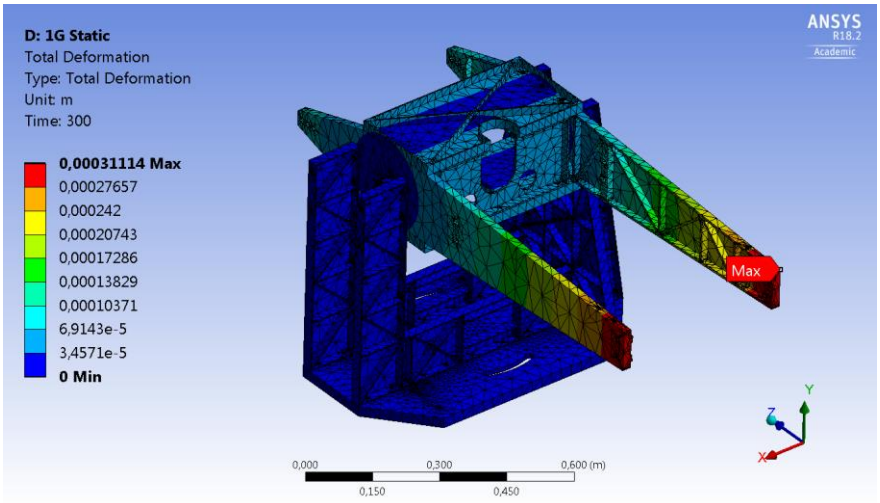

Figure 24: Maximum displacement from the 1G static simulation of the structure

The maximum stress from the 1G static test occurs on the shaft that connects the telescope arm to the coupling. This was expected since the shafts are supporting the weight of the entire top section of the mount. The stress induced by the weight of the mount is very low (18.4 MPa), though, and does not raise any concerns for failure under its own weight. This further lends to proving the structural integrity of the design.

The maximum deformation is more relevant for this simulation because it provides information that may directly affect the pointing system. A deformation of 0.311 mm can be observed at the ends of the telescope arms, which is very small compared to it's overall length and does not present a problem for the pointing system that has an auto-adjustment feature within the algorithm.

1.4.2.3 Verification and Validation (V&V) of Results

This section will demonstrate the measures taken post-simulation to build confidence in the simulation results.

There are numerous ways to check the validity of simulation results within ANSYS. For this simulation, 3 verification checks were performed: convergence, structural error, and mesh quality. All of these are, essentially, providing you with the same information (the accuracy of your results), but they confirm it in different ways and with different metrics.

The first check to perform is the convergence check. This is a broad scope check that provides information on how well the numerical solver was able to work through the finite element calculations. This is done by establishing a validation criterion by setting a predefined level of permissible error for the change in *stress* across elements and between timesteps. Typically, an error of 10-20% is acceptable for most applications; 10% was chosen for this simulation to be safe. ANSYS is then able to generate a convergence curve based on the numerical solver's ability to find an accurate solution. Whenever it can converge to an acceptable solution (in the acceptable amount of iterations), the curve should be below the curve of the validation criterion. This check was performed for all the simulations; the result for the standing structures simulation is displayed in Figure 25 with the criterion curve in blue and the convergence curve in purple.

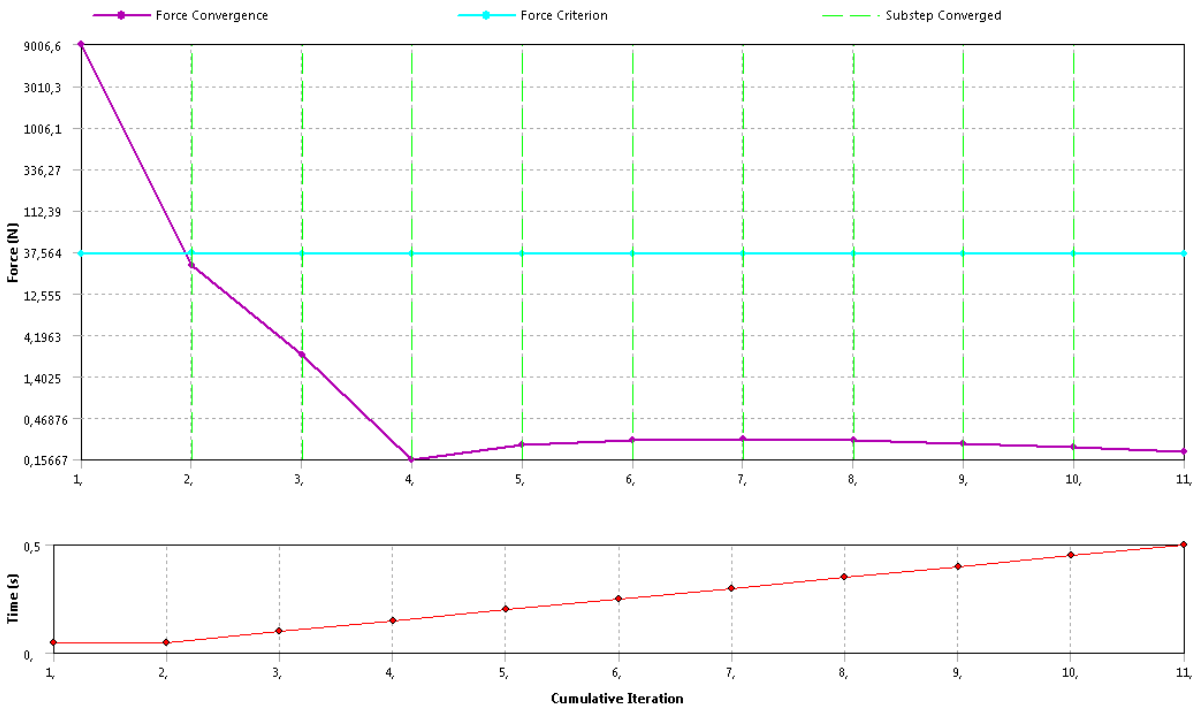

Figure 25: Stress convergence curve for the full-assembly structural simulation

The convergence curve is below the validation criterion curve for almost the entire duration of the simulation, which is a good indication that the next checks should yield positive results as well. If convergence problems were present, the next checks would be used to investigate the specific problem areas and find solutions accordingly; typically, the solution can be resolved by refining the mesh or changing element geometry in those problem areas.

The second check is the structural error check. This check is excellent for indicating the areas in the simulation model that require mesh refinement because of problems in the finite element calculations in those areas. It is, essentially, a more in-depth version of the convergence check. If specific areas, or even specific elements, are causing problems, it will take longer to converge, or will not converge at all and the structural error is able to display this. There were many problem areas with the original simulation models because of the bracketed design's curves. The mesh was refined in these areas and some elements were merged with adjacent elements to avoid the overlap of element areas. Across all simulations, a maximum structural error of 0.072 (7.2%) was achieved, which is within the accepted range (up to 10%) defined by ANSYS.

Lastly is the mesh quality check using the aspect ratio and element quality as metrics. The aspect ratio defines the degree to which elements are "stretched" in the mesh generation to fill out the simulation model; in other words. This can impact the simulation results because a large aspect ratio could cause mesh elements to span a large area in one direction. This can yield inaccurate results and impact the rest of the results in the numerical solver that follow that element's location. Typically, aspect ratio values under 10 is excellent, with larger aspect ratios (around 20) being accepted for elements outside the critical areas if they make up less than

10% of the total elements. Figure 26 demonstrates the distribution of the aspect ratios for the standing structures simulation model used.

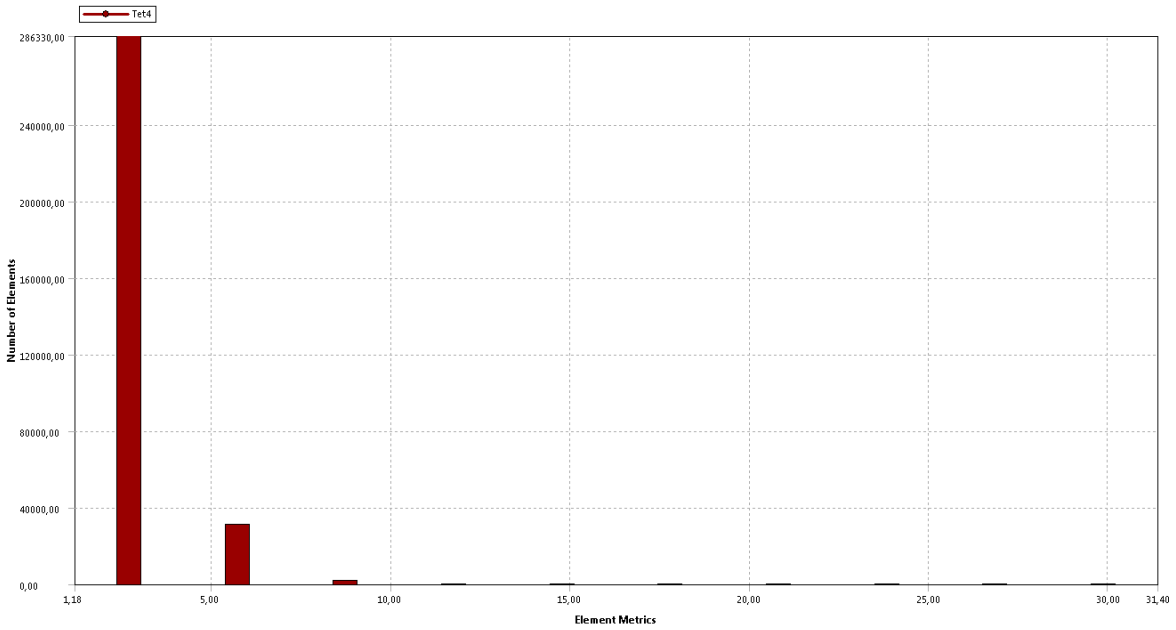

Figure 26: Distribution of aspect ratios of the standing structures simulation model

As observed, the aspect ratio of all the elements are below 10, indicating a great consistency in the shape of the elements. This check can be considered a success since it follows the criteria mentioned earlier.

Element quality is a more encompassing metric that is based on a ratio of the volume to the edge length. More specifically, it is determined by the following equation:

$$Element\ Quality = Shape\ Factor \times \frac{Volume}{\sqrt{[\sum(Edge\ Length)^2]^3}}$$

This is a check that is comparable to the aspect ratio in that it aims to check how stretched out the elements are. A value of 1 would imply that the element is a perfect cube, whereas a value close to zero would imply a shape that is flatter with some edge lengths much longer than others. This being the case, in order to have a good balance of edge lengths, an element quality larger than 0.30 is required. Figure 27 demonstrates the distribution of the element quality for all elements for the standing structures simulation model used.

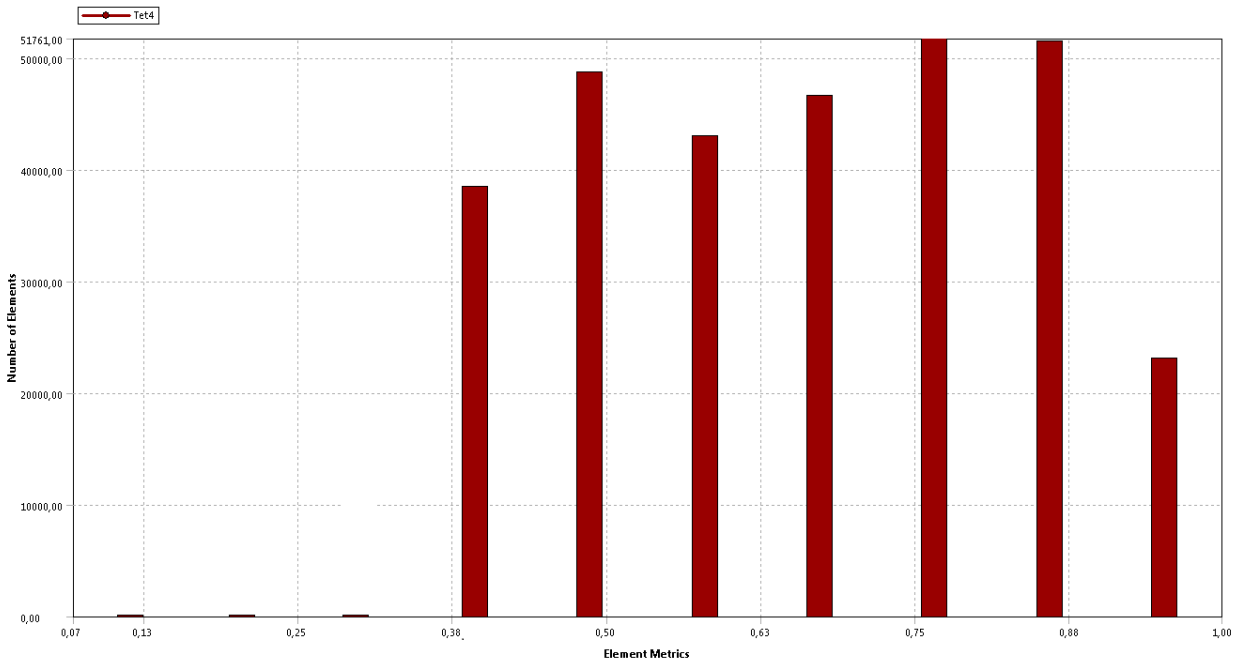

Figure 27: Distribution of element quality for the standing structures simulation model

As observed, the element quality of all the elements are above 0.30, which is also indicative of great geometry of the elements. This check can be considered a success since it also follows the criteria mentioned earlier.

1.4.2.4 Summary of Results

1.4.2.4.1 Numerical Analyses

Table 6: Summary of numerical results for the standing mount structure

Area	Stress Type	Analysis Result	Max Permissible	Factor of Safety	Conform?
RM-3 Motor	Normal Load (N)	Negligible	200.12	N/A	N/A
	Moment Load (N·m)	0.4188	13.5	32.23	Y
	Torque (N·m)	Negligible	4.50	N/A	N/A
RM-8 Motor	Normal Load (N)	698.6	3 109.77	4.451	Y
	Moment Load (N·m)	105.29	135.50	1.287	Y
	Torque (N·m)	Negligible	23	N/A	N/A
Altitude-Direction Coupling	Torque (N·m)	8.094	10	1.235	Y

1.4.2.4.2 Simulation Analyses

Table 7: Summary of simulation results for the standing mount structure

Area	Stress Type	Indicator	Sim. Result	Max Permissible	Conform?
Telescope Arm Structure	Von-Mises (MPa)	DYL	133.31	276	Y
		DUL	159.98	310	Y
Telescope Screws		N/A	11.712	1172.11	Y
Standing Structures (Mid-Portion)		DYL	221.45	276	Y
		DUL	265.74	310	Y
Full Structure		N/A	18.40	N/A	N/A
Interface Screws	Force (N)	Max X-Z	1035.7	4080	Y
		Max Y	266.43	1960	Y

1.4.3 Mission Performance

Although there aren't many quantitative means to measure the performance of the telescope mount, there is still room for discussion. This section will highlight specific subjects surrounding the telescope mount, provide more information about how they performed, and the problems encountered.

1.4.3.1 Structural Integrity

Based on inspection post-flight, the large structures proved to be well-designed. There was no major structural damage done to the mount itself, all parts could be reused for future missions, if desired. There are countless 1-mm diameter dents throughout the structure caused by the jettisoned stainless-steel balls used for altitude control, but it's not enough to impact the structural integrity of the design in a significant manner. For context, Figure 28 displays the type of landing environment that the payload landed in and withstood.

Figure 28: Landing environment of the gondola

The only data we have that can be used to measure the performance of the structure is the acceleration loads that were experienced by the gondola during the major events. CNES provided this data and the full graphs are available in Appendix 4; for convenience, however, Table 8 summarizes the maximum loads experienced at separation and at landing, along with the loads that the mount was designed to withstand for each.

Table 8: Maximum acceleration loads experienced at separation and landing

Scenario	Direction	Design Max. Load (g)	Measured Max. Load (g)
Landing	Vertical	15	10.47
	Lateral	6.8	4.43
Separation	Vertical	5	2.838
	Lateral	1.4	2.269

For the most part, the loads experienced were below the max loads the mount was designed to withstand. At separation, however, we can see that the maximum measured load in the lateral direction surpassed the maximum design load (2.269 g versus 1.4 g). Luckily, the structure was built to withstand up to 6.8 g in the lateral direction for the landing scenario. This data sets the benchmark not only for this specific design, but for the potential future designs that may be similar in geometry and size.

1.4.3.2 Interface Plate

The interface plate was a component that was heavily analyzed because this mission would be the first time the CARMEN gondola floors would be accommodating a payload of that size and weight. Although there are no means to quantify the performance of this plate, it warrants a quick mention because it was able to effectively distribute the loads experienced (as defined in Section 2.4.3.1). CNES was able to confirm post-flight that there was no damage done to the inserts that were engaged, providing more confidence in the design integrity of the interface plate. This implies that a future payload of similar size and weight could use the design (geometry, bolt engagement configuration, etc.) as a starting point.

1.4.3.3 Altitude-Direction Torque Coupling

As mentioned in Section 2.4.1.3, the altitude-direction torque coupling is used to transmit torque from the RM-5 motor to the telescope arm (the top-portion of the mount structure that holds the telescope). In the months leading up to the flight, this coupling was not performing as needed. When it was first integrated, it was slipping on the two shafts that it was coupling, introducing significant error for the pointing system. Since the maximum torque it was experiencing was not passed (as proven in Section 2.4.1.3), the issue may have been with the contact between the coupling and the shafts. It's possible that the surface finish was too fine for the coupling to grip, causing slip between the parts. This was simply speculation, however, and, even after investigation, the actual problem was not found.

To resolve this, though, a small hole was drilled through the coupling and through the shaft for the insertion of a pin. This pin would take the torque loads of the motor, transmit it to the coupling, which would, in-turn, transmit it to the following shaft (the telescope arm), completing the altitude movement of the telescope. This pin worked very well in-lab and during the integration and testing performed in Timmins in the weeks leading up to the launch. However, this modification was never analyzed and validated as the original configuration was. After the flight, it was found that the pin had failed. It is not known exactly when the failure occurred since there was no telescope movement during the flight. It can be speculated, however, that the pin failed upon landing since the maximum loads experienced before landing were relatively small and it had already survived comparable loads during transportation and integration. Therefore, it's difficult to conclude whether the pin would have functioned during flight as it did in the lab and during testing, but it's evident that it was not capable of surviving the acceleration loads of the flight.

1.4.3.4 Mechanical Vibrations Impact on the Pointing System

Although the design was demonstrated to be structurally strong, the top-portion of the mount presented some problems from a vibrational standpoint. During the gondola vibration tests, the pointing system was not able to stabilize on a point because of the constant mechanical movements caused by mechanical vibrations. It was speculated that the top-portion of the structure had a natural frequency that was close to the frequency at which the gondola vibrated due to small movements, which occur often.

After some rough calculations performed by CNES, it was found that the natural frequency of the actual structure of the telescope arm was around 16.2 Hz. According to CNES, this was sufficiently high to not be the cause of the natural frequency being close to the operational frequency of the gondola. After more deliberation, there seemed to be two major issues with the design, both that could have been contributing to the vibration problem: the constant-force springs used to balance the top-portion of the mount, and the fact that there was free movement for the entire top-portion of the mount due to play in the motors.

Since the constant-force springs connect the top-portion of the mount to the base, the natural frequency of the telescope arms alone does not provide enough information because it is part of a larger vibrational system. These springs may have introduced a new natural frequency the system or lowered the natural frequency of the original structure closer to the operational frequency of the gondola.

The telescope (and the entire top-portion of the structure) can be moved up and down in the altitude direction by hand if desired. This free movement is a problem because the telescope is not locked or fixed in a specific position when static; it can vibrate up and down and cause jitter for the pointing system.

These problems were discovered too late to find a mechanical solution, but the situation was improved with adjustments made to the pointing system's algorithm. In the end, these issues did not affect the mission because there was no star-tracking performed.

1.5 Recommendations for Improvement

Using what was discussed in Section 2.4.3, there are some parts of the design that can immediately be targeted as an area to improve, namely: the altitude-direction torque coupling and the mechanical vibrations that impacted the pointing system performance. These two will be discussed in the following subsections.

1.5.1 Altitude-direction Torque Coupling

As discussed in Section 2.4.3.3, this coupling presented a major issue for the pointing system and the solution implemented did not mitigate the problem entirely; in fact, it failed upon landing. The simplest solution would be replacing the coupling with a more suitable one that can tolerate higher torque loads and grips the shaft in a more reliable manner, such as a pin and bush configuration. This would remove the bottleneck for the torque, or at least increase the limit, that can be transmitted to the telescope arms from the motor and remove the issue of slip entirely. The second possibility is rethinking the design and removing the coupling altogether. Instead of having a coupling that connects the telescope arm to the motor, interface the two directly. The main issue here is figuring out the assembly procedure, which was the main reason for having a coupling in the first place. A potential work-around is designing the standing structure (the part that houses the bearings for the telescope arms) in a way that the top portion can be removed, allowing the telescope arm to be lowered into the standing structure with the bearing already integrated. The telescope arm's interface end could then be bolted onto the motor and the top of the standing structure re-attached, completing the assembly procedure. With this design, it would be important to ensure that the shaft that leads to the motor can withstand the torque loads. The current diameter of the shafts would, likely, suffice, but it's worth analyzing further.

1.5.2 Mechanical Vibrations Impact on the Pointing System

As discussed in Section 2.4.3.4, the mechanical vibrations also critically effected the pointing system during integration testing. The main source of the problem, here, was the constant-force springs that connected the top-portion of the mount to the bottom-portion, effectively changing the vibration modes of the top-portion to values other than what was found at the time by CNES. This dynamic resulting from the springs were not taken into consideration. They provide constant force in one direction, regardless of the distance they are pulled, resulting in differing spring constants for the lowering and elevating of the telescope. Also, the pointing system requires constant stable movement with as little jitter as possible. Springs will only provide stability when the system is stopped and is given a chance to go to equilibrium. In an application where the system is constantly moving, such as star-tracking, the system will never be given a chance to go to equilibrium. In this case, the springs must be removed from the design and a move back towards the original design of counterweights would be advised. Counterweights will keep the movements stable to begin with and, if an adjustable feature is also implemented, the position of the counterweight can be modified during the testing phase and locked for the flight. The main issues with this are the additional weight and potential mechanical interference with the optics box. The most feasible way to reintroduce the counterweights to the design would be to fix them onto the telescope arms, with half of the counterweight on each side. The issue was never foreseen because of a lack of knowledge in the behavior and stabilization of dynamic systems. The issue may have been discovered, however, if more extensive on-sky pointing tests had been conducted before the launch. The inability to maintain the pointing precision as a result of mechanical vibration may have been observed a lot earlier and mitigation strategies (such as pointing algorithm changes) could have been employed.

Chapter 2: Thermal Management

2.1 Scope of Work (SOW)

In order to dissipate the heat generated by the various EMCCD camera components, a passive-cooling thermal system was required for HiCIBaS. The solution developed was a custom thermal strap solution that will be discussed in further detail in Section 2.3.1. As mentioned in the Objectives of the Project, this thermal solution is supporting Objectives 4 and 5 of the mission's objectives.

More specifically, the thermal straps must:

1. Dissipate the heat generated by specific EMCCD camera components, as defined by Nüvü Cameras (the supplier of the cameras).
2. Keep the temperature of critical surfaces below their limits, as defined by Nüvü Cameras.

This chapter will detail the work done for the custom thermal straps and aim to demonstrate conformance to the scope of work defined above. Specifically, the requirements will be defined, followed by a discussion of the final design, details of the preliminary studies, an evaluation of the design with the approaches taken and the validation criteria, the mission performance of the system, and, finally, recommendations for further improvement.

2.2 System Requirements

Table 9: Thermal system requirements

Requirement #	Requirement	Origin
1	The maximum temperature of the detector surfaces (for the 128 and 512 cameras) must remain below 30°C for the duration of the flight	Nüvü Cameras
2	The maximum temperature of the controller surfaces (for the 128 camera) must remain below 40°C for the duration of the flight	Nüvü Cameras
3	The maximum temperature of the space controller surface (for the 512 camera) must remain below 20°C for the duration of the flight	Nüvü Cameras
4	The weight of the thermal system must be less than or equal to the weight budgeted for it (4.2 kg)	CNES HiCIBaS

In order to avoid redundancy, the surfaces mentioned in Table 9 are only displayed in Figures 34, 36, 38, 40, and 42 in the breakdown of the design.

Contrasting to the mount structure, the thermal system has very few requirements. In fact, they can be summarized in two categories: maintaining the maximum temperature of specific surfaces below specific temperatures and respecting the weight budget for the thermal system. It is still important, however, to understand the motivation for each requirement; here's a brief discussion for the origin of each of them:

- **Requirement #1:** The detector is the component in the camera that is also known as the CCD (charge-coupled device), it is responsible for light detection as a means for imaging. The performance of these

CCDs is directly linked to their operational temperatures and, so, they have integrated thermoelectric coolers that maintain their temperatures down to -85°C where they perform much better. However, in doing so, heat is extracted and moved to a different location in the system. This location is the surface that has the temperature limit defined in Requirement #1 and the value of the limit was determined by Nüvü Cameras. Therefore, this requirement is both operational and performance-related.

- **Requirement #2:** The controller is the electronics of the camera, it holds all the electronic components necessary for the camera to perform its functions. These components, however, generate a lot of heat. Nüvü Cameras has designed these controllers to dissipate heat outwards to two opposite sides of the electronic boards with two specific surfaces that are meant to be interfaced for heat dissipation. Again, the value of the temperature limit for this surface is defined in Requirement #2 and was determined by Nüvü Cameras. The controller's temperature does not have an impact on the performance, so this requirement is strictly operational.

- **Requirement #3:** The space controller has the same purpose as the regular controllers of the cameras. However, the space controller was designed specifically for space applications and, therefore, has a different geometry and, therefore, a different temperature limit. The electronics are integrated within a box (as shown in Section 3.3.2) and, therefore, it isn't as easy to interface for thermal dissipation. By design, heat is dissipated to the bottom of the box and, since the interface is not as direct, the value of the temperature limit for this surface is lower than the regular controllers, as defined in Requirement #3 and as determined by Nüvü Cameras. As with the regular controller, there is no impact on performance, so this requirement is operational.

- **Requirement #4:** The weight budget of the thermal system was estimated to be 4.2 kg and it contributes to the overall weight limit (100 kg) for the entire back floor imposed by CNES.

2.3 System Design

2.3.1 Design Breakdown and Driving Factors

With the minimal number of requirements for the thermal system, the driving factors of the design were less imposing on the design itself, but more imposing on the type of solution chosen. Instead of satisfying requirements imposed by other subsystems and external bodies, the design was driven by a "cost-to-benefit" type of approach. The primary goal was to find a solution that would:

1. Provide heat dissipation, as needed to satisfy Requirements 1-3.
2. Be reliable and bear minimal risk.
3. Be flexible in design, to anticipate potential changes in the optical system.
4. Use minimal space and minimal weight (due to space and weight constraints).
5. Use minimal monetary resources.

Another driving factor is the flight conditions, governed by the environment. As it pertains to this, there are two major areas of concern: low ambient temperatures and the lack of air (and, therefore, convection) in the stratosphere. This being the case, and for reasons discussed later in this section, it was determined that a passive solution that involved conductive heat transfer would be best suited for this application.

The solution chosen was a custom thermal strap solution made of copper shim stock and thermal epoxy (datasheets: Appendix 5). Multiple layers of copper shim stock (of thickness 0.8 mm) would be cut into the desired shape of a strap, they would be bent using a mold, glued together using thermal epoxy (of final thickness of 0.5 mm), clamped against the mold and left to solidify; this procedure is demonstrated in Figure 29 and an example of the final product is displayed in Figure 30. This solution was effective because it would be designed to provide the necessary heat dissipation, presented minimal risk because it would be a passive solution with zero reliability in other systems, it was flexible in design since it would be developed internally, it would only weigh as much as the material itself, and it used raw materials so it was low in cost.

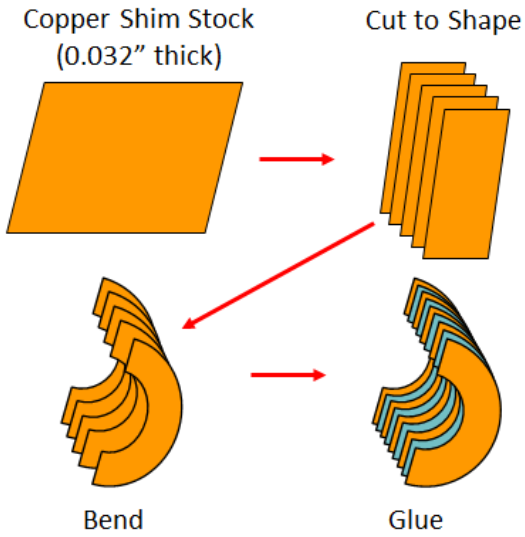

Figure 29: Fabrication and assembly procedure of the custom thermal strap solution

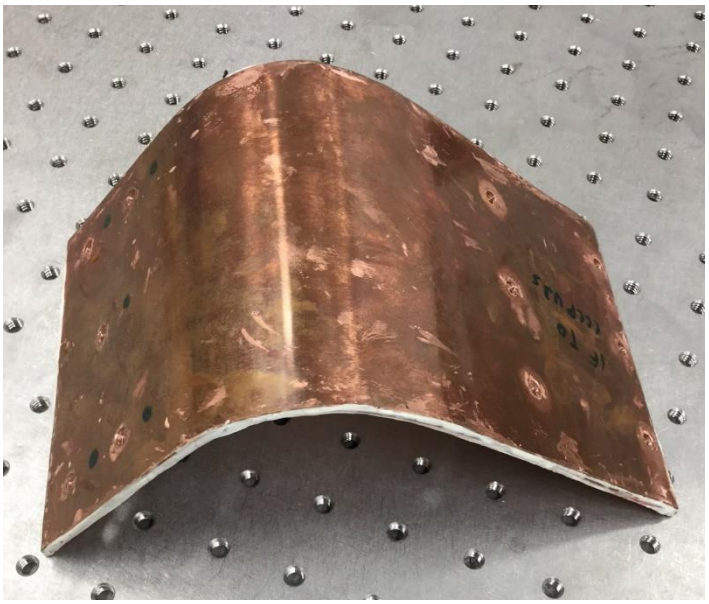

Figure 30: Custom thermal strap post-fabrication and assembly

The motivation behind the custom thermal strap solution came from the deliberation of 3 other solutions: liquid-cooling, two-phase heat pipes, and passive thermal straps. To provide some context, the following three paragraphs will provide some insight into the three solutions and why they were ruled out for the project.

Liquid-cooling solutions typically work by using a working fluid to transport heat through flexible piping from the heat source to the heat sink (Thermal Space, 2016). The liquid is cooled by transferring the heat to the sink and returns to the source to transport more heat. This design is extremely practical because of its flexibility and ease of assembly, but there were too many problems with the solution. It presented the most risk because it was an active solution that required power and a lot of testing to ensure it performed as needed. Also, a lot of research and design iterations needed to be done for this. With the time constraints and the desire to minimize risks, this solution was deemed too risky to attempt.

Two-phase heat pipes use the phenomenon of phase transition and capillary action to transport heat. As the liquid in the pipe absorbs heat from the source, some of the liquid will transition into its gaseous, or vapor, state and be pushed to the opposite end of the pipe because of the capillary movement of the rest of the liquid (Advanced Cooling Technologies, 2018). This design was considered for a long period of time because it presented the same benefits as the liquid-cooling solution with almost no risks. Two major problems were encountered, however. The custom commercial solution product that was flexible in design was far too costly. Contrastingly, the mass-produced commercial product that was cheap was too rigid in design. The latter was considered because interface pieces could be designed to add some flexibility to the routing of the heat pipes. The problem with this was that the behavior of the heat pipes couldn't be easily simulated and, therefore, their behavior could not be anticipated. Due to the risk factor and time constraints, this solution was deemed too risky to attempt as well.

The commercial thermal strap is the simplest of all the solutions. It entails using the principle of thermal conductivity to transfer heat from the hot-side of a strap (the heat source) to the cold-side of a strap (the heat sink). The material is typically an alloy of copper that is very close to its pure form (more than 99% pure copper), the only constituents being added to increase the structural integrity of the material (Technology Applications, Inc., 2018). Typically, the strap is two blocks of this copper alloy with a braid of copper wiring between them. In other words, the thermal performance of the strap is maximized while maintaining structural integrity and minimizing weight. This design presented the most benefits: virtually no risk if well-designed, flexible in design, and low-weight. The major issue, and, ultimately, the deciding factor in why it was not chosen, was the cost. This solution was the closest to being used and, because of the benefits discussed, it was the origin of the idea of using a custom thermal strap solution for the project, a solution that would have the same benefits as the commercial product but be much less costly.

It's important to note, though, that the thermal straps are only a means to *transport* heat from the heat source to the heat sink. The heat sink is the destination of the heat generated by the heat source. Typically, the heat sink is a component with a lot of surface area. In order to remove heat from a system entirely, it must be transferred to the surrounding medium (air) by thermal convection or radiation, mechanisms that are heavily dependent on surface area. For the case of this project, an appropriate heat sink was found that was already part of the design: the optical bench's cover, as displayed in Figure 31. The optical bench's cover is a component that has a simple, but essential, purpose: shield the optical bench's components (the optical system) from the harsh environmental conditions of the stratosphere and from stray light. The thermal system can take advantage

of this by repurposing the cover as a heat sink and a radiator by creating a thermal link (i.e. the thermal straps) between the heat-generating components and the cover. This effectively removes the need for a separate radiator that would complicate the overall design and add weight to the payload.

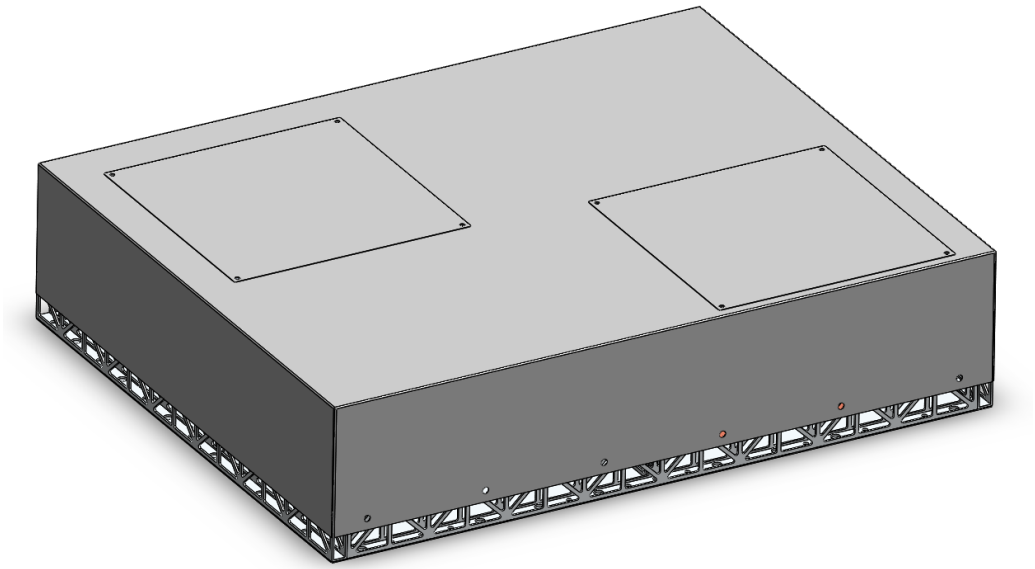

Figure 31: Full CAD model displaying the optical bench's cover

It is equally important to note that polyurethane foam (datasheet: Appendix 5) was added to the interior of the cover in order to introduce a layer of thermal resistance and promote gradual temperature change for the optics bench components. This is displayed in Figure 32; there are some sections cut out to make space for the straps to interface with the bench.

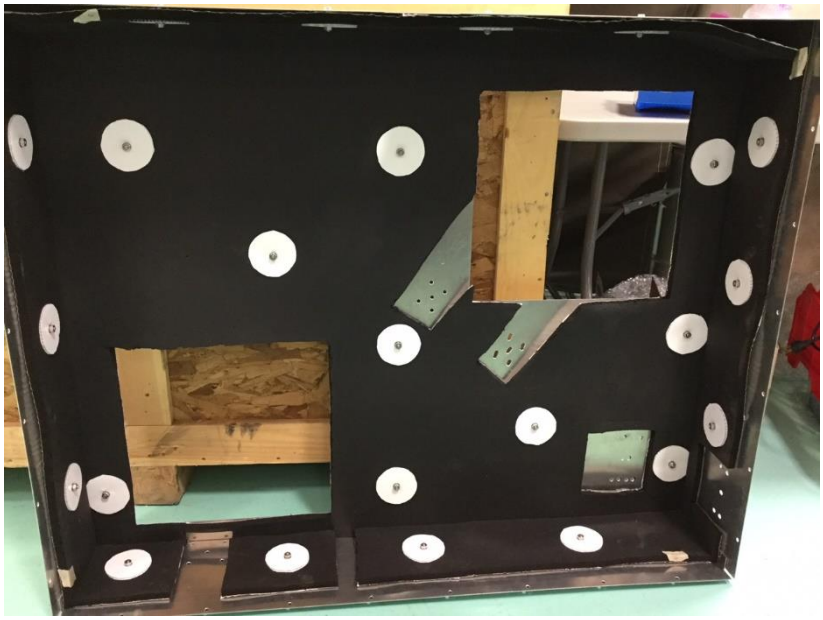

Figure 32: Polyurethane foam integrated on the interior of the cover

The following section (Section 3.3.2) will demonstrate where and how the straps interface with the cover.

2.3.2 Component-Level Design Breakdown

Since every component that generates heat is different in geometry and location, a different strap design was developed for each; they differ in length, width and the way in which they bend to interface with the heat sink (so, the overall shape). Therefore, this section will provide a brief discussion for the design of the thermal strap for each heat-generating component, the motivation behind it, and the specific challenges for each, if any.

It is worth noting here that the heat-generating components are all constituents of Nüvü Cameras' EMCCD cameras (Nüvü Cameras, 2018) that were supplied for this project (the purpose of each component has been defined in Section 3.2 in the discussions of the requirements). Most of these components are commercial products that were modified to a stripped-down configuration for this mission (apart from the Space Controller). Basically, the modifications involved removing parts or modifying them to expose the surfaces to be interfaced (hereafter referred to as "critical" surfaces) for thermal dissipation. Thermal interface material (datasheet: Appendix 5) was also used at all interfaces to increase thermal contact.

To provide some context before discussion each component of the thermal system, refer to Figure 33 for a look at where each of these components are located on the optics bench.

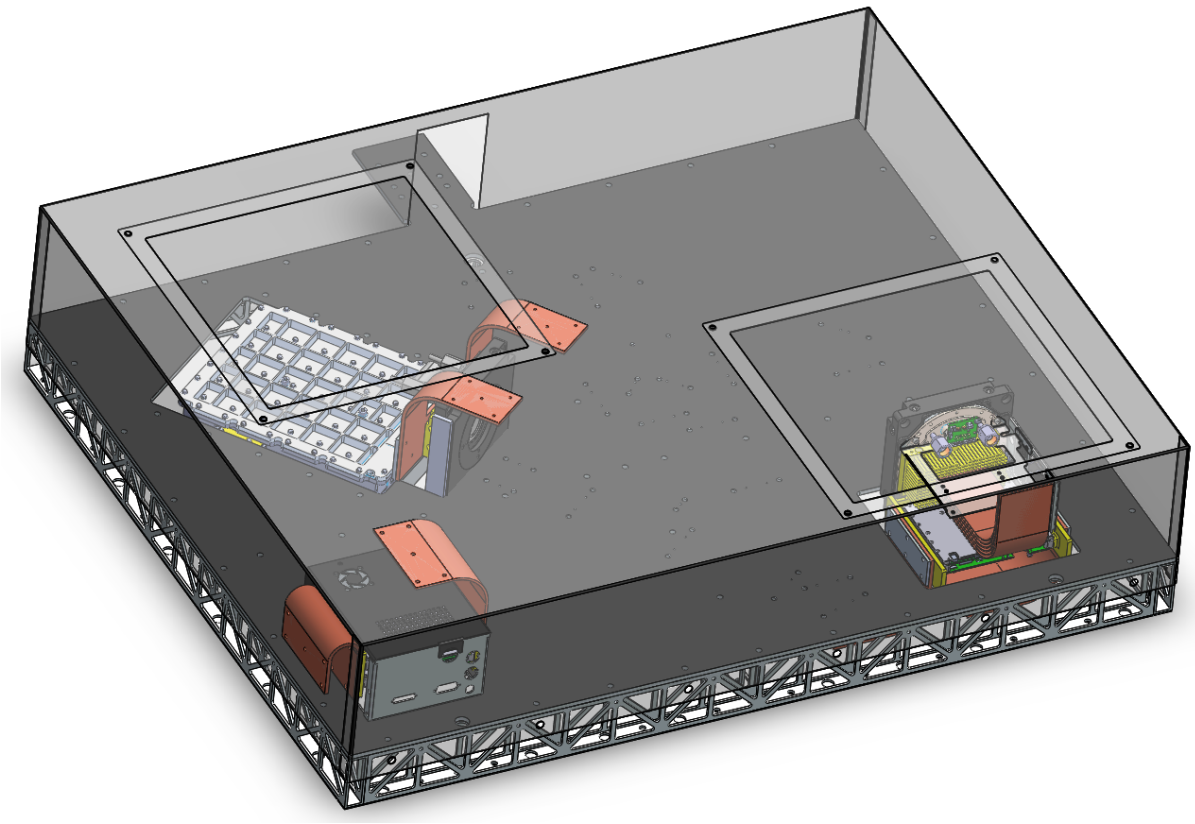

Figure 33: Full assembly configuration of the optics bench

2.3.2.1 HNü 512 Detector

The HNü 512 detector had one of the most accessible thermal interface surfaces. It is a component made of brass with a flat interface surface and four threaded holes for 8-32 screws, as seen in Figure 34. The only challenge with this component was the routing of the strap. As you'll note from Figure 34, the interface surface has components above and below it, putting constraints on the strap design. After trying a few CAD configurations, it was determined that the shortest length (the most performant) and the easiest configuration for assembly was simply bypassing the components that are above the interface surface from the left and the right sides, making a 90° turn to reach the cover, and making a 90° bend to interface with the cover, as seen in Figure 35.

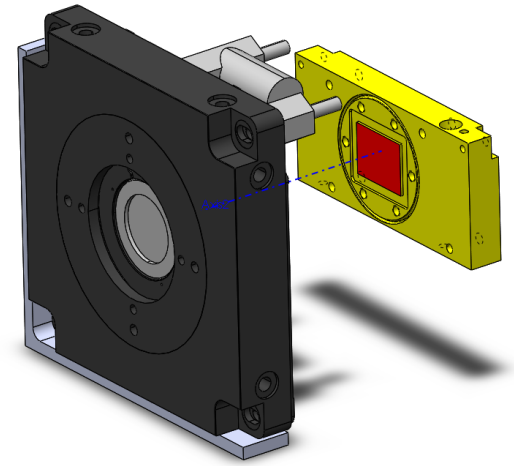

Figure 34: Critical surface for the HNü 512 Detector

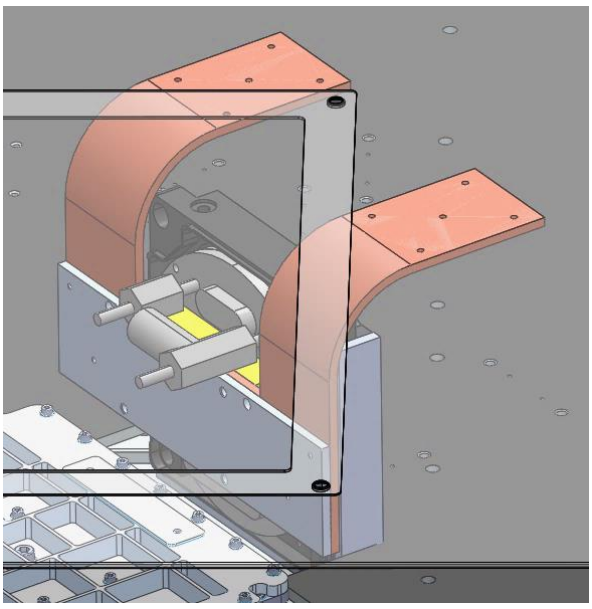

Figure 35: Full assembly configuration of the HNü 512 Detector

2.3.2.2 Space Controller

The Space Controller had the most accessible thermal interface surfaces of all the components. Since the electronics are located inside the box, as discussed in Section 3.2, the bottom of the box was the thermal interface surface, as displayed in Figure 36. Since it needed to be elevated to be plugged into the HNü 512 detector, the most convenient and simplest solution was to design a platform (made of 6061-T6 aluminum) that was optimized for thermal performance and weight instead of designing a platform and an additional strap, as seen in Figure 37. Although its thermal conductivity is low compared to the copper of the thermal straps (170 W/m·K versus 391 W/m·K), the Space Controller dissipates heat over a much larger area, so the low thermal conductivity of the platform has less of an impact on the heat dissipation because the heat flux is lower.

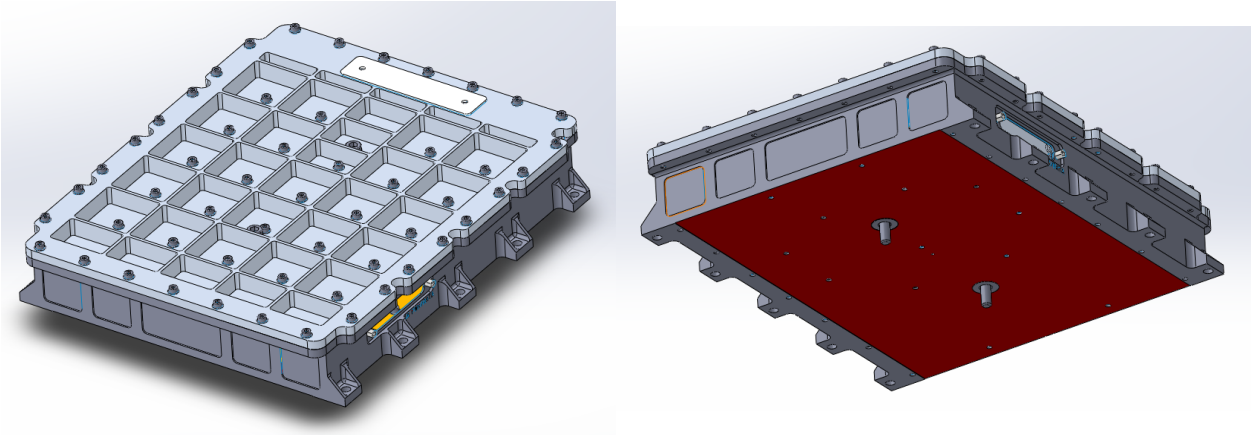

Figure 36: Critical surface for the Space Controller

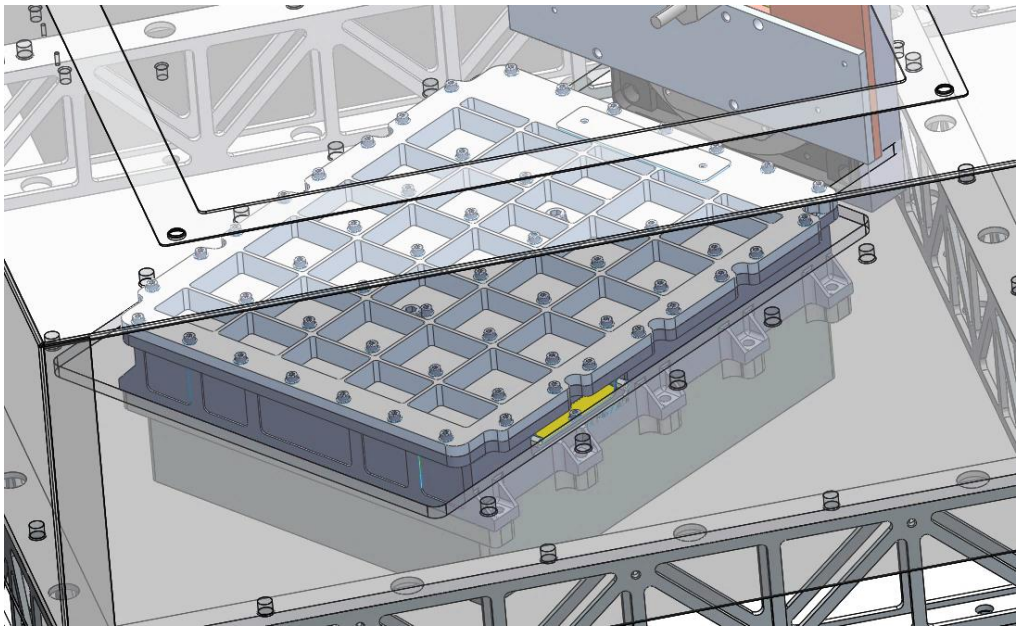

Figure 37: Full assembly configuration of the Space Controller

2.3.2.3 HNü 512 Regulator

The HNü 512's voltage regulator is comprised of two electronic boards that are stacked one on top of the other, with each electronic board having two thermal interface surfaces on opposite sides. It was evident two straps would be needed – one for each side. However, interfacing the strap with the electronic boards directly cause a lot of mechanical stress on the controllers. Instead, an intermediary piece was designed to interface with both electronic boards at the same time and with one on each side. This way, the intermediary piece could take the loads experienced from the strap, provide an excellent interface surface, and absorb the heat from both electronic boards at the same time, the assembly configuration (without the straps integrated) is shown in Figure 38. The shortest length and convenient design for the straps differed on the two sides. The side next to the cover had an upside-down U-shaped strap that interfaced with the side of the cover and the opposite side had an upside-down L-shaped strap that interfaced with the ceiling of the cover, as seen in Figure 39.

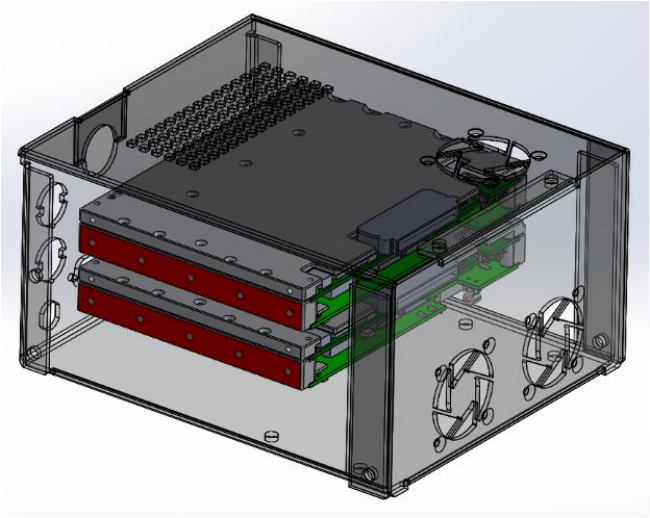

Figure 38: Critical surface for the HNü 512 Regulator

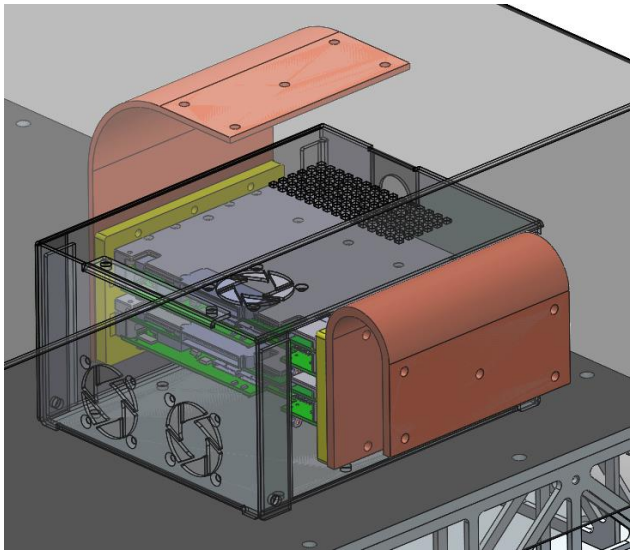

Figure 39: Full assembly configuration of the HNü 512 Regulator

2.3.2.4 HNü 128 Detector

The HNü 128 detector presented the most difficulty for the design of the strap. The detector has the same type of component as seen with the HNü 512 detector, but it has fins protruding from the surface, as displayed in Figure 40. This design is meant to be used with a fan for commercial purposes and couldn't be modified or removed. Besides making permanent modifications, or developing an entirely unique thermal solution, the only option was to wedge the copper shim stock between the fins and increase the thermal contact as much as possible using thermal paste, as seen in Figure 41. The end of the strap that interfaced with the cover was glued together and assembled as the other straps.

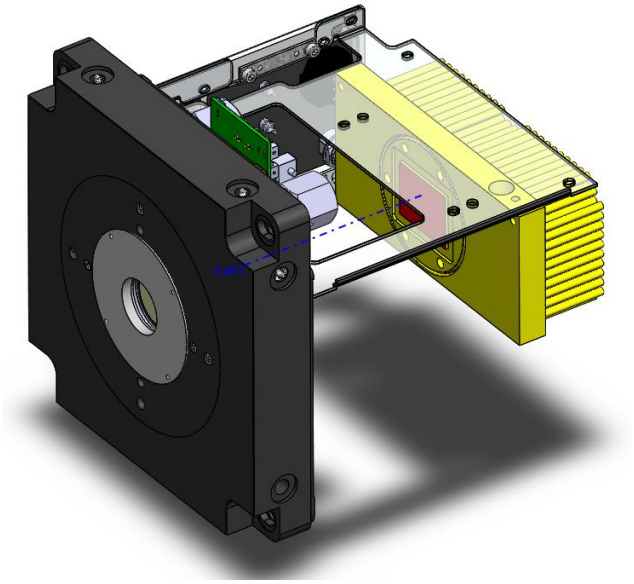

Figure 40: Critical surface for the HNü 128 Detector

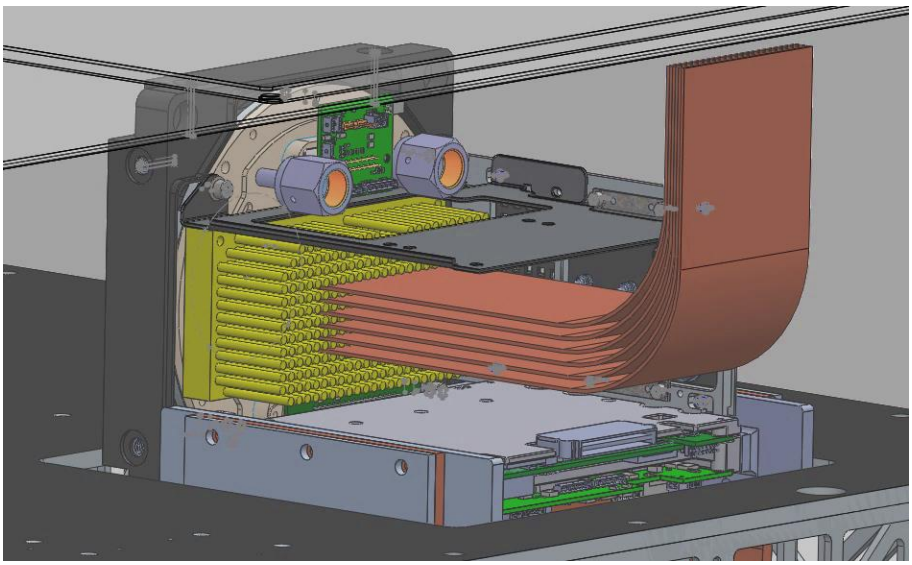

Figure 41: Full assembly configuration of the HNü 128 Detector

2.3.2.5 HNü 128 Controller

The HNü 128 controller is a simpler form of the HNü 512 regulator because it is simply one electronic board instead of two. However, because the housing of the camera was removed to expose the thermal interface surfaces, displayed in Figure 42, the controllers needed to be mounted to the housing surrounding the HNü 128 detector. A mounting piece was designed for each side of the controller to hold it in place and to interface with the straps. The strap design was simple, an L-shaped design for each side of the controller, as seen in Figure 43. For this component, however, the straps were routed to the floor *below* the optics bench. This floor was necessary to house some components, most importantly the electrical system and the wires for the entire payload. Again, we were able to give this component more purpose by using it as a heat sink, as was done with the cover.

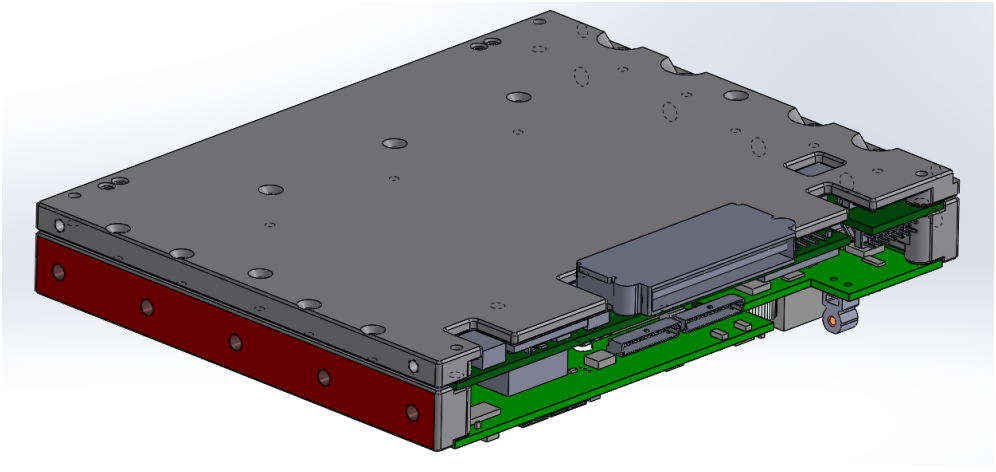

Figure 42: Critical surface for the HNü 128 Controller

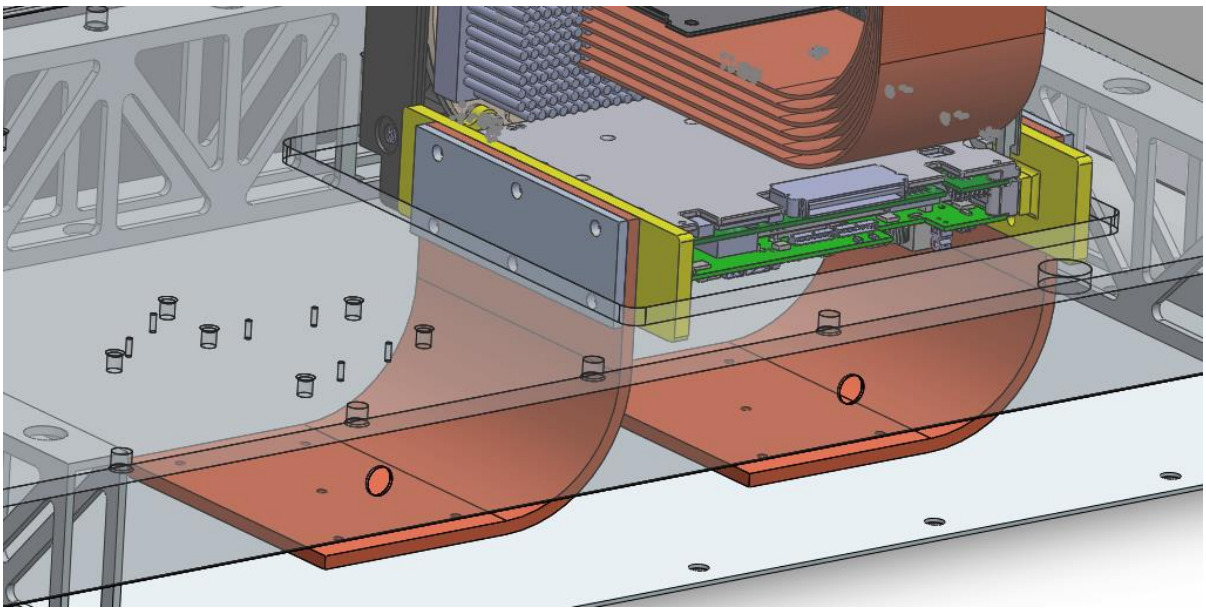

Figure 43: Full assembly configuration of the HNü 128 Controller

2.3.3 Feasibility Study

Since this solution has so few requirements and only consist of high-level requirements, low-level (performance) requirements needed to be created to ensure that the thermal straps could provide the heat dissipation necessary to satisfy those high-level requirements. To do this, a performance indicator needed to be established that could provide a validation criterion for each strap. Once the validation criteria are established, a feasibility study could be conducted to gauge if the proposed solution is able provide the heat dissipation necessary. This section discusses the performance indicator, establishes the validation criteria, and describes the feasibility study conducted to test the viability of the proposed solution.

2.3.3.1 Determining the Performance Indicator and Validation Criteria

Typically, the performance indicator for a thermal strap, a *transporter* of heat, would be its thermal resistance, a measure of how it resists heat transfer. Of course, for a thermal strap, it would be ideal to have as low of a thermal resistance as possible. However, this type of performance indicator is mostly used for comparing the performance of different strap lengths and geometries, not for establishing low-level system performance requirements. Instead, the temperature difference, ΔT, a variable needed to find the thermal resistance, was chosen as the performance indicator.

For a specific set of conditions of operation, the straps will achieve a specific temperature difference, ΔT, between the heat sink and the heat source. Some of the conditions of operation that effect this ΔT are: surrounding medium (air, water, etc.) physical properties, thermal interface surface area, strap material and thermal properties, heat sink and source thermal properties, and heat input into or generated by the system. This can be observed when modeling a thermal system using a thermal resistance network, which is an analytical technique that allows one to study the behavior of heat transfer through a system (Bergman, Lavine, Incropera, & Dewitt, 2011). The network is made up of resistances and capacitances that model the way a system's components resist a heat flow and absorb heat, respectively. In other words, it describes how heat moves through a system. An example of a thermal resistance network and the associated resistance and capacitance equations are displayed in Figure 44 for the HNü 128 controller.

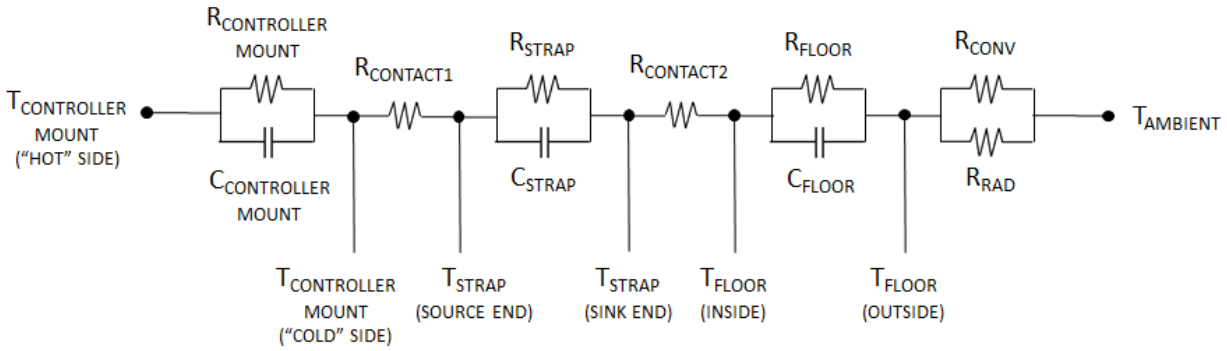

$$R_{cond} = \frac{T_{s1} - T_{s2}}{q_x} = \frac{L}{kA}; \quad = \frac{1}{h_r A} \qquad R_{conv} = \frac{T_s - T_\infty}{q} = \frac{1}{hA}; \qquad R_{cond} = \frac{T_s - T_{sur}}{q_{rad}}$$

$$R_{cont} = \frac{T_A - T_B}{q"_x}; \qquad C\frac{dT_q}{dt}; where\ C = \rho V c_p$$

Figure 44: Thermal resistance network and derived equations for the HNü 128 Controller

Using the thermal resistance network, it is possible to determine the maximum ΔT permissible in order to maintain the temperature of the heat source's surface below it's limit; of course, the optimal ΔT would be as small as possible, implying very little resistance. This can be accomplished by developing a numerical model of the network using the equations for the resistances and capacitances in Figure 44. A system of equations would be needed for each component (one equation for every node in the network), up to the two nodes of the strap (source-end and sink-end). These nodes are found at each surface throughout the thermal system. We can then impose the known dimensional and property values (surface area, convection coefficient, etc.) to find the resistances and capacitances, and the values for the ambient temperature ($T_{ambient}$). The only unknown values left will be the temperatures at each node. Using a numerical solver, the numerical model can then be iteratively solved to bring the system to a steady-state. In doing so, for those specific conditions, the maximum ΔT allowed for the strap to reliably dissipate the heat generated can be found. The system of equations derived for one of the numerical models (the HNü 128 controller) is shown in Appendix 6.

Using this iterative, analytical technique, the maximum ΔT allowed was found for each strap by finding the difference between the surface temperature of both ends of the strap. They vary because of differences in surface area interfaced, heat flux, geometry, and length. By obtaining the temperature difference throughout the entire system (source to sink), we can also compare how much ΔT is caused by the strap relative to the rest of the system. This simply provides more useful information about the performance of the straps. The results are shown in Table 10.

Table 10: Maximum ΔT values allowed for each strap component

Strap Component	Maximum ΔT Allowed (°C)	$\Delta T_{strap}/\Delta T_{system}$
HNü 512 Detector	16.2	96.7%
Space Controller	17.4	92.1%
HNü 512 Regulator	28.4	96.1%
HNü 128 Detector	20.3	98.9%
HNü 128 Controller	29.8	99.2%

2.3.3.2 Flight Simulations

After establishing the validation criteria, simulations must be performed to see if the designs proposed for each strap is viable. As previously mentioned, the ΔT depends on the specific conditions of the steady-state environment, so, for the simulation, the parameters used must reflect the high-altitude conditions we expect to experience (as closely as possible) to observe the true ΔT. The full parameter set, their respective values, and other simulation setup activities are outlined in Section 2.4.1, but, for convenience, the following is a summary of the values at peak altitude (Borden, 2017):

- Ambient temperature: -45°C
- Heat input: 50 W
- Convection coefficient: 0.05 $W/m^2 \cdot K$
- Radiation emissivity: 0.90

The ΔT derived from these simulations are conservative because the parameter values chosen for the simulation were chosen conservatively; the results are listed in Table 11.

Table 11: Actual ΔT values to be expected for each strap component

Strap Component	ΔT Simulated (°C)	Maximum ΔT Allowed (°C)	Safety Factor
HNü 512 Detector	13.18	16.21	1.23
Space Controller	11.32	17.44	1.54
HNü 512 Regulator	9.51	28.42	2.99
HNü 128 Detector	12.82	20.37	1.59
HNü 128 Controller	8.47	29.89	3.53

Evidently, all the ΔT values for each strap are below their maximum ΔT allowed, and all straps have a great safety factor, even after choosing conservative values for the simulation parameters. This is a good sign for the design and increases the confidence level in the viability of the custom strap solution, allowing for the next step in the development process: the full-system simulation.

2.3.3.3 Verification and Validation (V&V) of Results

Before the full-system simulation, however, it's important to show a couple of verification checks to ensure the reliability of our results in Section 3.3.3.2. The *first* type of verification was performed immediately within the simulation software (ANSYS) to check for inconsistencies and errors in the results. Generally, this issue is not prevalent in small-scale tests that tend to be consistent in shape, but the check was done for the sake of completion and good practice. However, the identical check was conducted, and conducted in more depth, for the full-system simulation performed in Section 3.4.2, where the model in question is more complex. So, to avoid

redundancy, I will simply note that the verification checks performed in Section 3.4.2.6 were also performed for this feasibility study in a nearly identical manner.

Unique to this feasibility study, however, is an in-lab test executed after the fabrication of the straps to compare the behavior of the simulation model to the physical model and verify (after-the-fact) the accuracy to which our simulation model mimics the physical model. The test could not be performed in flight conditions, so, instead, a simulation was performed using the lab's conditions. It's important to remember that the conditions themselves are not the most important factor for the setup of the simulation, this check is simply to see if the simulation model behaves accurately to the physical model for any given set of operating conditions, especially in the steady-state region, which is of prime interest. The test was executed with a thermocouple on the opposite end from the heat input location of the HNü 512 regulator strap, as displayed in Figure 45. This configuration gives us the best comparison because the heat would have to travel through the entire part, which results in a much more thorough test since the entire system is playing a role. The test was run for 4 hours to achieve a steady-state condition, using 10 W of heat input; the results are shown in Figure 46.

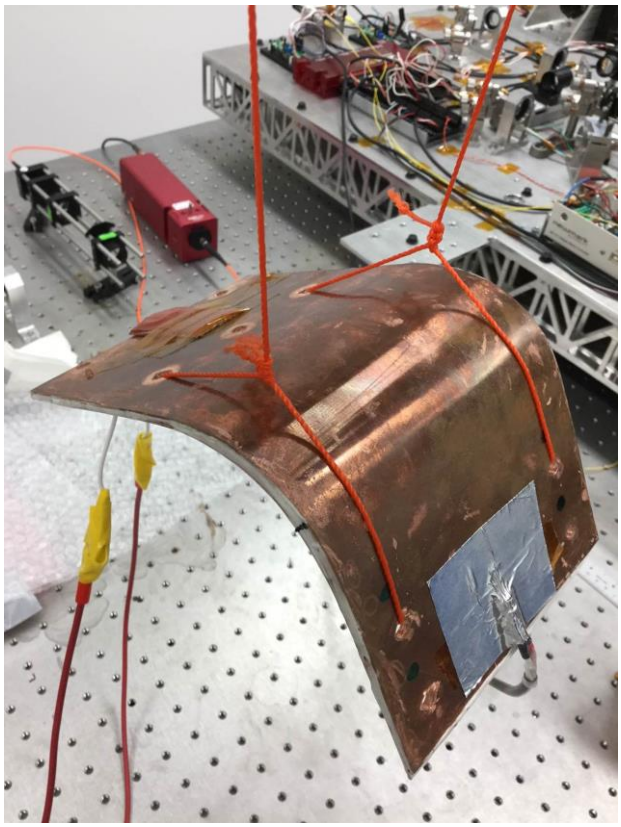

Figure 45: Lab test setup of the HNü 512 regulator strap

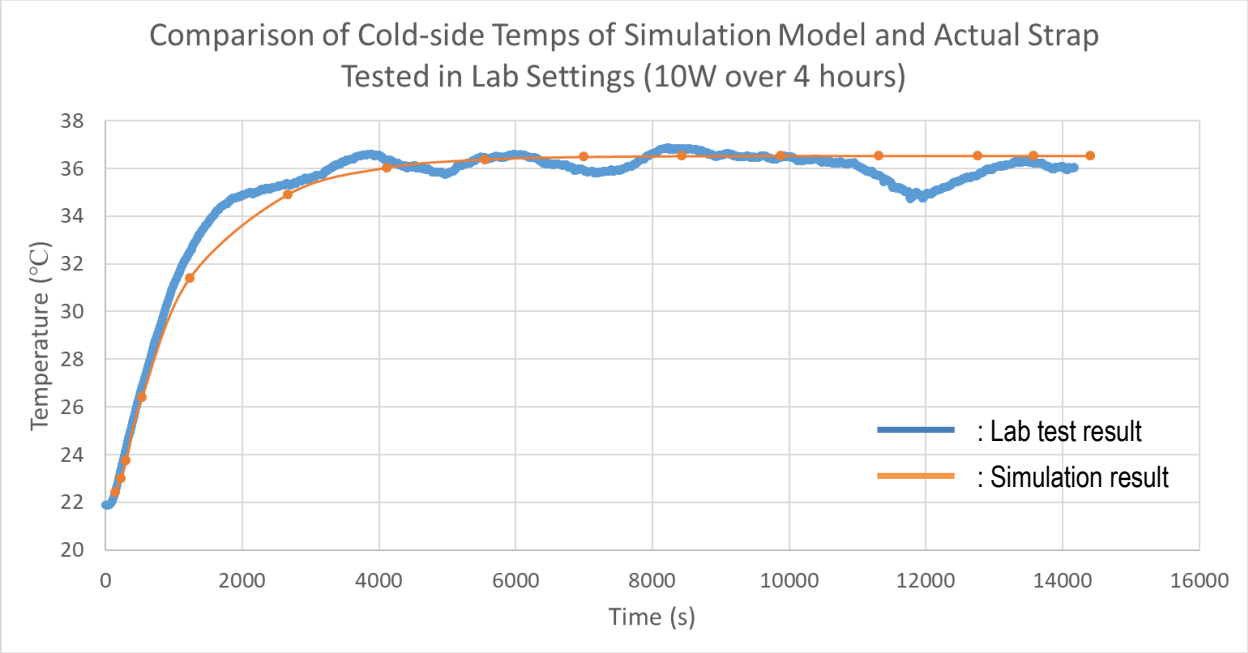

Figure 46: Comparison of the simulation results and the lab test results

There is a sudden dip that occurs close to 12 000 seconds mark in Figure 46, this is caused by the entering of personnel into the lab and test area, causing a change in the environment and rendering the system to leave the steady-state condition. Apart from this anomaly, though, there is an average steady-state temperature difference of ±0.8°C. With this, we can safely conclude that the simulation model behaves very closely to the physical model and we can state that this verification check is a success.

2.4 Evaluation of the Design

This section will demonstrate conformance to Requirements 1-3 pertaining to the surface temperature requirements of each component. All design models in this section were made in SolidWorks 2017 and imported into ANSYS 18.0 for thermal simulations.

2.4.1 Simulation Setup

The primary goal of this section is to build confidence in the setup of the simulations performed. More specifically, to build confidence in the simulation model's preparation and the parameters used. This section will outline the setup of the simulation by describing the general setup strategy, the input parameters, the parameter values, and the results expected.

To begin, the type of simulation chosen was the transient thermal simulation. The general strategy for the setup of the simulation was to remove as many parts as necessary to be able to run the simulation (limited by processing power and time) without compromising the accuracy of the results. The major issue is removing too many components and affecting the thermal inertia of the system so that it behaves differently from the physical model. In the end, the simulation model was comprised of only the essential parts: the components with the critical surfaces, the components directly in contact with those surfaces (the straps), and the heat sink

surfaces (cover, floors, and walls). The stripped-down configuration by component was displayed in Section 3.3.2, and the simulation model of the full assembly will be displayed in the following section, Section 3.4.2, to provide context for the subsequent results. It's important to note, as well, that the straps' properties were made to reflect the *effective* thermal properties of the copper and thermal epoxy used since the strap was modeled as a single entity (to simplify the model), but is, in fact, a stratified assembly.

The next step was to ensure that the *meshing* of the components was generated. Meshing is the practice of breaking up a component into small pieces, called *elements*, to be solved by a finite element analysis through the software's numerical solver. The meshing of components will directly impact the accuracy of the results. The overall goal is to generate a mesh that is fine enough to deliver accurate results, but coarse enough to minimize simulation time. For the heat sink components that were typically larger, the mesh sizes were left to the default sizes (up to 20 mm) determined by the software. Closer to the heat-generating components, though, the mesh size was lowered down to 5 mm. The straps and heat-generating components themselves had mesh element sizes of 0.1 to 5 mm, depending on the area; the closer to the critical path of the heat flow and the more complex the geometry, the finer the mesh. An example of the mesh size for the HNü 512 Regulator components, having a minimum element size of 0.1 mm, are displayed in Figure 47.

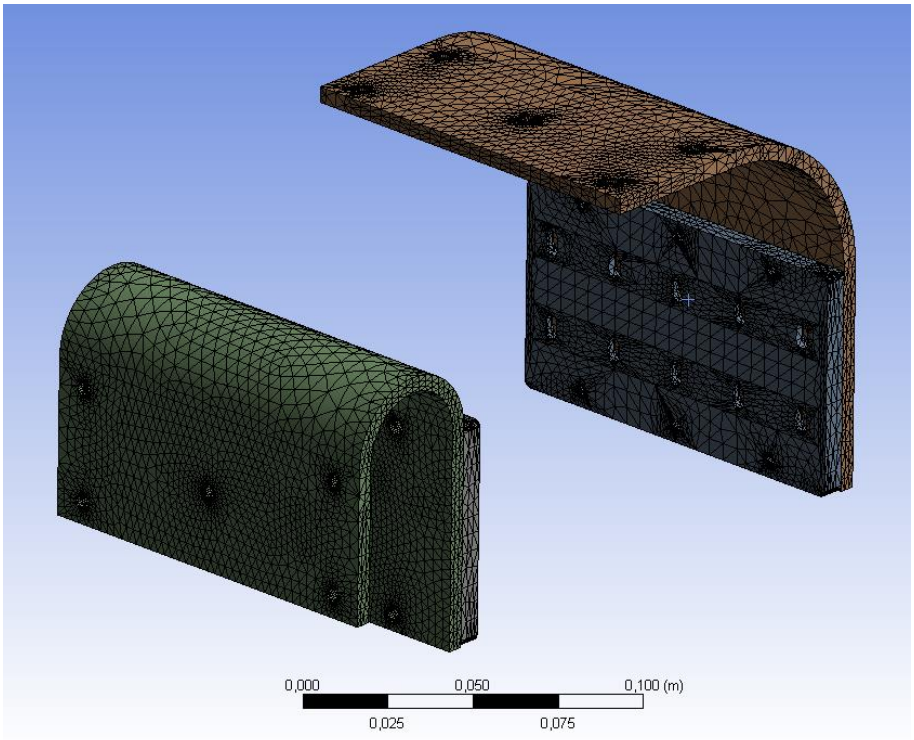

Figure 47: Modified meshing scheme for the HNü 512 Regulator components

With the simulation model established, the next step is to apply the loads and conditions of the simulation. In terms of loads, the input used were *heat flows*. Heat flows are measured in Watts and was used because the heat input situation was provided by Nüvü Cameras in terms of Watts for the critical surfaces (they are conservative estimates). However, some surfaces were smaller than others, so the *heat flux*, the heat flow per area, varied from component to component. In other words, even though the same amount of overall heat was

being generated, some surfaces were receiving larger “concentrations” of heat than others. Table 12 provides a breakdown of the heat flows used.

Table 12: Breakdown of heat flow inputs for the flight simulation

Component	Heat Flow per surface (W)	Total Heat Flow (W)	Heat Flux (W/mm²) per surface
HNü 512 Detector	50	50	0.06294
Space Controller	50	50	0.0008776
HNü 512 Regulator	25	100	0.01835
HNü 128 Detector	50	50	0.06294
HNü 128 Controller	25	50	0.01835

The parameters of the simulation were more complicated because some of them were dynamic during the flight, hence the need for a *transient* thermal simulation. The radiation coefficient was fixed at a conservative value of 0.95 because a few coats of white paint would be applied to the heat sink and, typically, they provide coefficients of 0.988-0.992. However, the convection coefficient changes with altitude due to the varying properties of air, environmental conditions, and system geometry. Similarly, the ambient temperature data can also be unreliable due to day-to-day meteorology. Analyzing these to develop a model would be far too complicated and, so, existing datasets were sought to be used. Unfortunately, high-altitude convection coefficient and temperature data is extremely scarce. Only two publications were found with datasets that could be used and, so, the more conservative, detailed, and well-explained dataset was chosen (Borden, 2017). The generated curves for the convection coefficient and ambient temperature that were used for the simulation is displayed in Figures 48 and 49. Note that the convection coefficient after 8000 seconds in Figure 48 is at 0.05 W/m·K, not zero.

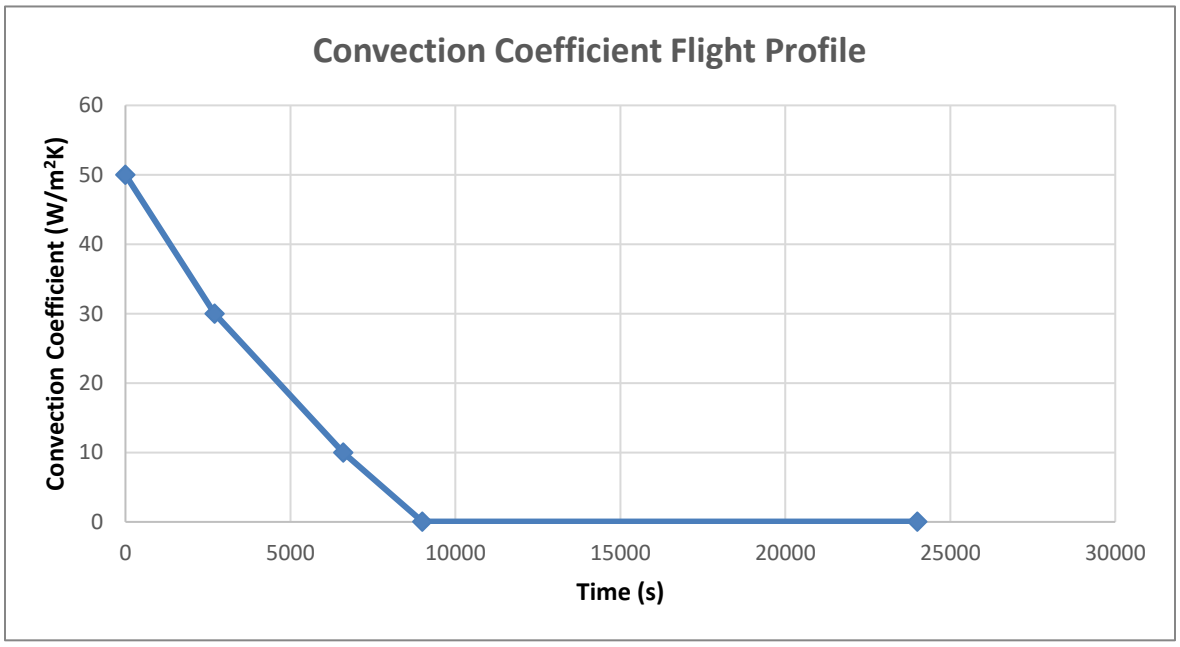

Figure 48: Convection coefficient curve used for the flight simulation

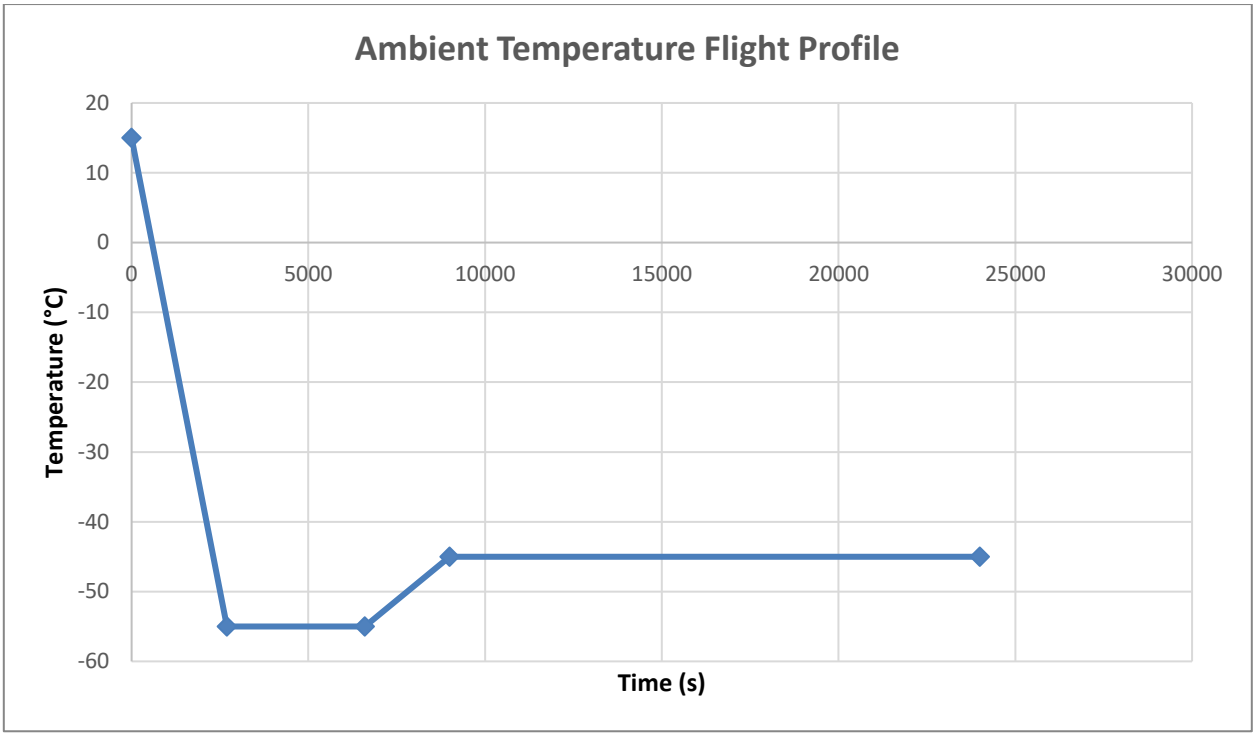

Figure 49: Ambient temperature curve used for the flight simulation

The last parameter to be defined was simulation time. The ascent time of the flight was determined to be 2.75 hours using information provided by CNES. The total time that was guaranteed for the cruise phase of the flight was about 4 hours. This brought the full simulation time to 6.5 hours. This information was critical in determining the altitude of the payload for a given time. An altitude-time curve was developed, as seen in Figure 50, that helped generate the convection coefficient and ambient temperatures curves in Figures 48 and 49.

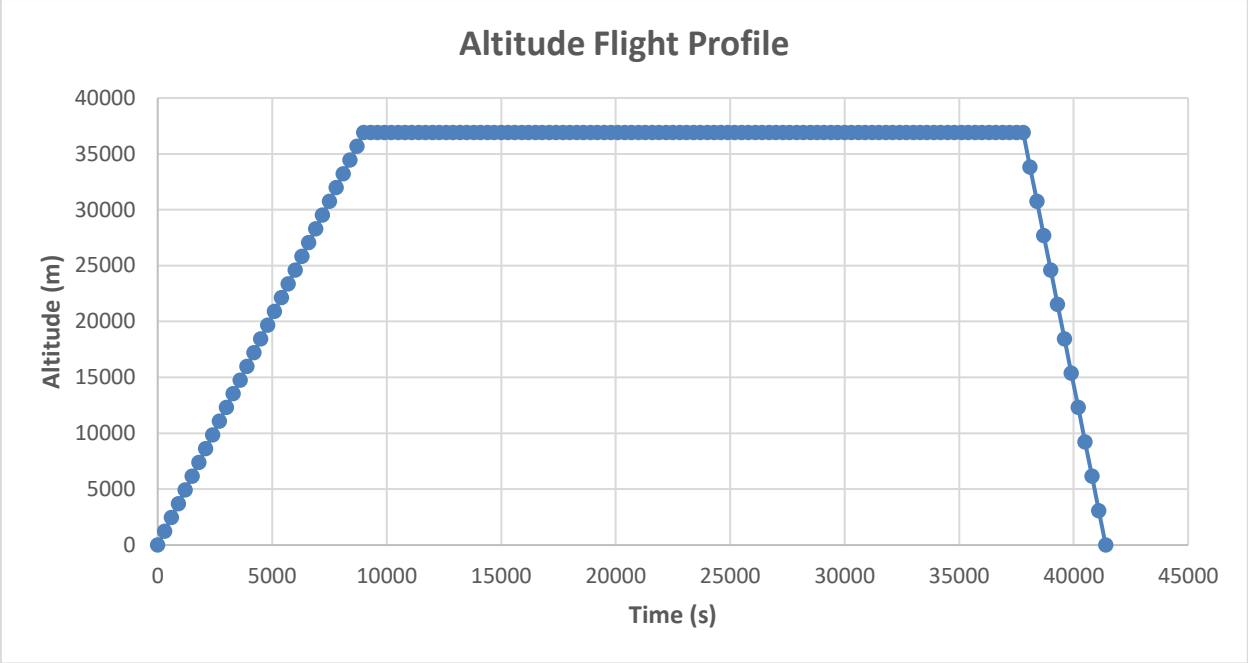

Figure 50: Altitude profile of the mission used for the flight simulation

For the last part of the setup, it's necessary to define the results desired and set a parameter to increase the accuracy of these results. In the case of the flight simulation, the most important result is the temperature of the critical surfaces defined in Section 3.3.2. Other desired results are the temperatures at both ends of the thermal strap to assess their performance and to see if the ΔT expected is achieved. The simulation was then set to perform two (2) refinement loops and have a refinement depth of two (2) as well, allowing the system to iterate the results and converge on a solution more precisely.

2.4.2 Simulation Analysis

This section will highlight the results of the flight simulation executed for the thermal system. The performance of the overall system will be measured by looking at the maximum temperature expected for each component's critical surface through simulation and comparing it to the maximum allowed temperatures defined in Requirements 1-3. Figure 51 displays the simulation model with the cover hidden to give an idea of the components that were removed for the simulation model and Table 13 holds the results of the simulation at the component-level.

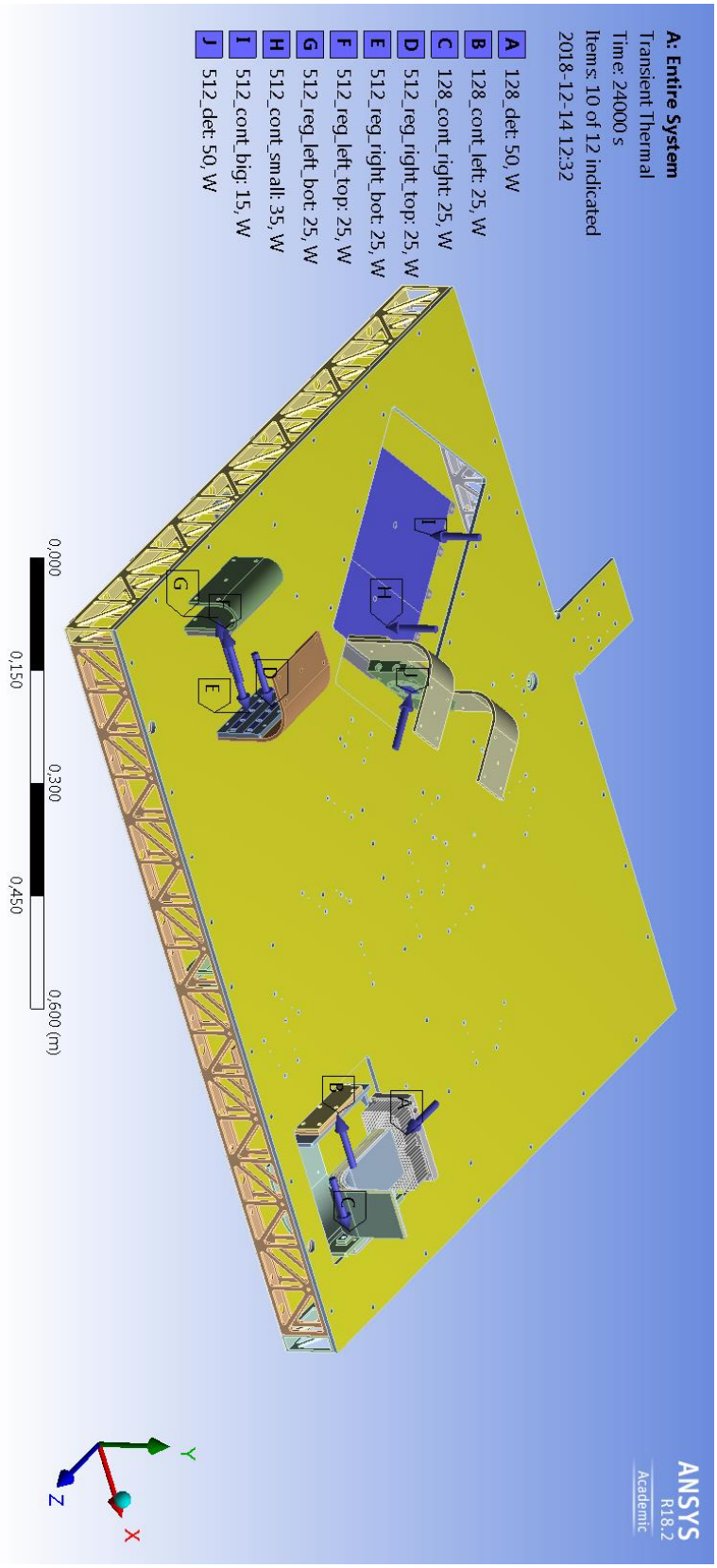

Figure 51: Simulation model of the thermal system's main components (and cover hidden)

Table 13: Maximum temperatures expected through simulation for critical surfaces

Strap Component	Maximum Simulated Critical Surface Temperature (°C)	Critical Surface Temperature Allowed (°C)
HNü 512 Detector	18.66	30
Space Controller	20.05	20
HNü 512 Regulator	24.34	40
HNü 128 Detector	36.01	30
HNü 128 Controller	21.09	40

Using Table 13 for side-by-side comparisons for each component, we can see that the design maintains most of the critical surface temperatures below their limits, thus satisfying Requirements 1-3 from a *design* standpoint for most of the components. Of course, the configuration used for the simulation is much simpler than the full-assembly (physical) model, but, as outlined in Section 3.4.1, many of the parameters were conservatively estimated and there is still a large margin of error available for most components. It should also be made aware that these maximum temperatures expected occur at the very end of the flight. The only component that significantly passes the allowed temperature limit is the HNü 128 detector, by a magnitude of about 6°C. This was expected because of the difficulties with establishing a design that could interface well with the component (as discussed in Section 3.4.3.1.2). A simple contingency procedure was set for the scenario where any component approached their temperature limit: turn the component off, allow it cool down passively for 5 minutes, turn the component back on, and resume operations.

Note that the temperature curves for the critical surfaces from the simulation were omitted from this section to put emphasis on the numerical results and avoid redundancy. The curves are nearly identical in shape to the pre-flight curves found in Section 3.4.3.1 where they are compared to the post-flight simulations and measured data, except that they are offset by the ΔT values for each component since that data is measured from the cold-side of the strap.

2.4.2.1 Verification and Validation (V&V) of Results

This section will demonstrate the measures taken post-simulation to build confidence in the simulation results.

Due to time constraints, there was no opportunity to validate the design from a *performance* standpoint before the flight. Therefore, the design will be validated using the temperature data received post-flight; effectively making this mission a test flight for the thermal system.

However, the simulation results can still be verified. There are numerous ways to check the validity of simulation results within ANSYS. For this simulation, 3 checks were performed: convergence, thermal error, and mesh quality. All of these are, essentially, providing you with the same information (the accuracy of your results), but in different ways. The definition of these 3 checks are omitted here because they are already defined in Section 2.4.1 (V&V for the structural simulations). The only difference is that stress is the basis for the structural error and heat flow is the basis for the thermal error here.

The first check to perform is the convergence check. The check was performed for the full-assembly thermal simulation and the result is displayed in Figure 52 with the criterion curve in blue and the actual convergence curve in purple.

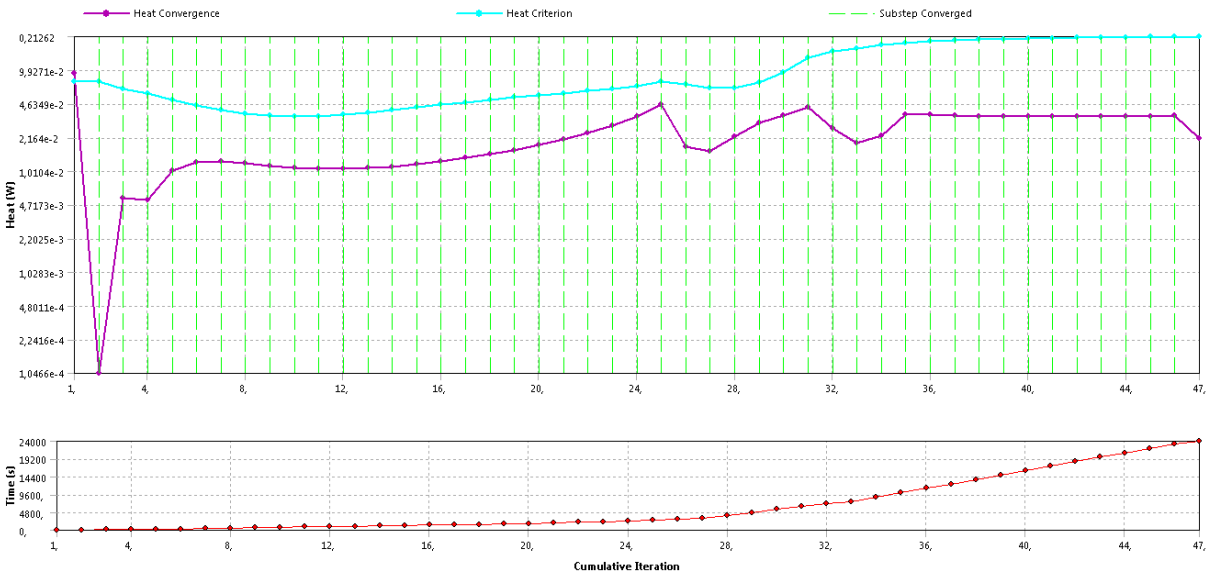

Figure 52: Heat convergence curve for the full-assembly thermal simulation

The convergence curve is below the validation criterion curve for almost the entire duration of the simulation, which is a good indication that the next checks should yield positive results as well.

The second check is the thermal error check. There were a few problem areas with the pre-flight simulation model, but the mesh was refined, and, throughout this simulation model, the maximum thermal error achieved was 0.092981 (9.2981%); this is in line with the results obtained from the convergence check and is an acceptable level of error.

Lastly is the mesh quality check using the aspect ratio and element quality metrics as indicators. Figures 53 and 54 demonstrate the distribution of the aspect ratios and element quality for the simulation model used.

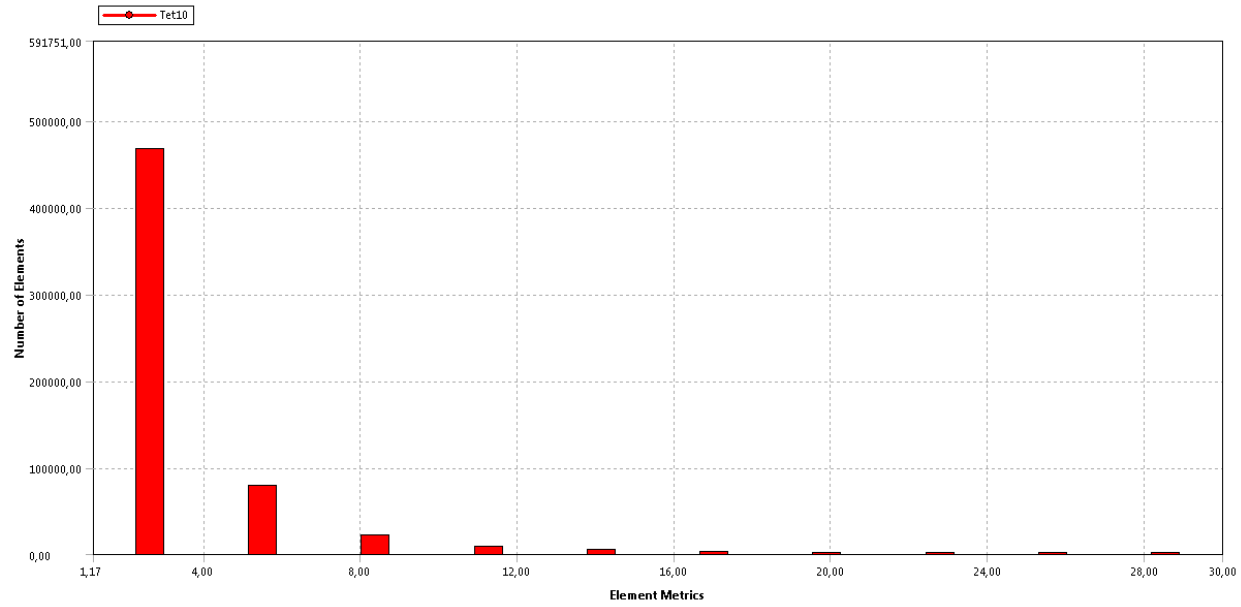

Figure 53: Distribution of aspect ratios for elements of the thermal simulation model

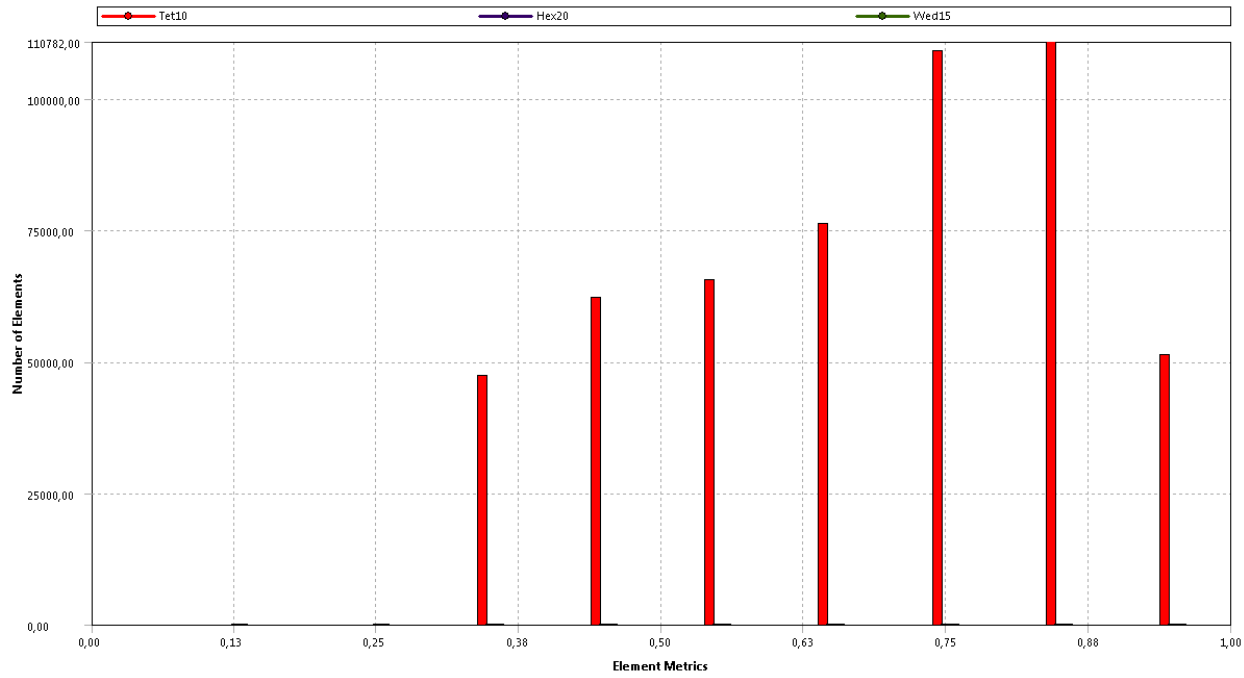

Figure 54: Distribution of element quality for elements of the thermal simulation model

It can be observed that the aspect ratio for >95% of the elements are in the range of 2 and 6, with the rest lying between 8 and 15. This indicates that the elements are less stretched out and providing good results since we desire aspect ratios below 10 and less than 10% above that value. To be safe, the elements that had

aspect ratio values above 10 were investigated and determined to be in non-critical areas, so they were left unrefined to save simulation time. It can also be observed that the element quality for all the elements are above 0.30. This is also indicative of good results since the minimum element quality desired is 0.30 for all elements, as discussed in Section 2.4.2.2.

It was decided, at this point, that there was enough confidence to move forward with the design and use it for the mission.

2.4.3 Mission Performance

This section will focus on the thermal system's performance during the flight. The first portion of the section (i.e. Section 3.4.3.1) will demonstrate how the simulation results compare to the flight data. The second portion of the section (i.e. Section 3.4.3.2) will demonstrate how the flight data was then used to show conformance to Requirements 1-3. To provide some context for the figures in Section 3.4.3.1, a view of the final assembly is provided in Figure 55 with each major component of the thermal system highlighted.

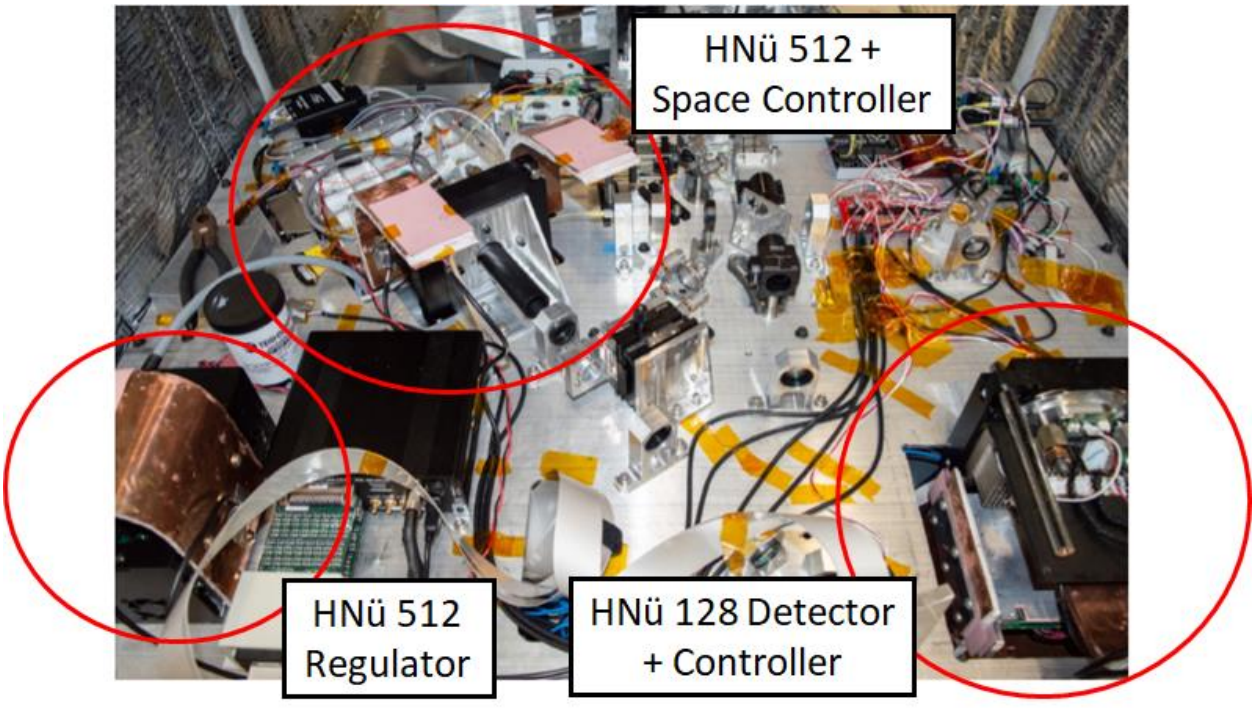

Figure 55: Final assembly of the thermal system integrated into the gondola (cover removed)

2.4.3.1 Component-Level Results

As mentioned, this section will be comparing the simulation results to the flight data. Each subsection will display the location of the thermocouple on the strap, the measured temperatures of the straps at strategic locations, and the results of the simulations performed (with the temperatures measured at the same location on the simulation model as the physical location of the thermocouple on the strap for the mission). The discussion of these results will be reserved to Section 3.4.3.2, instead of at the component-level, to avoid redundant explanations. Note that the results from two simulations are displayed: pre-flight and post-flight. These simulations are identical with the exception in the adjustment of two parameters for the simulation: the convection coefficient and ambient temperature curves. The motivation for the adjustment will be addressed in Section 3.4.3.2 in more detail.

Initially, it was planned to have thermocouples on both ends of all straps to measure their temperature difference, ΔT, throughout the flight. Having thermocouples directly on the surfaces defined in the requirements was impossible since these surfaces are directly interfaced and covered. Problems with the electrical system, however, caused the number of thermocouples allowed for the thermal system to be halved days before the launch. It was decided that the cold-side (heat sink-side) temperature would be measured. This decision was made because each component that generates heat (CCDs, controllers, regulator) already has temperature-measuring capabilities. By taking the cold-side temperature of the strap, we'd be able to observe the transfer of heat through the entire strap. The hot-side temperature would give us a better understanding of whether the surface temperatures remained below their maximums as defined in the requirements, but, as a trade-off, we lose a lot of information about the thermal system.

2.4.3.1.1 512 Detector

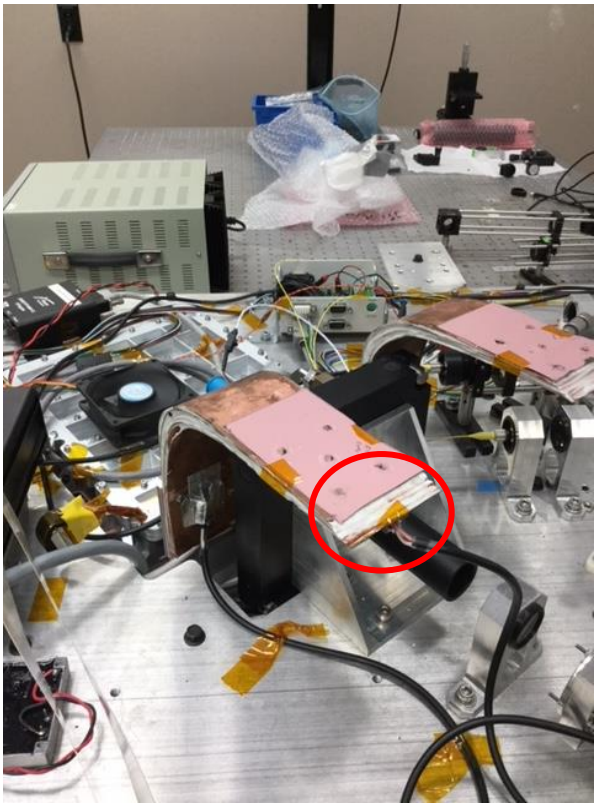

Figure 56: Thermocouple placement for the 512 Detector strap

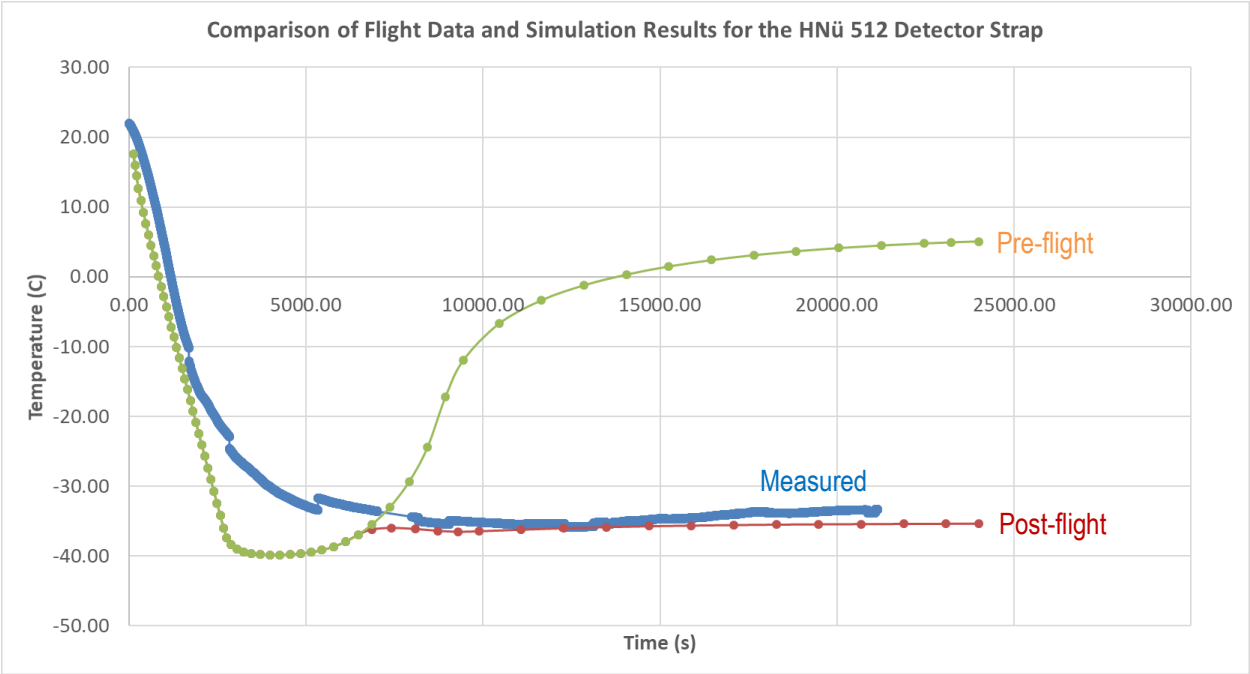

Figure 57: Simulation vs. mission comparison of 512 Detector strap's performance

2.4.3.1.2 128 Detector

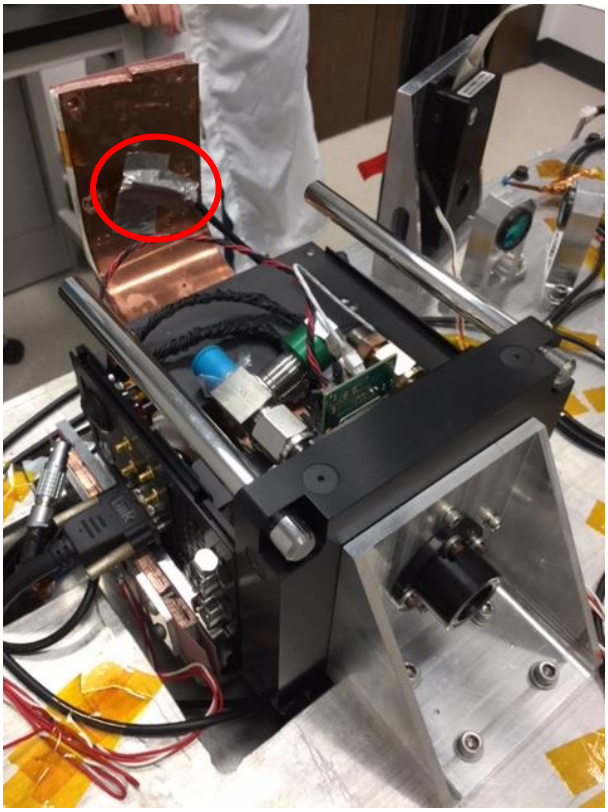

Figure 58: Thermocouple placement for the 128 Detector strap

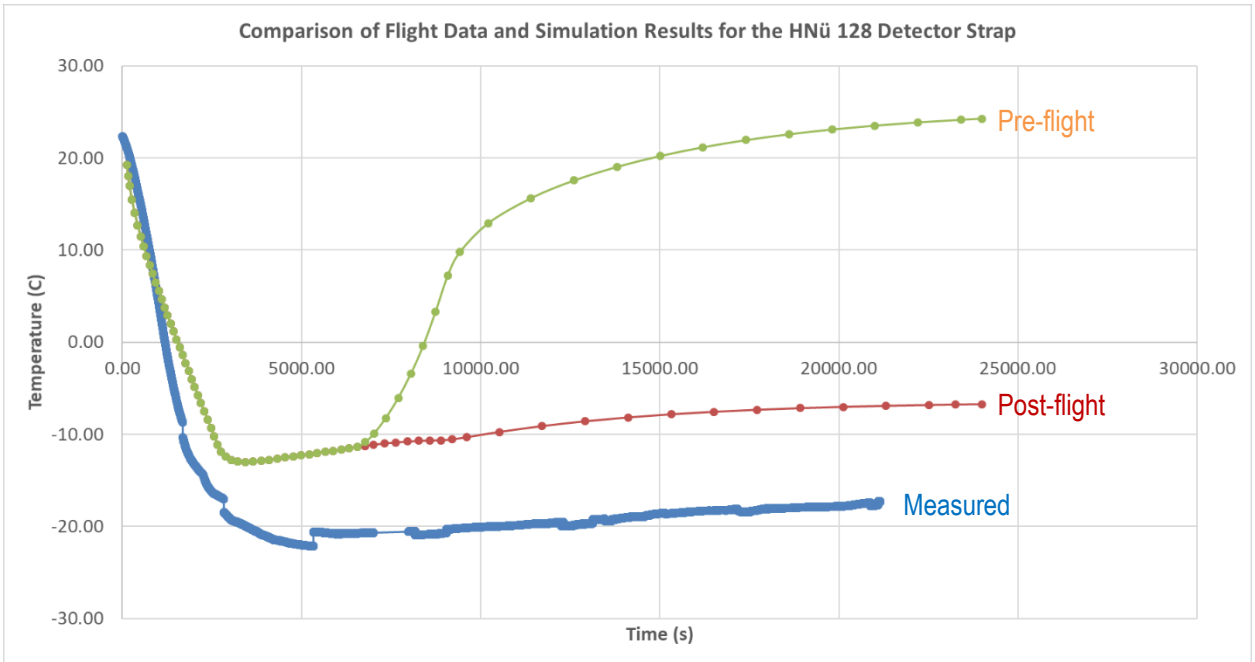

Figure 59: Simulation vs. mission comparison of 128 Detector strap's performance

2.4.3.1.3 128 Controller

Figure 60: Thermocouple placement for the 128 Controller strap

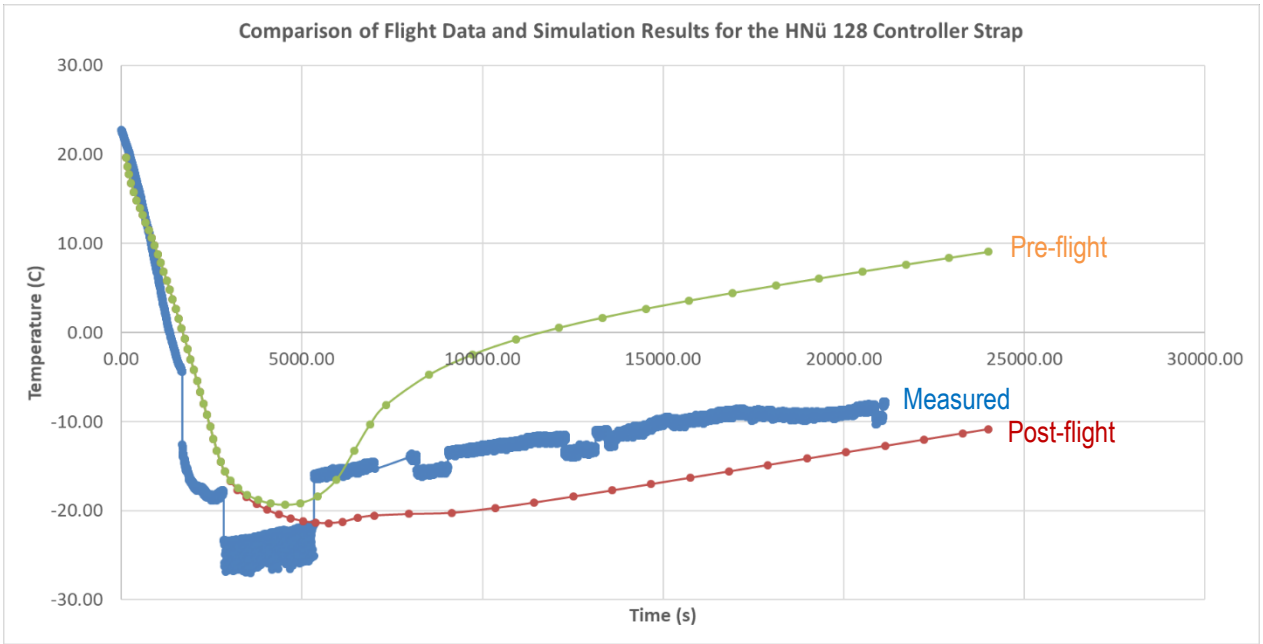

Figure 61: Simulation vs. mission comparison of 128 Controller strap's performance

2.4.3.1.4 512 Regulator

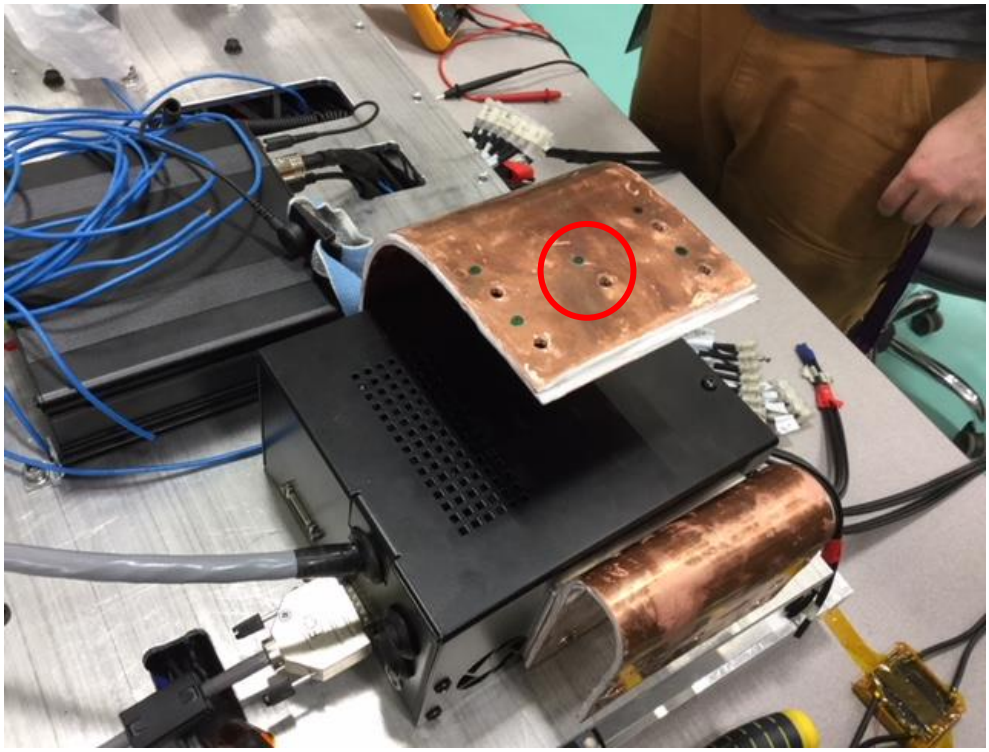

Figure 62: Thermocouple placement for the 512 Regulator strap

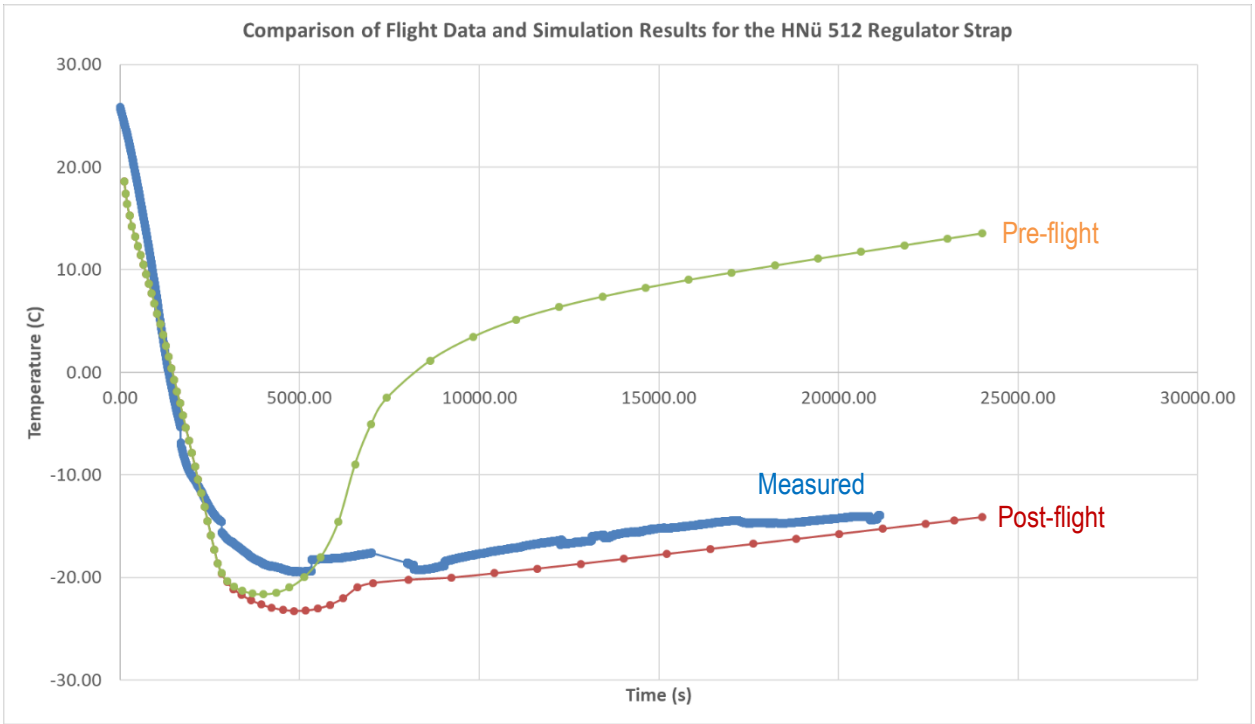

Figure 63: Simulation vs. mission comparison of 512 Regulator strap's performance

2.4.3.1.5 Space Controller

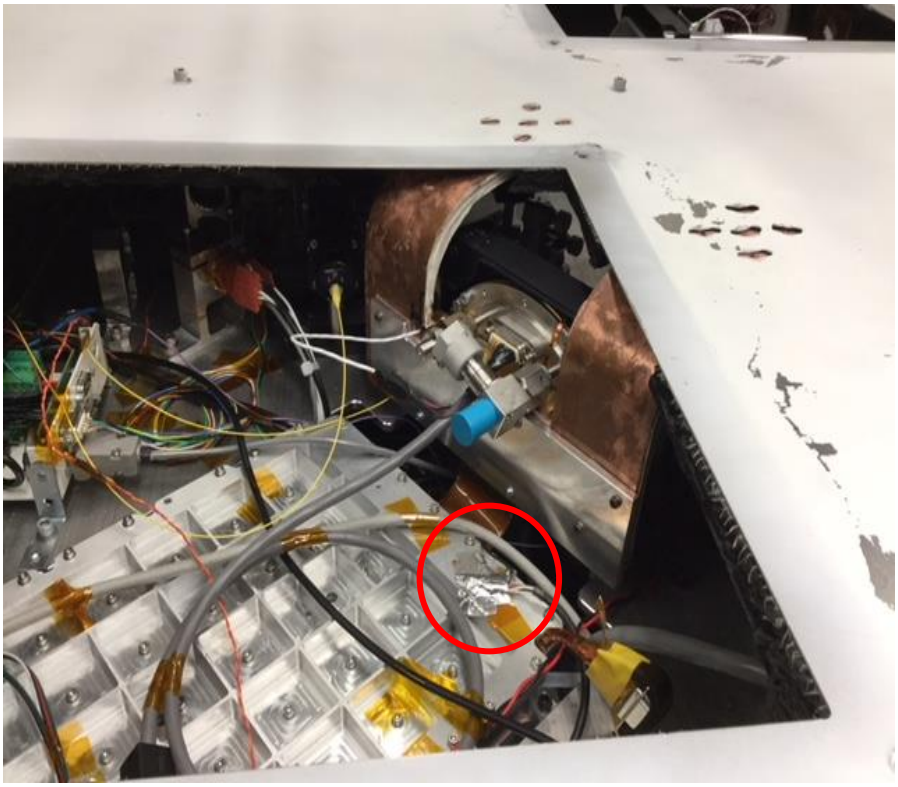

Figure 64: Thermocouple placement for the Space Controller strap

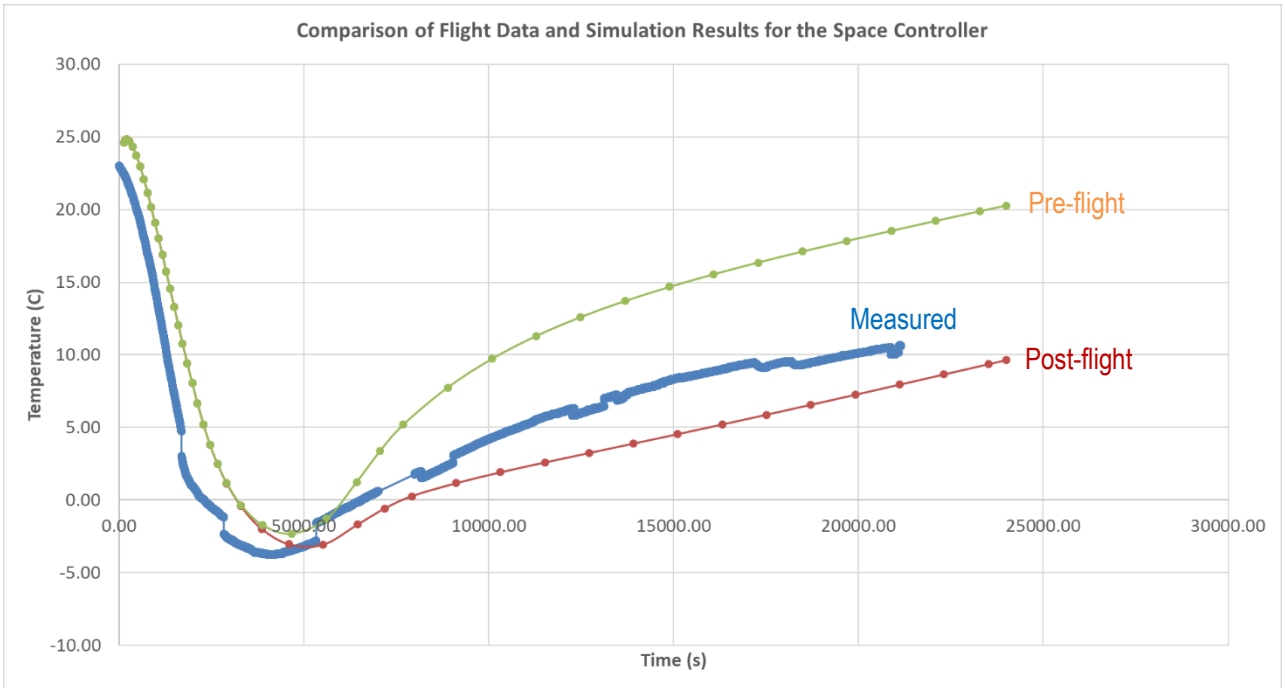

Figure 65: Simulation vs. mission comparison of Space Controller's performance

2.4.3.1.6 Bench

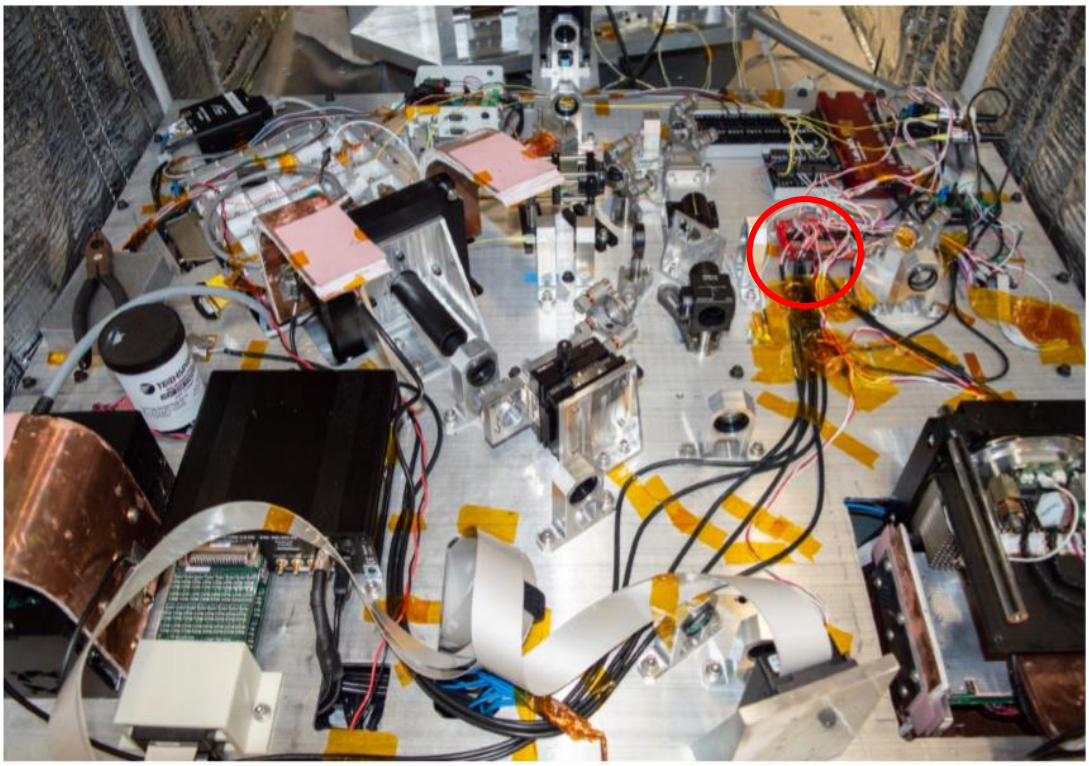

Figure 66: Thermocouple placement for the Bench

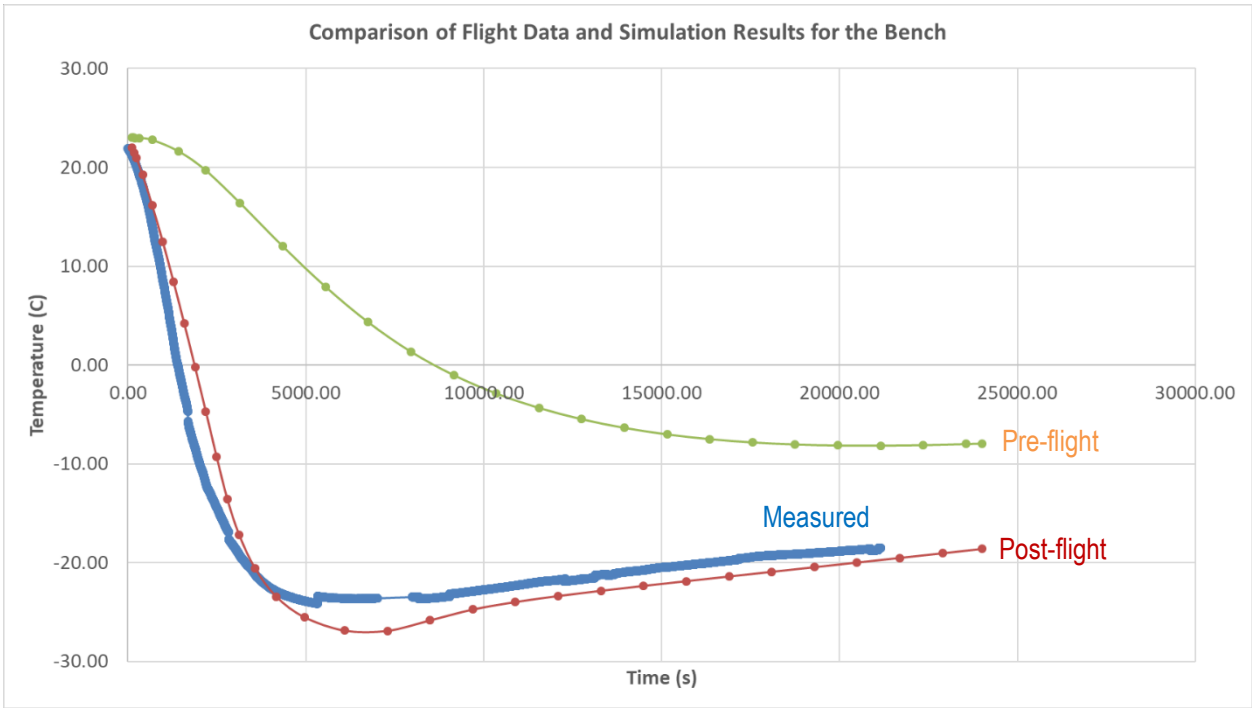

Figure 67: Simulation vs. mission comparison of Bench's performance

2.4.3.2 Component-Level Discussion of Results

2.4.3.2.1 Major discrepancy between Pre-flight Simulation and Measured Data

Before commenting on the curves, it's important to note that with the uncertainties in the flight parameters used for the simulations, as mentioned in Section 3.4.1, discussion of the parameters is necessary. Analyzing the thermocouple data after the mission, it was evident that there was a lot more convection and much lower temperatures than anticipated. This was concluded by the process of elimination. The only potential causes for this discrepancy are: inaccuracy of the simulation parameters or a behavioral difference between the simulation and physical model. The latter was proven to not be the case in Section 3.3.3.3 to a small degree in the testing of the straps and was proven again when the simulation parameters were analyzed.

If the simulation parameters were inaccurate, the problem must be an inaccuracy with one of the four parameters: heat input, radiation emissivity, convection coefficient, ambient temperature. The major problem is that none of these parameters can be verified or measured using hard data from the flight. However, we can speculate on which parameters were inaccurate for the flight through general discussion. The radiation emissivity is a parameter that was conservatively estimated at 0.90 and is a physical property not dependent on the operation of the payload or any system, so it likely does not contribute to the system being colder than expected since we have no reason for it not to behave as intended. This value also had a relatively small impact on the thermal design since convection was prevalent. The heat input can be confirmed to have been constant for almost the entire flight by looking at the voltage data of all the components. There were a few shorts that caused brief voltage drops, but, for more than 99% of the time, they were operational and generating heat as inputted for the simulations. However, the magnitude of the heat input could be inaccurate. For the simulations, 25 or 50 Watts per surface was used as a conservative estimate for the heat input, but these values could be as low as 15 or 35 Watts per surface, or lower, according to Nüvü Cameras. Therefore, the heat input could be a contributing factor.

However, the ambient temperature and the convection coefficient are two parameters that greatly effect the thermal dissipation characteristics of the system and are known to have been drastically different for the flight. The ambient temperature and convection coefficient were set based on the data presented in Section 3.4.1. However, as mentioned, this data could be highly unreliable due to the unpredictable nature of jet streams and day-to-day meteorology. It is possible, even with the low air density in the stratosphere, that the amount of air still present and the wind velocity allows for significant convection and, therefore, a convection coefficient much larger than used for the simulation. The CSA confirmed that the flight was much colder than expected, potentially having reached a temperature of -85°C for a brief period in the mid-level part of the stratosphere. With this knowledge, it is safe to assume that the ambient temperatures and convection coefficients were underestimated when performing the simulations. Convection coefficients are also dependent on geometry and direction of air flow, unlike the constant convection coefficient assumed for all surfaces of the simulation model. It's important to note, however, that this discrepancy would be a lot smaller in magnitude than was observed.

For these reasons, their values were slightly adjusted (and estimated) based on discussions with CSA employees and the same studies presented in Section 3.4.1; these values can be seen in Figures 68 and 69. The new parameters yielded the post-flight curves seen in Sections 3.4.3.1.1 to 3.4.3.1.6.

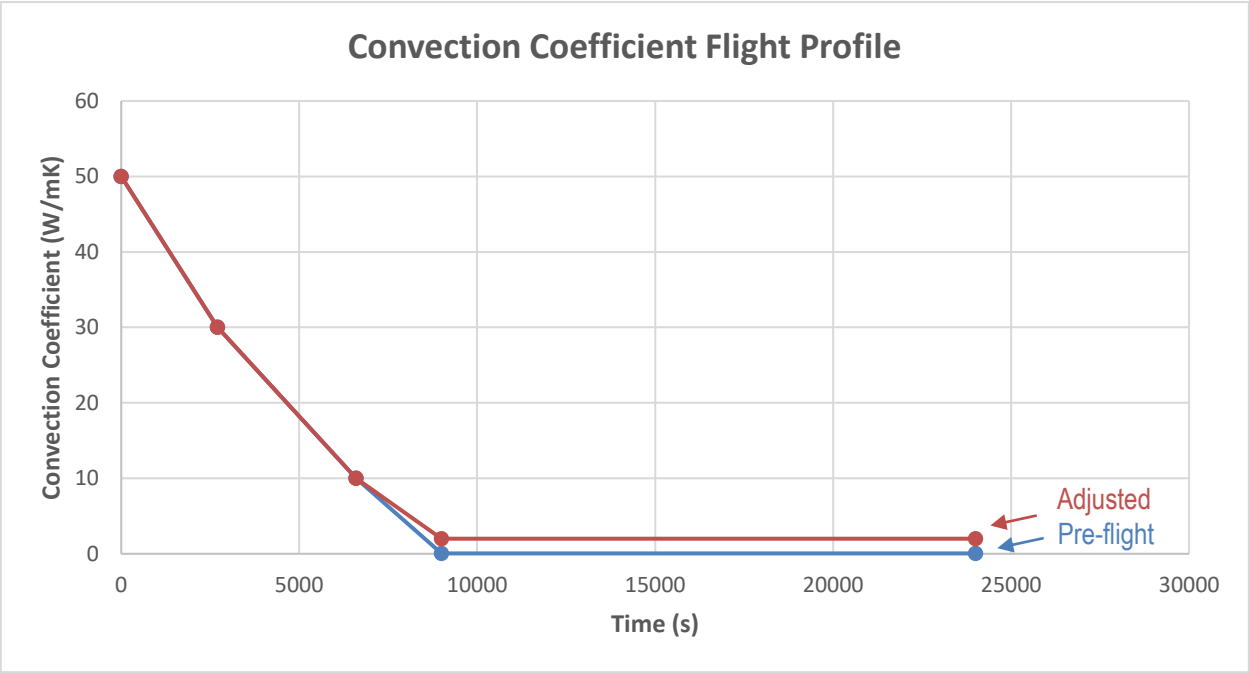

Figure 68: Adjusted convection coefficient curve for post-flight simulations

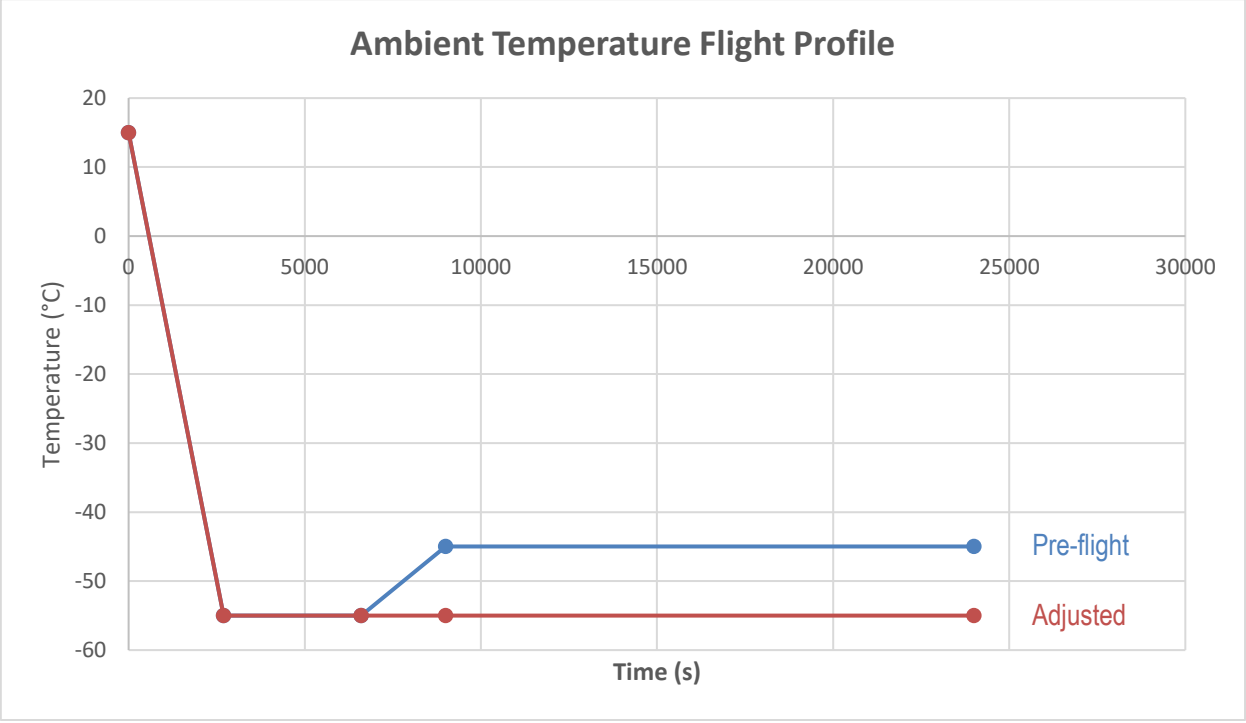

Figure 69: Adjusted ambient temperature curve for post-flight simulations

2.4.3.2.2 Comparison of the Adjusted Simulations and Measured Data

Before studying the curves more closely, some context is needed regarding the altitude profile and how it pertains to the trends in the curves. The graph in Figure 70 was generated using data supplied by CNES and displays the change in altitude of the payload over the entire duration of the mission. Although the altitude was not used directly as a simulation parameter, there is still crucial information that can be derived from it and it can also be compared to the pre-flight curve used for the simulations in case there are major differences.

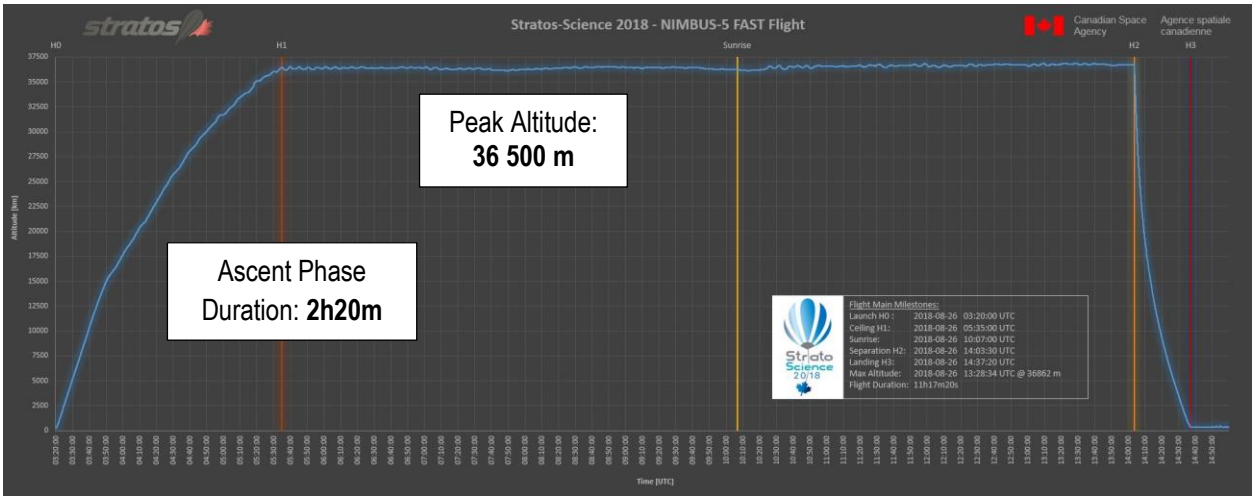

Figure 70: Approximate altitude profile of the flight for the entire duration of the mission

Luckily, the altitude profile is very similar to the curve used for the simulation and the discrepancy is negligible. However, Figure 70 is also relevant for the discussion of the results because it indicates at what point the flight is traversing the different parts of the atmosphere. From 0 to 2800 seconds, the balloon is in the troposphere, from ground-level to about 10 km altitude. From 2800 to 5500 seconds, the balloon is in the lower part of the stratosphere, from 10 km to 20 km altitude. Here, the ambient temperature and convection coefficient remain constant. From 5500 to 8000 seconds, the balloon is in the mid-level part of the stratosphere, from 20 km to 37 km altitude. And, finally, from 8000 to 24 500 seconds, the balloon is at its peak altitude, at about 37 km altitude.

Using this information, we can study the flight data and simulated temperature curve more effectively. For most of the curves in Section 3.4.3.1, the simulated and measured curves are very similar in the troposphere and peak altitude regions. The data used for the troposphere region was very reliable as this part of the atmosphere has been studied and characterized very well. At peak altitude, the data regarding temperature is relatively reliable, but the convection coefficient can be hard to pinpoint; this is due to the varying air properties and wind velocities in the stratosphere. Judging from the curves, the parameters used for those regions were relatively accurate. We can see that the simulated and measured curves have very similar trends for both regions in every curve, even if the curves are not at the same magnitude. In fact, the only curve that has a large difference in terms of magnitude is the curve for the 128 Detector (about 12°C difference). This was expected since the strap-detector interface was very difficult to accomplish, and even harder to model accurately for the simulation. Aside from that curve, every other curve has a temperature difference of less than 7°C, which is acceptable

considering the simplification of the simulation model and the many uncertainties surrounding the flight parameters.

Another region that is interesting to study is the lower and mid-level stratosphere regions (2800 to 8000 seconds). The simulated curves all tend to have a bit of a dip at these regions, they bottom out quickly and begin increasing towards the end of the latter region. The measured curves, however, simply begin to decline at a slower rate and begin to move towards a steady state. Regarding the simulated curve, this is likely due to the major uncertainties of the ambient temperature and convection coefficient at these regions. Another explanation is the simplification of the CAD model. Since most of the components in the assembly were removed (due to the lack of processing power), the system's *thermal inertia* was also impacted, the speed at which the system changes temperature to external factors. With a large assembly, there is more thermal mass and more thermal inertia and, therefore, the system will react slower; in other words, it would be more gradual. However, in a stripped-down version of the same assembly, there would be less thermal mass and less thermal inertia, causing the system to react much quicker; in other words, the change would be more observable. This is likely the cause of these dips in the simulation curves for the lower and mid-level stratosphere regions and why they aren't present in the measured temperature curves, the thermal inertia of the two models were very different. This doesn't affect the steady-state temperature that is attained later because thermal inertia only affects the speed at which the system reacts; eventually, a system with low thermal inertia will achieve the same steady-state temperature as a system with high thermal inertia, given that all the other conditions are the same.

Besides the 128 Detector curve that was discussed earlier, there are two curves that warrant a quick discussion as well. Firstly, you'll note that a supplementary temperature curve was added: the Bench's temperature. It was measured to characterize how it would react to the environment and the thermal system's management of the heat. By the end of the mission, the bench was at a temperature of about -20°C and it hadn't achieved a steady-state yet; the bench was quite isolated and probably required more time to stabilize. This information is particularly relevant for the optics system design. Secondly, the Space Controller curves also never stabilized. Since the platform was made of 6061-T6 aluminum, it most likely required a lot more time to achieve a steady-state since the material has a lower thermal conductivity and since the part itself was relatively large and had much more thermal inertia than the straps.

2.4.3.3 System-Level Results and Discussion

Section 3.4.3.1 and 3.4.3.2 focused primarily on comparing the measured results from the flight to the simulated results and seeing if the simulation was able to model the behavior of the system during flight. This section will focus more on comparing the measured results to the surface temperature limits defined in Requirements 1-3; in other words, this section will aim to analyze the results and determined if the requirements were satisfied.

As mentioned in Section 3.4.3, the thermocouples were placed on the cold-side of the thermal straps. In order to determine if Requirements 1-3 were satisfied, the temperatures of those surfaces need to be calculated. Knowing the actual temperature of the cold-side of the strap and using the ΔT values (i.e. between the cold-side and hot-side of the strap and, subsequently, between the hot-side of the strap and the critical surfaces) derived in Section 3.3.3.2, we can approximate value of the surface temperatures. These calculations were performed, and the results are shown in Table 13.

Table 14: Comparison of the temperatures measured for each surface and the limits

Strap Component	Max. Temp. of *Cold-Side* Measured (°C)	Max. Temp. of *Critical Surface* Derived (°C)	Max. Temp. of Critical Surface Allowed (°C)
HNü 512 Detector	-33.31	-18.65	30
Space Controller	-1.36	10.65	20
HNü 512 Regulator	-13.95	-2.36	40
HNü 128 Detector	-17.32	-5.98	30
HNü 128 Controller	-7.85	4.21	40

The temperature of the critical surfaces was maintained well below their limits. In fact, the least performant component was the Space Controller, which did not have a strap for heat dissipation; the explanation for this has already been discussed in Section 3.4.3.2.2.

2.5 Recommendations for Improvement

Although the thermal system performed well and met all the requirements, there's a few areas that can be improved. Specifically, the definition of the requirements and the overall design of the straps. Both will be discussed in the following subsections.

2.5.1 Definition of Requirements

As observed by the results in Section 3.4.3, the temperatures of the critical surfaces remained within their specified limits. However, in some instances, specifically for the HNü 512 detector strap, the temperatures were far below what was expected. Knowing that the ambient temperature can be a lot lower than expected and that convection is more prevalent than presumed, defining a lower limit is very necessary. Components overheat when the temperatures are too high, but they can also freeze or fail when temperatures are too low. The definition of these lower limits can be provided by Nüvü Cameras, as the higher limits were, but can also be determined by finding the highest lower limit of the electronic components (the bottleneck) for the controllers.

2.5.2 Overall Design of Thermal Straps

The thermal straps used for this project were made to mimic the shape of the commercial product that uses copper braids between two copper blocks. Although the design was successful in terms of performance, it can be improved to reduce weight, increase thermal conductivity, and increase flexibility in design. The proposed solution is rethinking the design to mimic the commercial strap solution even better.

First, design the copper blocks as needed to interface with the critical surfaces. Then, find copper braids (commercial electronic component) that are appropriately long and cut to size. Cold weld the copper braids to the copper blocks. Conductivity can be improved by heat treating the assembly, promoting recrystallization at the microstructure-level and enhancing its thermal properties. This solution mimics the commercial thermal straps very closely. The only differences will be that the processes and products used for the commercial straps will have been tailor-made for those products. Obviously, they may not perform as well as the commercial solution, but they will perform better than the copper shim solution used for this project because the thermal epoxy will be eliminated from the design. This increases the overall effective thermal conductivity of the part and, in turn, the amount of heat that can be transferred by the part (if the overall geometry and temperature gradient remain the same). This can be verified using the governing conduction equation that shows the proportionality of the heat flow rate to thermal conductivity, cross-sectional area, thickness, and the temperature gradient. Other major benefits of this design will be the reduction in weight and the flexibility of this design to interface in areas that are hard to route the strap towards. Thermal conductivity will also be improved because, if fabricated correctly, there will be less heat lost due to contact resistance and the thermal epoxy, which will be phased out of the design entirely.

Conclusion

From a top-level perspective, the mount structure and thermal systems proved to be well-designed because they fulfilled all the requirements defined for them. Both, though, have one or two major areas that need to be improved if they are to be reused for the next iterations of the HiCIBaS project.

For the telescope mount, there needs to be an overhaul of the design of top-portion of the structure. Specifically, reintroducing the counterweights and putting more emphasis on the vibrational analysis of the structure. Of course, this implies adding more requirements in order to include the aspect of vibrations and line-of-sight stability to the Scope of Work.

For the thermal system, major performance improvements can be made by overhauling the design completely using copper braids and blocks like the commercial product. This solution may prove to be difficult to develop a simulation model for because of the braids but can be approximated if the behavior of the model is tested. The thermal system can also benefit from the addition of more requirements, specifically to include the lower limits for the critical surfaces.

With the thought of using a 1-meter diameter telescope in the future in mind, it's also important to discuss the feasibility of both systems to be repurposed for such a mission. The telescope mount, of course, cannot be used for the 1-meter telescope. Its design was tailored to fit a commercial telescope and to accommodate the commercial motors. Since a 1-meter telescope will, likely, be custom-made, the design of the mount will depend heavily on it. With the commercial motors being changed as well (to suit the needs of the pointing system), the mount's design becomes obsolete. However, the redeeming qualities of the mount can be used for future designs, for instance: the bracketed design to maintain structural integrity while reducing weight and the interface plate configuration. The thermal system design, on the other hand, can be repurposed. If the changes discussed earlier are made, the thermal straps produced will be able to passively maintain the temperature of the critical surfaces under their limits. This will be very much dependent on the conditions of the flight, however, as experienced for this iteration of the project. For future missions, in order to obtain more accurate simulation results, the environmental data would be a huge priority. Without it, passive solutions are too risky. An active solution would do better because it has the capability of adjusting during the flight, cooling when the components are beginning to heat up and going into standby mode when components are cool enough.

For the purpose of this mission, though, both systems were successful at performing as expected. The telescope mount proved, in the lab, to provide the pointing system with a platform to track point sources. During the flight, the thermal system was able to maintain all the critical surfaces of the optics bench components below their maximum temperature limits.

References

Advanced Cooling Technologies. (2018). *Heat Pipe Loops*. Retrieved from Advanced Cooling Technologies: https://www.1-act.com/innovations/heat-pipes/heat-pipe-loops/

Bergman, T. L., Lavine, A. S., Incropera, F. P., & Dewitt, D. P. (2011). *Fundamentals of Heat and Mass Transfer, 7th ed.* John Wiley & Sons.

Borden, M. (2017). Thermal, Structural, and Optical Analysis of a Balloon-Based Imaging System. *Publications of the Astronomical Society of the Pacific*, 8.

Buscher, D. F. (2015). *Practical Optical Interferometry.* Cambridge: Cambridge University.

Centre National d'Études Spatiale. (2018). *Maximum Allowable Panel Insert Loads.*

Centre National d'Études Spatiale. (2018). *Shock Logger Flight Data.* Centre National d'Études Spatiale.

Federal Foam Technologies. (2007). *SONUS Foam.* Retrieved from Federal Foam Technologies: https://www.federalfoam.com/products/sonus-foam/

Henkel-Adhesives. (2015, January). *Sil-Pad 900S Technical Data Sheet.* Retrieved from Henkel-Adhesives: https://thermal.henkel-adhesives.com/files/downloads/datasheets/PDS-SP-900S-HENKEL-0615.pdf

Kaufman, M. (2017, January 24). *A Four Planet System in Orbit, Directly Imaged and Remarkable.* Retrieved December 23, 2018, from Many Worlds.

MacRobert, A. (2006, August 14). *How to Successfully Beat Atmospheric Seeing.* Retrieved December 23, 2018, from Sky & Telescope.

Mathieu, B. (2013). *Safety Engineer.* Canadian Space Agency.

McMaster-Carr. (2018). *Circuit Board Cooler.* Retrieved from McMaster-Carr: https://www.mcmaster.com/2195N9

McMaster-Carr. (2018). *Copper Shim Stock.* Retrieved from McMaster-Carr: https://www.mcmaster.com/9709k82

McMaster-Carr. (2018). *Moisture-Venting Polyurethane Foam Insulation.* Retrieved from McMaster-Carr: https://www.mcmaster.com/9385k73

Newmark Systems. (2018). *RM-3 Series Rotary Stage.* Retrieved from Newmark Systems: https://www.newmarksystems.com/datasheets/RM-3-Datasheet.pdf

Newmark Systems. (2018). *RM-5 Series Rotary Stage.* Retrieved from Newmark Systems: https://www.newmarksystems.com/datasheets/RM-5-Datasheet.pdf

Newmark Systems. (2018). *RM-8 Series Rotary Stage.* Retrieved from Newmark Systems: https://www.newmarksystems.com/datasheets/RM-8-Datasheet.pdf

Nüvü Cameras. (2018). *HNü EMCCD Camera*. Retrieved from Nüvü Cameras: http://www.nuvucameras.com/products/hnu-camera/

OMEGA. (2018). *OB-101 OMEGABOND Epoxy Adhesive.* Retrieved from OMEGA: https://www.omega.com/Manuals/manualpdf/M0064.pdf

Technology Applications, Inc. (2018). *Thermal Straps - Copper Thermal Straps (CuTS)*. Retrieved from Technology Applications, Inc.: https://www.techapps.com/copper-thermal-strap-assemblies

Thermal Space. (2016). *Cold-Plate Design, Fabrication, and Testing*. Retrieved from Thermal Space: https://thermal-space.com/cold-plate-design-and-fabrication/

Université Laval. (2016). *HiCIBaS - High-Contrast Imaging Balloon System Proposal.* Université Laval.

Appendices

Appendix 1: Rotary Motor Datasheets

Excerpt from RM-3 Motor datasheet

Specifications	
Resolution	Stepper Motor: 0.36 arc-sec (72:1 gear ratio), 0.72 arc-sec (36:1 gear ratio) Servo Motor: 4.5 arc-sec (72:1 gear ratio), 9 arc-sec (36:1 gear ratio)
Accuracy	70 arc-sec
Max. Speed	Stepper Motor: 25°/sec (72:1 gear ratio), 100°/sec (36:1 gear ratio) Servo Motor: 180°/sec (72:1 gear ratio), 360°/sec (36:1 gear ratio)
Unidirectional Repeatability	5 arc-sec
Max Payload Weight	90.7kg (200lbs)
Travel Range	360° Continous
Encoder	Optical rotary encoder mounted to rear of motor, 1000 lines (4000 CPR) with Index (Optional)
Origin	Optical Home Switch (optional) Optical index mark on encoder (with encoder option)
Gear Ratio	72:1 or 36:1
Stage Weight	3.6 kg (8 lbs)
Material	Aluminum Alloy Construction
Finish	Black Anodize

Load Characteristics

Normal Load (Fz)	90.7 kg (200 lbs)
Moment Load (Ma)	54.2 Nm (40 lb-ft)
Max. Torque (Tz)	12.5 Nm (9.2 lb-ft)

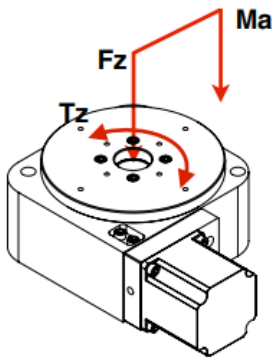

Figure A1: Manufacturer's datasheet for the RM-3 motor (Newmark Systems, 2018)

Excerpt from RM-5 Motor datasheet

Specifications	
Resolution	Stepper Motor: 0.29 arc-sec (90:1 gear ratio), 0.57 arc-sec (45:1 gear ratio) Servo Motor: 3.6 arc-sec (90:1 gear ratio), 7.2 arc-sec (45:1 gear ratio)
Accuracy	70 arc-sec
Max Speed	Stepper Motor: 30°/sec (90:1 gear ratio), 50°/sec (45:1 gear ratio) Servo Motor: 180°/sec (90:1 gear ratio), 360°/sec (45:1 gear ratio)
Unidirectional Repeatability	5 arc-sec
Max Payload Weight	20.4 kg (45 lbs)
Travel Range	360° Continous
Encoder	Optical rotary encoder mounted to rear of motor, 1000 lines (4000 CPR) with Index (Optional, Standard with servo motor)
Limit Switches	None
Origin	Optical Home Switch (optional) Optical index mark on encoder (with encoder option)
Gear Ratio	90:1 or 45:1
Stage Weight	1.4 kg (3 lbs)
Material	Aluminum Alloy Construction
Finish	Black Anodize

Load Characteristics

Normal Load (Fz)	20.4 kg (45 lbs)
Moment Load (Ma)	13.5 Nm (10 lb-ft)
Max. Torque (Tz)	4.5 Nm (3.3 lb-ft)

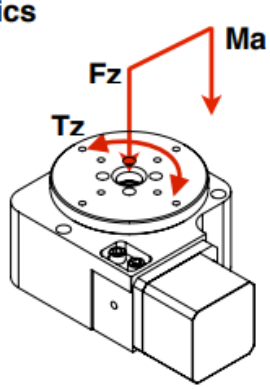

Figure A2: Manufacturer's datasheet for the RM-5 motor (Newmark Systems, 2018)

Excerpt from RM-8 Motor datasheet

Specifications	
Resolution	Stepper Motor: 0.32 arc-sec Servo Motor: 4.1 arc-sec
Accuracy	70 arc-sec
Max. Speed	Stepper Motor: 20°/sec Servo Motor: 100°/sec
Repeatability (uni-directional)	5 arc-sec
Max Load Capacity	317 kg (700 lbs)
Travel Range	360° Continous
Encoder	Optical rotary encoder mounted to rear of motor, 4000 CPR with Index (Optional)
Origin	Inductive home switch (Optional) Optical index mark on encoder (with encoder option)
Gear Ratio	80:1
Stage Weight	13.6 kg (30 lbs)
Material	Aluminum Alloy Construction
Finish	Black Anodize

Load Characteristics

Normal Load (Fz)	317 kg (700 lbs)
Moment Load (Ma)	135.5 Nm (100 lb-ft)
Max. Torque (Tz)	23 Nm (17 lb-ft)

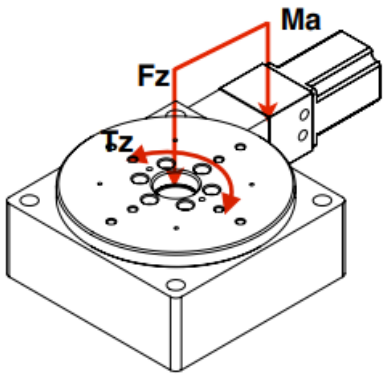

Figure A3: Manufacturer's datasheet for the RM-8 motor (Newmark Systems, 2018)

Appendix 2: Load Specification for Gondola's Inserts

Maximum Allowable Panel Insert Loads

Each panel is fixed using 12x M8 Hex Socket Cap Screws and provide 110 x M6 inserts.
There are two maximum allowable loads depending if attached nearby the structural inserts or not.
Structural inserts are shown with orange dot below. Loads are show in table below.
The assembly must pass the criterion (≤1) show below the table.

La reprise des équipements sur les panneaux est assurée par les inserts équipements. Les inserts permettent soit le bridage direct des équipements sur le plateau soit le montage de sangles au moyen d'équerres vissées sur ces inserts.
Dans tous les cas, le calcul du nombre d'inserts nécessaires à la reprise des équipements sur les plateaux est à la charge de l'architecte mécanique de la nacelle.

Pour cela, les informations suivantes devront être fournies par l'équipementier : masse de l'équipement, son volume et la position sur les 3 axes du CDG par rapport au volume.

Pour mémoire, on rappelle les résultats suivants issus des dossiers de justification mécanique de la nacelle (voir DR1) :

		Vertical	Lateral
	Inserts M6	**Effort normal maximal P_{crit} (N)**	**Effort transverse maximal Q_{crit} (N)**
All inserts except inserts nearby structural inserts	**Tous les inserts à l'exclusion des inserts situés à proximité des inserts structuraux**	1960	4080
Inserts nearby structural inserts (orange)	**Tous les inserts à proximité des inserts structuraux**	1105	4080

L'assemblage doit répondre aux exigences suivantes :

$$\left(\frac{P}{P_{crit}}\right)^2 + \left(\frac{Q}{Q_{crit}}\right)^2 \leq 1$$ Critère pour les inserts

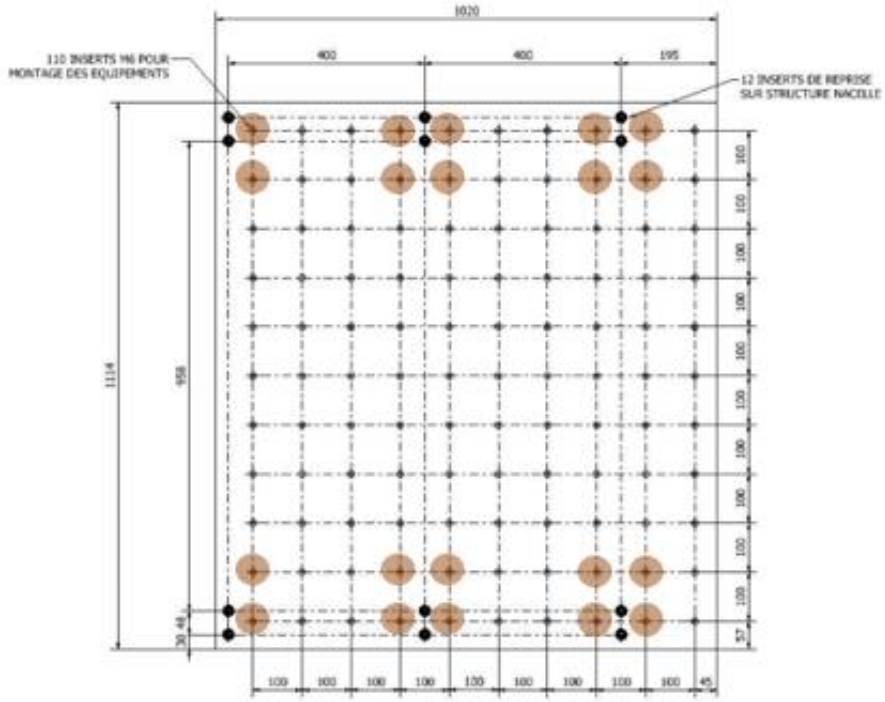

Figure A4: Insert load specifications (Centre National d'Études Spatiale, 2018)

Appendix 3: Excerpt from CSA Safety Regulations Document

5.4.2 Mechanical design dimensioning principle

5.4.2.1 Rule 4.2: Mechanical design dimensioning principle

Mechanical design dimensioning is based on the following principle:

- the limit load LL multiplied by the various safety factors measured during the dimensioning process must remain below the material yield load YL and,
- the limit load LL multiplied by the various safety factors measured during the dimensioning process must remain below the material ultimate load UL.

The limit load is determined either by the maximum observed load (in 99% of cases with a 90% confidence), or by calculation.

Safety factors usually include:

- model factor (KM),
- project factor (KP),
- design factor (FOSD: Factor Of Safety – Design),
- yield factor (FOSY: Factor Of Safety – Yield),
- ultimate factor (FOSU: Factor Of Safety – Ultimate),

By definition:

- DLL (design limit load) = LL*KM*KP*FOSD,
- DYL (design yield load) = DLL*FOSY,
- DUL (design ultimate load) = DLL*FOSU.

Design dimensioning must verify that DYL <= YL and DUL <=UL.

Rule	*Criterion*	*Means of compliance*	*Applicable during phase*	*Applicable to project*
D4.2	*The mechanical dimensioning*	*Description and*	*1*	*PL, PLG, AE*

5.4.2.2 Rule 4.3: Minimum safety factor

A minimum safety factor of 1.5 must be applied to the yield limit:

LL*1.5 <= YL.

Rule	*Criterion*	*Means of compliance*	*Applicable during phase*	*Applicable to project*
D4.3	*The mechanical design dimensioning principle must show compliance with the minimum safety factor.*	*Description and justification*	*1*	*PL, PLG, AE*

Figure A5: Design criteria defined in CSA Safety Regulations Document (Mathieu, 2013)

Appendix 4: Impact Loads Measured During Mission

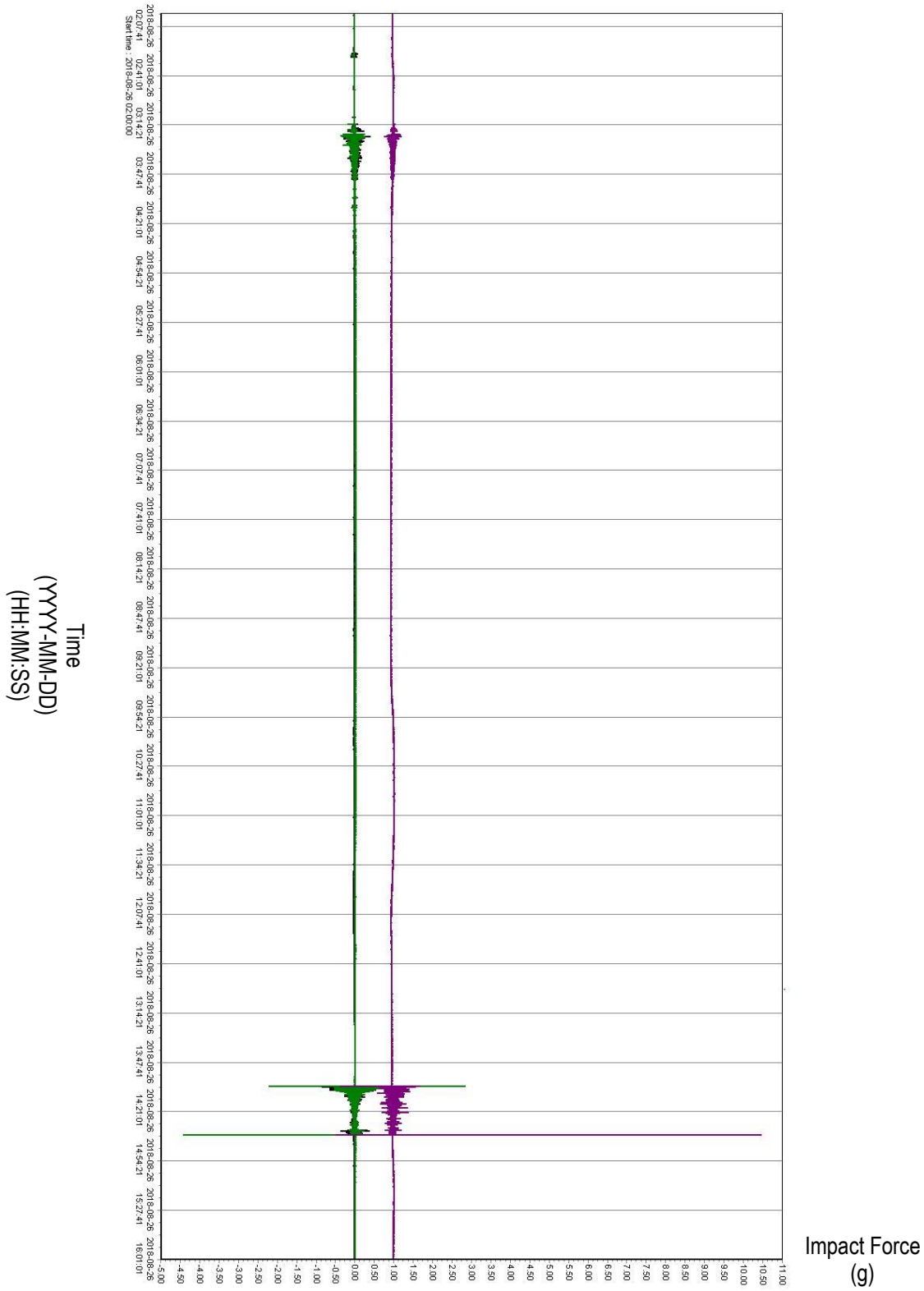

Figure A6: Impact loads measured during mission (Centre National d'Études Spatiale, 2018)

Appendix 5: Thermal System Material Datasheets

Copper Shim Stock

Copper Shim Stock

6" x 100" Roll, 0.032" Thick

Each

ADD TO ORDER

Ships in 2-5 weeks
$120.07 Each
9709K82

Shape	Rectangular
System of Measurement	Inch
Thickness	0.032"
Thickness Tolerance	-0.0015" to 0.0015"
Length	100"
Length Tolerance	-0.25" to 0.5"
Width	6"
Width Tolerance	-0.01" to 0.01"
Shim Stock Form	Roll
Material	110 Copper
Hardness	
Min.	Rockwell 15T47
Maximum	Rockwell 15T57
Temper Rating	Softened
Fabrication	Cold Worked
Magnetic Properties	Nonmagnetic
Certification	Material Certificate with Traceable Lot Number and Test Report
Specifications Met	ASTM B152
RoHS	Compliant

The most electrically conductive stock we offer. It is also corrosion resistant. Use it to create custom shims to fit for your applications.

Figure A7: Supplier's datasheet for the copper shim stock (McMaster-Carr, 2018)

Thermal Epoxy (Excerpt)

General Description

OMEGA's OB-101 Epoxy Cement is a versatile, room temperature cure, two-part epoxy cement. It is designed to permanently bond OMEGA's CO series, cement-on and beaded wire thermocouples, and other sensors to a wide variety of materials. OB-101 has many exceptional characteristics including:

- Resists temperatures to 221°F (105°C)
- Resists oil, solvents and most acids
- Heat conductive and tensile shear resistant
- Excellent electrical insulator
- Excellent mechanical bonding characteristics
- Adheres to most surfaces

Curing

Allow about four hours for initial set at room temperature (75°F, 24°C). Full cure will develop during the following 24 hours. Cure may be accelerated by moderate heat.

Physical Properties*

Service Temperature	-67°F to 221°F (-55°C to 105°C)
Thermal Conductivity (BTU) (in/hr) (ft^2) (°F):	7.2
Thermal Conductivity) (cal) (cm/sec) (cm^2) (°C):	0.0025
Volume Resistivity, ohm-cm:	10^{15}
Tensile Shear, ½" (1.27cm) overlap, psi:	2,200, min. (154 kg/sq. cm)
Flexural Strength, psi:	12,000, min. (840 kg/sq. cm)
Coefficient of Thermal Expansion:	20×10^{-6} in/in/°F (36×10^{-6} in/in/1°C)
Chemical and Solvent Resistance:	Excellent
Color:	White

*Determined under laboratory conditions using applicable ASTM procedures. Actual field data may vary. Do not use Physical Properties for warranty specifications.

Figure A8: Manufacturer's datasheet for the thermal epoxy (OMEGA, 2018)

Polyurethane Foam

Moisture-Venting Polyurethane Foam Insulation

Sheeting with Adhesive Backing, 54" Wide x 1" Thick, 4' Long

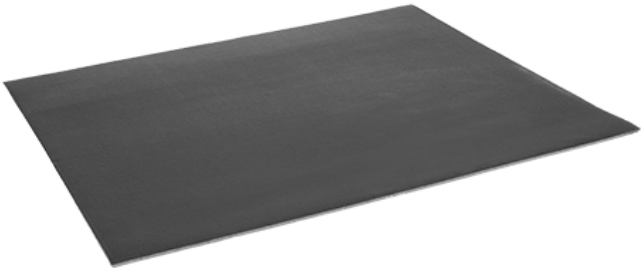

Each

In stock
$81.45 Each
9385K73

ADD TO ORDER

Insulation Type	Sheet/Strip
Thickness	1"
Width	54"
Length	48"
Temperature Range	-20° to 200° F
R Value	3.3
Heat Flow Rate	0.3 @ 75° F
Density	2 lbs./cu. ft.
Material	Polyurethane Foam
Facing Material	Vinyl
Flexibility	Flexible
Cell Type	Open
Backing Type	Adhesive
Color	Black
Facing Color	Black
For Use Outdoors	No
Specifications Met	FMVSS-302
Additional Specifications	SDS

Open-cell construction allows moisture to evaporate from this foam insulation. It also resists cracking and fading. These sheets have an easy-to-clean vinyl facing for added strength and abrasion resistance.

Figure A9: Supplier's datasheet for polyurethane foam (McMaster-Carr, 2018)

FEDERAL FOAM TECHNOLOGIES INC.
MATERIAL SPECIFICATION SHEET

MATERIAL NUMBER: 31200
DESCRIPTION: MILITARY SPECIFICATION VINYL/FOAM COMPOSITE

APPLICATIONS:

31200 is a flame laminated composite consisting of polyester urethane foam and perforated vinyl. Its primary use is in military vehicle interiors.

PRODUCT CONSTRUCTION:

Facing: Perforated Vinyl
Foam: Open Cell Polyester Urethane

CERTIFIED PHYSICAL PROPERTIES:

Foam:

Property	Test Method	Value
Density	ASTM D 3574, Test A	2.0 ± 0.2 pcf
Tensile Strength	ASTM D 3574, Test E	15 psi minimum (die A of ASTM D 412)
Change in Tensile Strength	ASTM D 3574, Test K	25% maximum
Tear Strength	ASTM D 3574, Test F	1.8 pli minimum
Low Temperature Flexibilty	N/A	No cracking when bent around a one inch mandrel after 4 hour cold soak @ -50°F
Flammabiltiy	UL 94	HF-1, Certified
Color	N/A	Charcoal Gray or Black

Vinyl:

Property	Test Method	Value
Weight	N/A	19 oz/ly minimum @ 54" width
Thickness (Vinyl plus back)	N/A	0.021" minimum
Backing Weight	N/A	2.0 oz/yd² minimum
Backing material	N/A	Polyester or Polyester/Cotton Blend
Perforation- Hole Diameter	N/A	0.078" nominal
Perforation- Hole Pattern	N/A	24 holes/in² staggered (or equivalent)
Flammabiltiy	FMVSS302	Certified
Color	N/A	Black

Composite:

Property	Test Method	Value
Bond Type	N/A	Flame Laminated- Vinyl to Foam
Temperature Resistance	N/A	-50°F to 250°F (no unforced delamination)
Bond Adhesion	ASTM D 903	1.0 pli minimum

6/14/07

Figure A10: Supplier datasheet for polyurethane foam (Federal Foam Technologies, 2007)

Thermal Interface Material

Circuit Board Cooler

12" Long x 12" Wide x 0.009" Thick

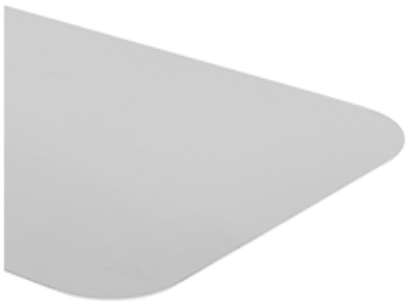

Each

In stock
$57.16 Each
2195N9

ADD TO ORDER

Shape	Square
Length	12"
Width	12"
Thickness	0.009"
Material	Fiberglass-Reinforced Silicone Rubber
Color	Pink
Temperature Range	-75° to 355° F
Tensile Strength	1,300 psi
Dielectric Strength	5,500V AC
Hardness	Durometer 92A
Specifications Met	UL 94V0

Also known as thermal pads and thermal interface pads, these heat-dissipating pads pull heat away from electronic components. They're often used to fill gaps between two surfaces that require thermal contact. All meet UL 94V0 for flame retardance.

Figure A11: Supplier's datasheet for thermal interface material (McMaster-Carr, 2018)

McMaster-Carr Part Number 2195N9 = Sil-Pad 900S

Sil-Pad® 900S

High Performance Insulator for Low-Pressure Applications

Features and Benefits

- Thermal impedance: 0.61°C-in²/W (@50 psi)
- Electrically isolating
- Low mounting pressures
- Smooth and highly compliant surface
- General-purpose thermal interface material solution

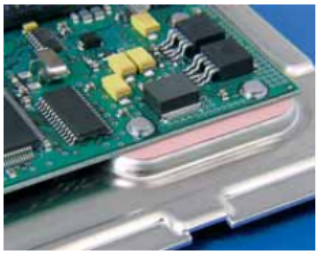

The true workhorse of the Sil-Pad product family, Sil-Pad 900S thermally conductive insulation material, is designed for a wide variety of applications requiring high thermal performance and electrical isolation. These applications also typically have low mounting pressures for component clamping.

Sil-Pad 900S material combines a smooth and highly compliant surface characteristic with high thermal conductivity. These features optimize the thermal resistance properties at low pressures.

Applications requiring low component clamping forces include discrete semiconductors (TO-220, TO-247 and TO-218) mounted with spring clips. Spring clips assist with quick assembly and apply a limited amount of force to the semiconductor. The smooth surface texture of Sil-Pad 900S minimizes interfacial thermal resistance and maximizes thermal performance.

TYPICAL PROPERTIES OF SIL-PAD 900S

PROPERTY	IMPERIAL VALUE	METRIC VALUE	TEST METHOD
Color	Pink	Pink	Visual
Reinforcement Carrier	Fiberglass	Fiberglass	—
Thickness (inch) / (mm)	0.009	0.229	ASTM D374
Hardness (Shore A)	92	92	ASTM D2240
Elongation (%45° to Warp and Fill)	20	20	ASTM D412
Tensile Strength (psi) / (MPa)	1300	9	ASTM D412
Continuous Use Temp (°F) / (°C)	-76 to 356	-60 to 180	—
ELECTRICAL			
Dielectric Breakdown Voltage (Vac)	5500	5500	ASTM D149
Type 3 Electrodes	8300	8300	ASTM D149
Dielectric Constant (1000 Hz)	6.0	6.0	ASTM D150
Volume Resistivity (Ohm-meter)	10^{10}	10^{10}	ASTM D257
Flame Rating	V-O	V-O	U.L. 94
THERMAL			
Thermal Conductivity (W/m-K)	1.6	1.6	ASTM D5470

THERMAL PERFORMANCE vs PRESSURE					
Pressure (psi)	10	25	50	100	200
TO-220 Thermal Performance (°C/W)	3.96	3.41	2.90	2.53	2.32
Thermal Impedance (°C-in²/W) (1)	0.95	0.75	0.61	0.47	0.41

1) The ASTM D5470 test fixture was used. The recorded value includes interfacial thermal resistance. These values are provided for reference only. Actual application performance is directly related to the surface roughness, flatness and pressure applied.

Typical Applications Include:

- Power supplies
- Automotive electronics
- Motor controls
- Power semiconductors

Configurations Available:

- Sheet form, die-cut parts and roll form
- With or without pressure sensitive adhesive

Building a Part Number

SP900S – 0.009 – AC – 00 – ACME 951753 Rev B

- Section A: SP900S = Sil-Pad 900S Material
- Section B: 0.009 = Standard thicknesses available: 0.009"
- Section C: AC = Adhesive, one side; 00 = No adhesive
- Section D: ___ = Standard configuration dash number, 1212 = 12" x 12" sheets, 12/250 = 12" x 250' rolls, or 00 = custom configuration
- Section E: NA = Selected standard option. If not selecting a standard option, insert company name, drawing number, and revision level.

example

Note: To build a part number, visit our website at www.bergquistcompany.com.

Standard Options

Sil-Pad®: U.S. Patents 4,574,879; 4,602,125; 4,602,678; 4,685,987; 4,842,911 and others

Figure A12: Manufacturer's datasheet for thermal interface material (Henkel-Adhesives, 2015)

Appendix 6: System of Equations derived from Thermal Resistance Network

$$T_{crit} \times \left(\frac{1}{\frac{R_{mount}}{2}} \right) = T_1 \times \left(\frac{1}{\frac{R_{mount}}{2}} \right) + q_{input}$$

$$T_1 \times \left(\frac{-1}{\frac{R_{mount}}{2}} + \frac{1}{\frac{R_{mount}}{2} + R_{strap}} - \frac{C_{mount}}{\Delta t} \right) - T_2 \times \left(\frac{1}{\frac{R_{mount}}{2} + R_{strap}} \right) = -T_{int} \times \left(\frac{1}{\frac{R_{mount}}{2}} \right) - \frac{C_{mount} T_1^{OLD}}{\Delta t}$$

$$T_2 \times \left(\frac{1}{\frac{R_{mount}}{2} + R_{strap}} + \frac{1}{\frac{R_{strap}}{2} + R_{floor}} - \frac{C_{strap}}{\Delta t} \right) - T_3 \times \left(\frac{1}{\frac{R_{strap}}{2} + R_{floor}} \right) = -T_1 \times \left(\frac{1}{\frac{R_{mount}}{2} + R_{strap}} \right) - \frac{C_{strap} T_2^{OLD}}{\Delta t}$$

$$T_3 \times \left(\frac{1}{\frac{R_{strap}}{2} + R_{floor}} + \frac{1}{R_{floor} + \frac{R_{conv} R_{rad}}{R_{conv} + R_{rad}}} - \frac{C_{floor}}{\Delta t} \right) - T_{amb} \times \left(\frac{1}{R_{floor} + \frac{R_{conv} R_{rad}}{R_{conv} + R_{rad}}} \right) = -T_2 \times \left(\frac{1}{\frac{R_{strap}}{2} + R_{floor}} \right) - \frac{C_{floor} T_3^{OLD}}{\Delta t}$$

Figure A13: Example of one system of equations derived from thermal resistance network